Dynamic Shearing Resistance of an Energetic Material Simulant: Sucrose

Pinkesh Malhotra[(a)], Tong Jiao, David L. Henann, Rodney J. Clifton, Pradeep R. Guduru

School of Engineering, Brown University, 182 Hope Street, Providence, RI 02912, USA
[(a)]Email address: pinkesh_malhotra@alumni.brown.edu

Abstract: Sucrose is a commonly used energetic material simulant for β-HMX. However, its behavior under extreme loading conditions remains poorly understood. Pressure-Shear Plate Impact (PSPI) experiments have been conducted to provide an experimental foundation for developing a suitable constitutive model for sucrose. Experiments have been performed at two different nominal normal stress values, 3 and 9.5 GPa, with nominal shear strain-rates of the order of $10^6\ s^{-1}$. Sucrose exhibits a shear strength of ~400-500 MPa in this pressure range, with a relatively small pressure sensitivity. However, pronounced strain softening is observed in sucrose at sufficiently large shear strains - even a dramatic drop in shearing resistance in some cases. A thermodynamically-consistent constitutive theory is presented to model the thermoelastic, thermo-viscoplastic response of sucrose. The use of the logarithmic strain and an appropriate set of invariants allows for separation of the Cauchy stress into pressure and deviatoric terms. A complete Mie-Gruneisen equation of state is presented to model the volumetric behavior while the deviatoric response is captured through the Johnson-Cook Model. The material model is able to capture experimental observations and predicts localization in the form of adiabatic shear bands, which explains the catastrophic drop in shearing resistance of sucrose observed in the experiments. Such localization events carry important implications for energetic materials in the context of hot-spot formation and underline the importance of dynamic shearing strength measurements.

Keywords: Energetic Materials, Sucrose, Pressure Shear Plate Impact (PSPI), Polymer-bonded explosives, Thermodynamics, Adiabatic Shear Band, Mie-Gruneisen equation of state, Complete Equation of State

1 Introduction

An energetic crystal is one with a large amount of stored chemical energy that can be released over a very short duration of time. Energetic crystals such as octahydro-1,3,5,7-tetranitro-1,3,5,7-tetrazocine (HMX), cyclotrimethylene trinitramine (RDX), 2,4,6-Trinitrobenzene-1,3,5-triamine (TATB), etc. play important roles in military and space applications, construction and mining. Energetic crystals are routinely employed as a solid fuel in rocket propellants and in mining and construction. One of the important classes of energetic materials is polymer-bonded explosives (PBXs), which are composites of energetic crystals held together by a small fraction (typically ~2-10%) of a polymeric binder. The presence of the binder in these granular composites imparts reduced shock sensitivity, which allows safer transportation and storage and minimizes accidental events like sympathetic detonations. There has been a great deal of interest in developing "insensitive munitions" in recent years, which motivates a systematic study of ignition mechanisms in energetic materials under controlled conditions. It is generally accepted that ignition in energetic materials begins in localized regions of high temperature known as 'hot-spots' (Bowden and Yoffe, 1958, 1952), which are formed when localized mechanical energy is converted into heat. Since the mechanical behavior, microstructure and composition of PBXs affect their impact sensitivity and propensity for ignition, it is imperative to study their mechanical response and that of their constituents under high pressure and high strain-rate loading conditions of relevance.

In the study of PBXs, energetic crystals like HMX and RDX are often replaced by simulant crystals such as sucrose, melamine and acetaminophen. A simulant crystal is a molecular crystal that closely resembles an energetic crystal in terms of one or more relevant attributes such as crystal structure, density and mechanical properties. For example, sucrose and acetaminophen are simulants for HMX due to their similar monoclinic crystal structure. β-HMX crystals have $P2_1/c$ ($P2_1/n$) symmetry with unit cell dimensions of $a = 6.54$ Å$, b = 11.05$ Å$, c = 8.70$ Å$, \beta = 124.3^0$ (Miller and Garroway, 2001). Sucrose also belongs to the $P2_1$ space group with cell dimensions of $a = 10.89$ Å$, b = 8.69$ Å$, c = 7.77$ Å$, \beta = 103^0$ (Beevers et al., 1952). Sucrose has also been shown to have mechanical behavior similar to that of HMX, RDX and pentaerythritol tetranitrate (PETN) under drop-weight impact (Heavens and Field, 1974) and a similar shock Hugoniot as HMX (Sheffield et al., 1998). These similarities have resulted in sucrose being a commonly used energetic material simulant. Sucrose has not only been used as a mock energetic crystal in the energetic materials industry but has also found an important application in the pharmaceutical industry as a model material to study

compaction processes (Duncan-Hewitt and Weatherly, 1990), where the use of sucrose offers insights into fracture in chipping, capping and delamination in such compaction processes. Due to their inert nature, energetic simulants provide a safe and cost-effective way to infer the mechanical behavior of real energetic crystals, which makes them suitable for many laboratory settings. Another advantage of studying energetic simulants is that they allow decoupling of mechanical and chemical behaviors of energetic crystals so that one can understand the mechanical signatures of phenomena such as pore collapse, adiabatic shear localization, fracture and granular friction independent of the effects of the accompanying chemical reaction in an actual energetic material (Sheffield et al., 1998). Moreover, it should be noted that several properties of energetic crystals are not adequately characterized, including: (a) the melt curve as a function of pressure, (b) the thermal conductivity of the solid phase as a function of pressure and temperature, (c) the specific heat capacity of the liquid phase as a function of pressure and temperature, (d) viscosity in the liquid phase as a function of pressure and temperature, and (e) the anisotropy of yield surface. Some of these properties are difficult to measure experimentally because of the onset of chemical decomposition and a subsequent reaction under extreme conditions. However, all the above properties are important for accurate modeling of the mechanical behavior of energetic crystals under large deformations and accurate prediction of ignition from hot-spot formation. Simulant crystals like sucrose offer an opportunity to provide reference values and trends for the relevant material properties of real energetic crystals.

Due to their mechanical and chemical fragility, characterization of molecular crystals using traditional testing methods is challenging. Brittle molecular crystals, such as RDX, HMX, PETN, sucrose, etc., fracture readily because they cannot be subjected to large strains or plastic deformation. Moreover, characterization methods such as electron microscopy are difficult to use on these materials for quantitative assessment as they chemically dissociate under an electron beam. Hence, not much is known about the deformation behavior of molecular crystals and the underlying deformation mechanisms. As a result, researchers have been left with only a handful of experimental methods to characterize these materials in the quasi-static limit. Nano-indentation and atomic force microscopy (AFM) have been used to extract the elastic moduli and hardness of sucrose (Duncan-Hewitt and Weatherly, 1989; Masterson and Cao, 2008; Ramos and Bahr, 2007). Apart from mechanical and chemical fragility, molecular crystals are difficult to analyze and characterize experimentally because of other complex features such as anisotropy and phase transformations. For example, β-HMX has a monoclinic crystal structure with 13 elastic constants (Stevens and Eckhardt, 2005; Zaug, 1998). Similar measurements of the elastic constants of RDX (Haussühl, 2001; Haycraft et al., 2006; Schwarz et al., 2005) showed large anisotropy of elastic properties along different orientations. Anisotropy in crystallographic slip results in a varying mechanical response when shocked in different orientations. Dick et al. (2004) demonstrated the anisotropy in strength and elastic precursor decay of β-HMX single crystals when shocked in different orientations. The inelastic mechanisms of deformation have also been shown to vary with orientation. Similarly, Hooks et al. (2006) showed that elastic wave speeds, Hugoniots and plastic wave relaxation rates are highly anisotropic for shocked RDX single crystals. Such a large anisotropy in the elastic and plastic properties of energetic crystals requires extensive experimental characterization for reliable constitutive models.

A great deal of work has been done over the past few decades to understand the compressive response of PBXs (Funk et al., 1996; Gray III et al., 1998; Idar et al., 1998) and their polymer-bonded simulants (PBSs) (Funk et al., 1996; Hu et al., 2015; Idar et al., 1998; Kendall and Siviour, 2015; Liu et al., 2011; Siviour et al., 2008; Williamson et al., 2006). While mechanical testing of PBSs under extreme conditions has received substantial attention, modeling of the phenomena leading to hot-spot formation in PBXs and PBSs requires accurate constitutive modeling of the constituents, which is lacking. The mechanical response of energetic crystals such as HMX and RDX has been studied in detail under uniaxial strain through normal compression impact experiments (Dick et al., 2004; Hooks et al., 2006). However, a systematic characterization of the shear strength of energetic crystals and their simulants has not been done so far. Despite being the most widely used simulant, sucrose has not been sufficiently characterized to inform constitutive models adequately. Trott et al. (2007) investigated the response of granular sugar under shock compression for different sample thicknesses, impact velocities and particle size distributions. A shock Hugoniot has also been reported by Sheffield et al. (1998). However, these studies are insufficient to model the strength response of sucrose as a function of pressure and strain-rate. At present, there is insufficient experimental data to develop an accurate anisotropic elastic-viscoplastic model of sucrose. It is difficult to develop even a sufficiently robust isotropic model for polycrystalline sucrose or a sufficiently large aggregate of sucrose grains, which can adequately model large deformations under high pressures and high strain rates. The absence of any shear strength measurements makes it difficult to perform realistic simulations of deformation and phenomena such as pore-collapse, shear localization and friction that lead to hot-spot formation. Granularity of the

specimen further hinders the ability to probe the bulk material response of sucrose. The effect of the granular nature of the specimen is evidenced by the very different normal velocity profiles for the same impact velocities observed by Trott et al. (2007). For these reasons, we employ the Pressure-Shear Plate Impact (PSPI) technique in the present work to measure the material response of a uniform sucrose layer to normal and shear loading.

Adding to the complexity of the mechanical behavior of molecular solids, it has been reported that under high pressures, temperatures and shear strains, molecular solids can undergo phase transformations. Ciezak-Jenkins and Jenkins (2018) and Patyk et al. (2012) reported an isostructural phase transformation in sucrose at a pressure of ~5 GPa, using a diamond anvil cell. Ciezak-Jenkins and Jenkins (2018) subjected sucrose samples to large shear strains at high pressures using a rotational diamond anvil cell and showed that amorphization occurs under such loading conditions. However, the diamond anvil cell studies do not quantify the shear strains and rates of loading and hence do not provide the necessary quantitative information to develop material models. Therefore, in the present work, we lay an experimental foundation using the PSPI experiments for the constitutive modeling of sucrose. In addition to being the first undertaking to study the high pressure and high strain-rate strength of sucrose, the experimental results also reveal the propensity of sucrose to undergo shear localization. Such findings beg for more experimental effort on real energetic crystals such as HMX and RDX under PSPI loading.

Since the response of molecular crystals to mechanical loading is inherently complex, constitutive models for energetic crystals and simulants are complex as well. In general, in order to model the material response and capture the physics behind phenomena such as pore collapse and subsequent chemical reactions, it is imperative to retain a sufficiently general model, albeit at the expense of complexity and computational resources expended. A general material model for such molecular crystals should incorporate: (a) a finite deformation framework, (b) non-linear anisotropic thermo-elasticity, i.e., have anisotropic elastic moduli which are dependent on pressure and temperature in general and be able to handle finite non-linear elastic deformations under large pressures through a complete equation of state, (c) plastic anisotropy, typically modeled using a crystal plasticity approach, and (d) thermo-elastic heat generation and plastic dissipation. Multiple researchers have taken up the task of including one or more of the above-mentioned features into the constitutive modeling of materials subject to extreme dynamic environments. Since the applications of interest involve large deformations, only finite deformation models are reviewed here. Barton et al. (2009) employed an anisotropic thermo-elastic model coupled with crystal plasticity to model pore collapse in HMX, although pressure and temperature-dependent moduli were not used and a constant specific heat capacity was assumed. Austin et al. (2015) extended the model by Barton et al. (2009) to incorporate a temperature-dependent specific heat and coupled chemical kinetics to simulate pore-collapse and consequent shear band formation. The effects of including crystal anisotropy and rate-dependent viscoplasticity on shear band formation were analyzed, and it was shown that a rate-independent model does not lead to shear band formation during the pore-collapse process, thus altering the mechanical signatures and subsequent chemical decomposition reactions. Use of pressure-dependent elastic moduli (Becker, 2004; Grunschel, 2009; Wang et al., 2016) enables capturing large volumetric strains and the evolution of shocks from steep pressure gradients. All the above references used crystal-plasticity to model the anisotropic plastic response. Clayton (2014) presented a thermodynamics-driven approach to modeling large deformations in hard anisotropic materials such as sapphire, diamond and quartz that incorporates all the aforementioned features of a general constitutive model. However, validating such a model requires a large number of experimentally characterized material constants which may not be feasible to obtain for most materials.

In the present study, we present a thermodynamically-consistent framework for finite deformation modeling of sucrose. The framework presented here is generic and can be used for any isotropic material subject to extreme dynamic environments involving high pressures, high strain-rates and large strains, both in compressive and shear loading scenarios. It enables the incorporation of a complete equation of state and a thermo-viscoplastic strength model in a thermodynamically-consistent manner, thus allowing an accurate representation of thermoelastic and thermo-viscoplastic work. Moreover, the use of logarithmic strains accompanied by an appropriate set of invariants (Criscione et al., 2000) allows the separation of stress into pressure and deviatoric terms. This is particularly useful in validating the model using experimental observations since the equation of state is measured through a separate set of experiments as compared to strength measurements. Due to a lack of experiments on sucrose, there is a lack of experimentally verified material constants. The present model uses a reasonable number of material parameters to address this problem.

The paper is organized into five sections. Section 2 details the experimental methods used and the results of PSPI experiments on sucrose. The shear behavior of sucrose is characterized under high shear strain-rates and high pressures. In

section 3, we present the thermodynamic framework used to model sucrose, followed by a description of the constitutive model and a derivation of a complete Mie-Gruneisen equation of state. Analytic expressions for different types of loading, such as isentropic, isothermal and shock loadings, are derived without any strength considerations, and the behavior of sucrose is compared under such conditions. The importance of using a temperature-dependent specific heat is highlighted for the case of shock loading. In section 4, we describe the numerical implementation of the material model and demonstrate that the proposed constitutive model is able to fit the experimental data reasonably well under varied testing conditions. Section 5 presents a summary of the dynamic shearing behavior of sucrose reported in the preceding sections and discusses possible avenues of further improvement on the experimental and modeling fronts.

2 Experiments

2.1 Methods

Pressure Shear Plate Impact (PSPI) experiments have been used to study the dynamic response of sucrose under extreme conditions. Pioneered by Kim et al. (1977), PSPI experiments allow investigation of the shearing response of materials under high pressures, high shearing strain-rates and high shear strains. In these experiments, a flyer plate impacts the target plate at an angle θ generating both compressive longitudinal waves and shear waves. The angle θ is usually kept below 20° to ensure that no slip occurs at the impact face. A 2.5-inch gas gun at the plate impact facility at Brown University is used for these experiments. The gun barrel has a keyway which facilitates oblique impacts. One of the most common test configurations is a sandwich configuration as shown in Fig. 1. In this configuration, a thin sample (typically 10-200 μm in thickness) is sandwiched between two hard elastic plates, hereafter, referred to as the front target plate and the rear target plate. The flyer and target plates are made from a hard material such as tungsten carbide or high strength steel, that remains elastic (or nearly so) over the range of loading pressures and strain rates reported herein. Upon impact a one-dimensional plane-wave loading is obtained. This loading allows for a comparatively straightforward interpretation of the stress-state achieved inside the specimen.

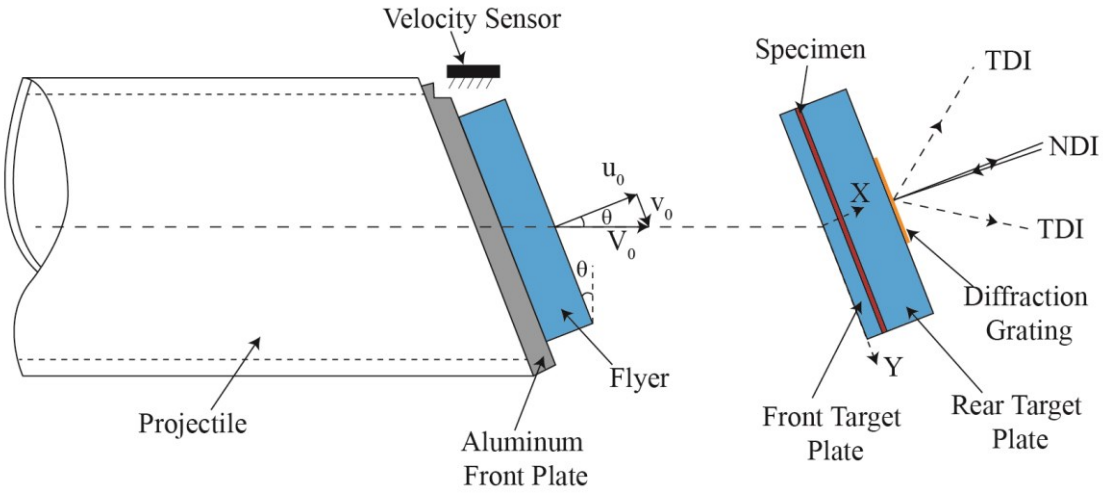

Fig. 1 PSPI Experimental Set-up. The projectile is typically a light-weight fiberglass tube. A flyer plate is glued to an aluminum plate bonded to the front of the projectile. A flat step is made on the aluminum front plate perpendicular to the impact direction. This step is used to short the pins of the velocity sensor that is used to measure the velocity of the projectile. The velocity sensor consists of five pins, placed at an angle of ~110° to the impact direction. Rotation of the projectile is prevented by a key, attached to the projectile and sliding in a keyway in the gun barrel. The flyer plate and the target assembly are aligned for impact of parallel plates with an angle, θ, between the normal direction to the impact plane and the direction of approach. Plane compressive and shear waves are generated at the impact face. A thin specimen, sandwiched between two hard elastic plates (target plates), is loaded by the forward propagating plane waves emanating from the impact plane. Particle velocities at the free surface are measured using a combined normal and transverse displacement interferometer (NDI & TDI) (Kim et al., 1977). Transverse displacements are measured interfering two beams diffracted symmetrically by a diffraction grating deposited on the free surface of the rear target plate. A diffraction grating with 625 lines/mm is used in this study.

The *t*-*X* plot for a typical PSPI experiment with a sandwich configuration is shown in Fig. 2. The impact occurs at X=0 and t=0, where X refers to the Lagrangian coordinate along the thickness direction (as shown in Fig. 1) in a reference

configuration and *t* represents time. On impact, longitudinal and shear waves are sent through the front target plate and the flyer. Due to low acoustic impedance of the specimen, these waves reverberate through the specimen before the stress state rings-up to a uniform value. Note that the thickness of the front target plate is chosen so that the compressive stress in the specimen has rung-up to a uniform value before the arrival of the shear wave. Hence, the measurement of the shear strength of the specimen is made at a state of nominally constant normal stress. The time window of shear loading at a constant normal stress is cut short by the earliest arrival of the unloading wave from the free surface of the rear target plate or the unloading wave reflected from the rear face of the flyer, as shown in Fig. 1. On impact, cylindrical unloading waves are generated at the circumference of the plates due to traction-free boundary conditions. When these waves reach the point being monitored on the free surface of the rear target plate, displacements can no longer be interpreted as caused by one-dimensional plane waves. The record is discarded beyond this point. The thickness of the rear target plate and the flyer are chosen to maximize the shear window. Typically, a shear window of 0.75-1 μs is achieved, which allows large shear strains of 1-10 for shear strain rates of 10^6-10^7 s^{-1}.

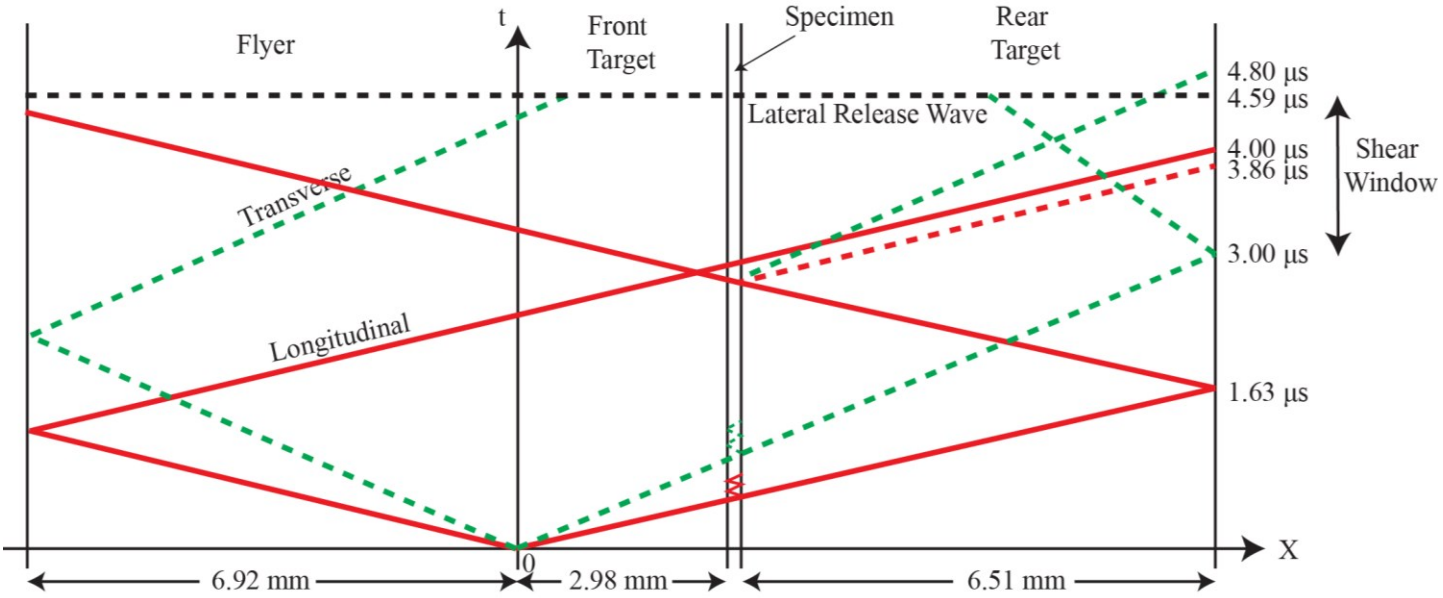

Fig. 2 A typical t-X plot for a PSPI experiment (Shot1 is depicted here. See Section 2.3 for details). Solid red lines represent the longitudinal wave characteristics and dashed green lines represents the shear wave characteristics. The dashed red line represents the transients reflected from the rear target/specimen interface. The horizontal black ~~dotted~~ dashed line represents the lateral release wave. The shear window in the scenario depicted here is limited by the lateral release wave.

If the flyer and target plates respond elastically, velocities and tractions at the sample/rear target plate interface can be inferred from the free surface velocity measurements made on the rear target plate. For such a case, normal and shear stresses in the sample can be obtained using a characteristic analysis for one-dimensional elastic wave propagation. The normal and shear stresses can be inferred from particle velocity measurements made at the free surface, as given through the following expressions:

$$\sigma_{sp} = -\frac{\rho_0 c_L u_{fs}}{2}, \qquad \tau_{sp} = -\frac{\rho_0 c_S v_{fs}}{2}. \tag{2.1}$$

Here, σ and τ represent normal and shear stresses respectively; u and v represent normal and transverse particle velocities; c_L and c_S are the longitudinal and shear wave speeds in the target and flyer material; and ρ_0 is the initial density of the target plate and flyer material. The subscript '*sp*' indicates specimen and '*fs*' stands for free surface. After a sufficient number of reverberations, a nominally uniform state of stress is obtained through the thickness of the sample as given by: $\sigma_{sp} = -\frac{\rho_0 c_L u_0}{2}$, where $u_0 = V_0 \cos(\theta)$ and V_0 is the impact velocity. However, the shear stress may not ring up to the peak value of $\tau_{sp} = -\frac{\rho_0 c_S v_0}{2}$ (where $v_0 = V_0 \sin(\theta)$) if the sample deforms plastically in shear. Then, the velocity difference between the front and back of the specimen leads to a shear strain rate given as:

$$\dot{\gamma} = \frac{v_0 - v_{fs}}{h_s}, \tag{2.2}$$

where h_s is the specimen thickness. The expression for the strain rate in equation (2.2) is valid only after the specimen has reached a state of constant shear stress. The shear strain-rate can then be integrated to yield the shear strain. In cases in which the anvil material does not respond elastically, its constitutive response needs to be characterized beyond the elastic limit and an inverse analysis used to infer velocities at the sample/rear target plate interface from the experimentally measured free surface velocities at the rear target plate. Such an inverse analysis has been provided by Clifton et al. (2020).

The above analysis assumes an ideal condition of perfectly parallel impacting surfaces. However, there is always a finite amount of tilt between the flyer and the target plate. It is important to keep the tilt as low as possible, typically a value below 2 mrad is desired. In order to achieve such low tilt angles, a high precision alignment technique was invented by Kumar and Clifton (1977). Alignment of the flyer to the sandwich consists of two steps: a coarse alignment step and a fine alignment step. In the coarse-alignment step, the flyer and the sandwich are brought in contact and the degrees of freedom of the sandwich adjusted to ensure no gaps and a complete overlap of the impacting surfaces. This is followed by a fine alignment step that uses a partially-mirrored, 90° precision-prism. The procedure is described in detail in Kumar and Clifton (1977). An alignment precision as small as 0.02 mrad is achieved using this method. In order to confirm if a shot is valid, the tilt is measured by recording times of contact of the flyer with tilt pins lapped flush with the target impact surface (Klopp and Clifton, 1990).

2.2 Specimen Preparation

A uniform thin layer of crystalline sucrose is prepared on the front target plate by spin-coating a super-saturated solution of sucrose in de-ionised water. Pure sucrose from Sigma Aldrich is used rather than a commercial variety of sugar. An 80% w/w solution of sucrose in water is prepared and degassed. The solution is spin-coated on the substrate at 4000 rpm. The substrate is placed on a hot plate at ~60 ^{0}C for ~12-16 hours until all water has evaporated, and the sucrose has crystallized. As shown in Fig. 3, it is important to stay above the metastability limit (in Zone III) for crystallization to occur. A moist environment and a rough substrate are found to favor grain nucleation and growth. Once the sucrose layer is prepared on the front target plate, the rear target plate is placed on top of the sucrose specimen and the sandwich is glued on the periphery of the sample/target plate interface with an epoxy while gently pressing with a small weight. During PSPI experiment, slip is prevented by the large compressive normal stress.

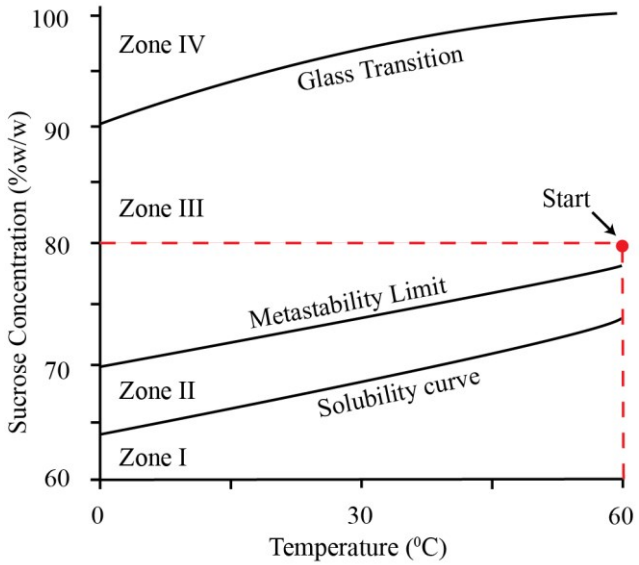

Fig. 3 Sucrose concentration (% weight of solid) vs temperature (The data for the figure was taken from Shastry and Hartel (1996)). Zone I: Under-saturated solution, Zone II: Meta-stable solution, Zone III: Labile solution, Zone IV: Amorphous state. Sucrose crystallization begins above the metastability limit. So, for a solution heated at 60°C, a starting solution concentration of 80% is chosen.

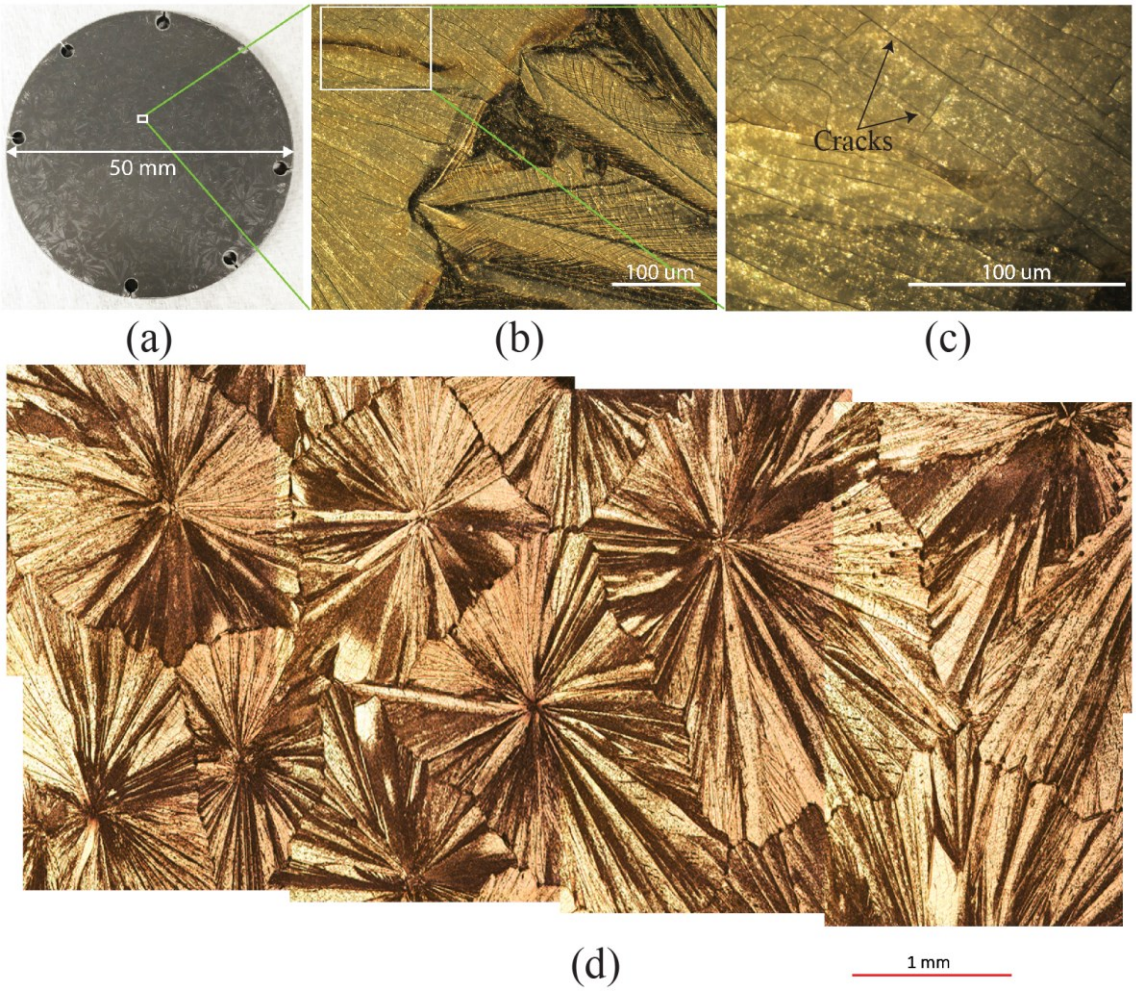

Fig. 4 (a) WC front target plate (diameter = 50 mm) with a 15 μm thick uniform layer of sucrose spin-coated on top. (b), (c) Magnified views of a spot on the sample and (d) a stitched version of microscope images indicating sucrose grain boundaries.

A sample obtained by following the above preparation process is shown in Fig. 4. The sample thickness is measured using a Dektak profilometer. A sucrose layer of 10-20 μm in thickness can be obtained by this method, which facilitates large shear strain rates of the order of 10^6 s^{-1}. Note that the specimens are not perfectly flat and have a surface roughness of the order of a micron. On cooling, cracks are observed on the sample, as shown in Fig. 4(b) and (c), due to a large mismatch between the coefficient of thermal expansion of the substrate and that of sucrose. However, the width of these cracks is extremely small as indicated by the scale bar and are not significant in the PSPI experiments. Fig. 4(d) depicts a polycrystalline layer of a sucrose specimen with a grain size of the order of a few microns. Another critical issue of interest is the crystallinity of the sucrose layer. To ensure that the sucrose layer prepared by the spin-coating method is crystalline, X-Ray Diffraction (XRD) studies are carried out on powdered crystalline sucrose and spin-coated sucrose layers (see Fig. 5). An overlap of XRD peaks of the spin-coated specimen and that of crystalline powdered sugar shows that the spin-coating method indeed yields a crystalline layer. Fig. 5(a) shows that XRD intensity peaks for different spin-coated samples overlap, indicating consistency across different samples and different spots on the same sample. It is evident from Fig. 5(b) that the spin-coated sample shows most of the peaks corresponding to powdered sucrose although with lower relative intensities. So, it is reasonable to conclude that spin-coating gives a crystalline sample.

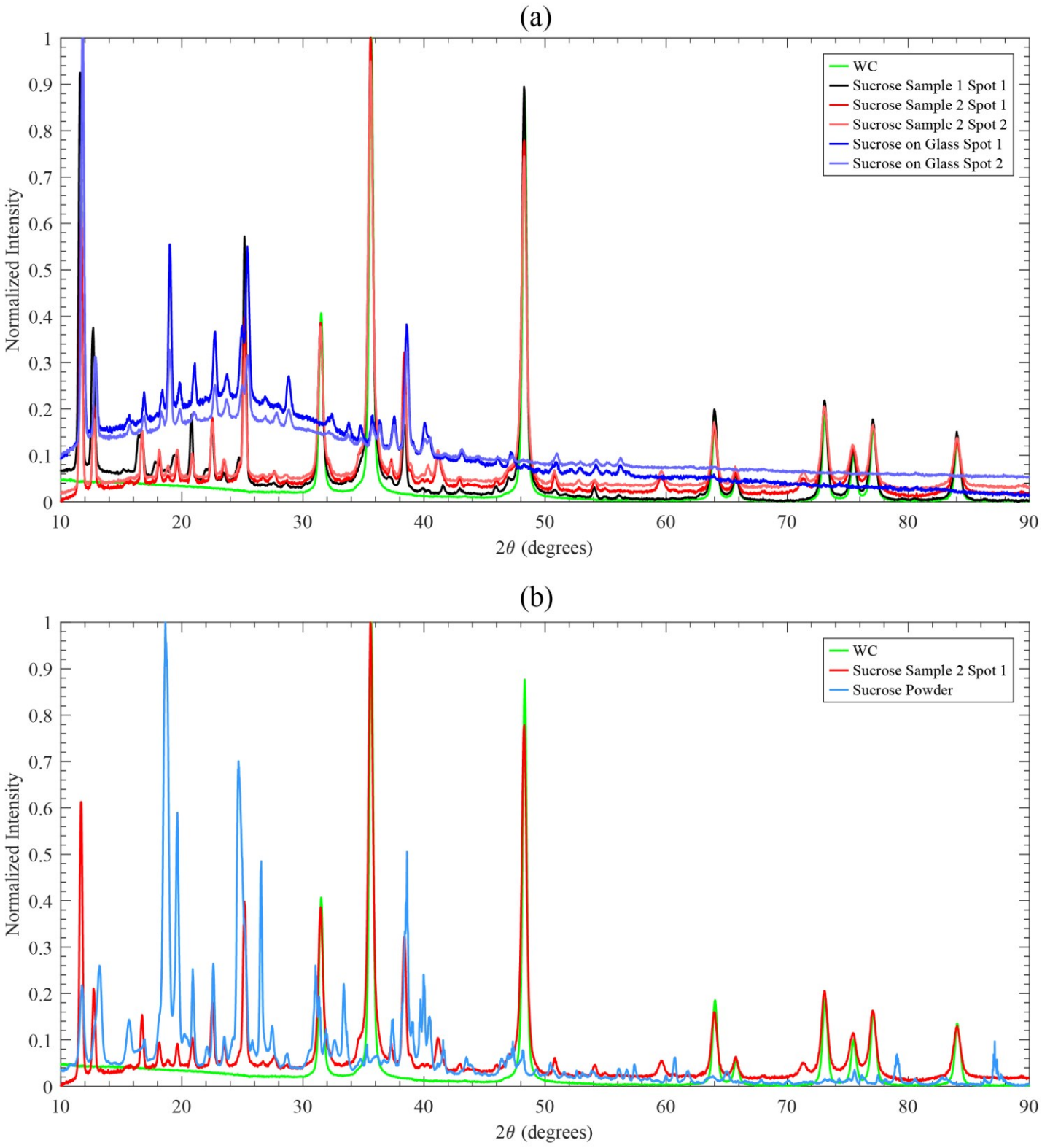

Fig. 5 (a) XRD intensity plot for spin-coated sucrose samples. XRD graphs of WC, spin-coated samples on WC and spin-coated samples on an amorphous glass substrate are compared to isolate intensity peaks corresponding to sucrose. (b) XRD intensity plot for WC, a spin-coated sucrose sample on a WC substrate and sucrose powder. The spin-coated sample shows most of the peaks displayed by the crystalline sucrose powder, albeit at a lower intensity. Graphs in (a) and (b) are shifted along the intensity axis for clarity.

2.3 Experimental Results

A total of seven PSPI shots have been conducted on sucrose. A summary of the shots is provided in Table 1. D2 steel is used as the anvil material for the low normal stress (nominally 3 GPa) shots, while WC is used for the high normal stress (nominally 9.5 GPa) shots. Shear strain rates of the order of 10^6 s^{-1} are obtained as a result of using a small sample thickness of 10-20 μm.

Table 1 Summary of PSPI shots on sucrose

Shot No.	**Target Material**	h_S (μm)	h_F (mm)	h_{FT} (mm)	h_{RT} (mm)	θ	V_0 (m/s)	**Tilt (mrad)**	σ_{max} (GPa)	τ_{max} (GPa)	$\dot{\gamma}$ (s^{-1})
Shot1	D2 Steel	12.05	6.915	2.978	6.511	18°	132.06	1.21	2.82	0.382	$1.95x10^6$
Shot2	D2 Steel	12.63	6.94	2.951	6.522	18°	134	NA	2.9	0.442	$1.7x10^6$
Shot3	D2 Steel	16.97	6.965	2.944	6.571	18°	133.46	1.02	2.93	0.404	$1.55x10^6$
Shot4	WC	17.6	6.443	2.886	5.872	18°	187	0.5	9.1	0.460	$2.9x10^6$
Shot5	WC	16.91	6.324	2.855	5.986	18°	194.5	0.8	9.75	0.288	$3.1x10^6$
Shot6	WC	13.58	6.369	2.937	5.934	18°	191.9	0.37	9.64	0.580	$3.98x10^6$
Shot7	WC	18.24	6.335	2.914	5.940	18°	188.52	0.97	9.47	0.530	$2.95x10^6$

h_S: sample thickness h_F: flyer thickness, h_{FT}: front target plate thickness, h_{RT}: rear target plate thickness, θ: angle of impact, V_0: impact velocity, σ_{max}: peak normal stress, τ_{max}: peak shear stress, $\dot{\gamma}$: mean shear strain-rate

Fig. 6 shows the normal stress profiles, and the shear stress profiles are plotted in Fig. 7. Saturation normal stresses of ~3 GPa and ~9.5 GPa are nominally obtained for the low and high velocity shot categories. The normal stress profiles show an elastic precursor as indicated by the initial step. Following the elastic precursor, the normal stress profiles for the low-pressure shots rise steeply to the plateau with a rise time of approximately 86 ns. For the high-pressure shots, the initial rise after the elastic precursor is steep but a bend is observed at a normal stress of ~6 GPa, which could be a result of the anvil material (WC) reaching its Hugoniot elastic limit (HEL). No steps corresponding to the ring-up of normal stress are observed despite the large acoustic impedance mismatch between the anvil material and sucrose because the sucrose layers are extremely thin. Instead, the normal stress rises steeply to the saturation value.

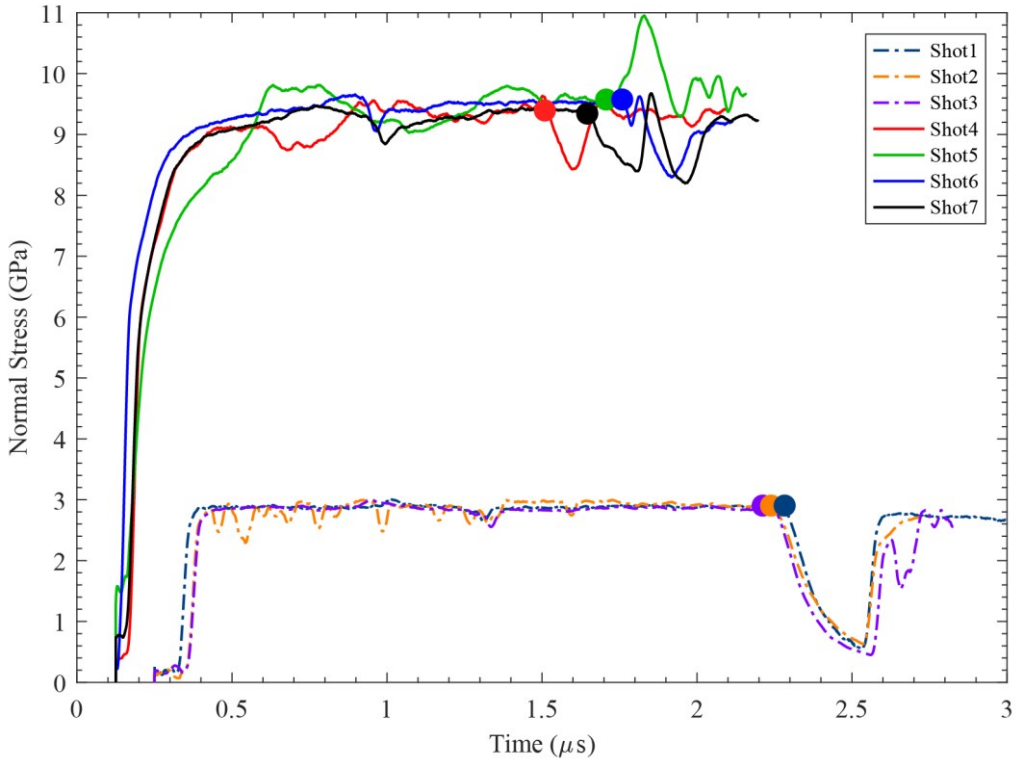

Fig. 6 Normal stress vs time profiles for all PSPI shots on sucrose. Solid lines show the high-pressure shots while dashed lines show the low-pressure shots. Low and high-pressure shots are laid on top of each other for a better comparison and to demonstrate the consistency of normal behavior across different shots. The arrival of the unloading wave is marked by a dot for each case.

The shear behavior offers more interesting insights into the mechanical behavior of sucrose under high pressures and high shear strain-rates ($>10^6$ s^{-1}). The shear stress rises to a peak value followed by pronounced strain softening. Under these loading conditions, sucrose loses its shearing resistance after accumulating a certain amount of shear strain. For the low-pressure case (Fig. 7 (a)), the shear stress profiles are quite repeatable. For the high-pressure case (Fig. 7 (b)), two shots (Shot4 and Shot7) show almost identical shear behavior. However, for Shot 5, the peak shear strength is much lower than the other shots and shows a complete loss in shear strength, the reason for which is not fully understood. It is possible that this particular specimen had pre-existing defects such as voids which collapse upon the arrival of the shear wave, leading to more damage than would be expected in a nominally homogeneous defect-free specimen, and hence leading to complete shear failure. The shear stress profile for Shot6 is not plotted since the data for that shot is very noisy due to the low signal to noise ratio of the transverse displacement interferometer (TDI). Overall, the high-pressure shots exhibit more variability in the shear stress data compared to the low-pressure shots. However, both cases show qualitatively similar behavior. Also note that as the transverse velocity reduces to a very small value after shear strain-softening, the shear-stress profiles become noisy due to the low signal to noise ratio of the TDI signal thereafter.

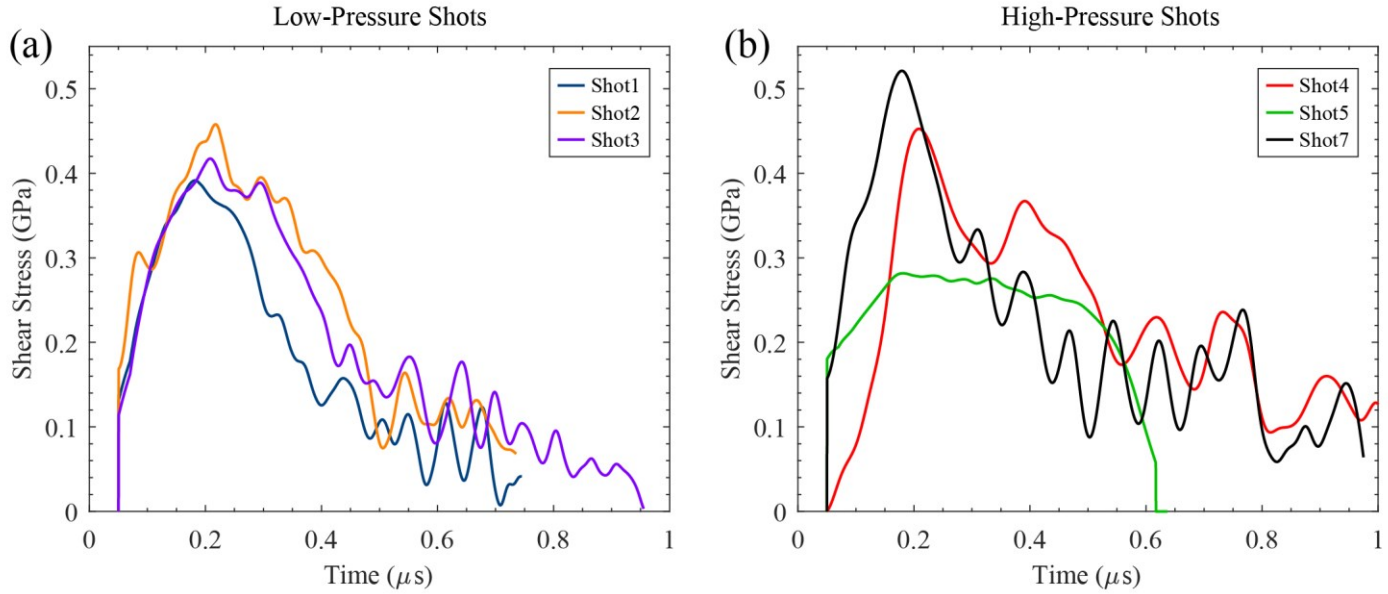

Fig. 7 Shear stress vs time profiles for (a) low-pressure shots and (b) high-pressure shots on sucrose. Low and high-pressure shots are laid on top of each other for a better comparison and to demonstrate the consistency of shear behavior across different shots. The arrival of the longitudinal unloading wave occurs at times latter than depicted here for each case. Note that the high frequency oscillations at the end of the shear profiles are a result of low signal to noise ratio of the TDI signal.

The dramatic drop in shear strength of sucrose can be attributed to a thermo-viscoplastic instability leading to localized shearing deformation and possibly melting in the sucrose sample. Such behavior is modeled using the constitutive model described in Section 3. A simple calculation of the amount of plastic work due to shear converted to heat ($= \int \beta \, \tau d\gamma$) suggests a significant increase in temperature. Here $\int \tau d\gamma$ is the amount of plastic work due to shearing deformation, and β is the fraction of plastic work converted to heat. For example, assuming homogeneous deformation across the specimen in Shot4 and taking $\beta = 0.9$ and ambient values of the specific heat ($1244\ J/kgK$) and density of sucrose ($1580.5\ kg/m^3$), a temperature increase of approximately 286℃ is expected. The thermal softening eventually overtakes the strain and strain-rate hardening, leading to localized deformation. Such localized failure through the formation of adiabatic shear bands has been observed in molecular solids such as RDX (Coffey and Sharma, 2001; Sharma et al., 1996; Sharma and Coffey, 1996). Sharma et al. (1996) and Sharma and Coffey (1996) used Atomic Force Microscopic (AFM) imaging to illustrate the lattice and molecular deformations in RDX resulting from drop-weight loading. AFM images of an RDX single crystal subject to an aquarium shock of 12.9 GPa magnitude by Sandusky et al., (1993) were shown in Coffey and Sharma (2001). AFM images of recovered samples showed that shear bands with widths of several tens of microns formed along crystal slip planes and extended for hundreds of microns. It was also shown that RDX melted locally within the shear bands, flowed out of the bands and solidified on the crystal surface. Molecular dynamics studies of shock-loaded HMX (Jaramillo et al., 2007) and RDX (Cawkwell et al., 2008) also showed the formation of nano-shear bands at 45^0 to the direction of impact. However, quantitative measurements of the peak shear stress at which shear bands formed were not made in any of the above studies.

Peak shear stresses in sucrose exhibit some variability for a given normal stress. The variability is low for the low normal stress case. However, in general, the peak shearing resistance of sucrose seems to be very weakly dependent on normal stress, as shown in Fig. 8.

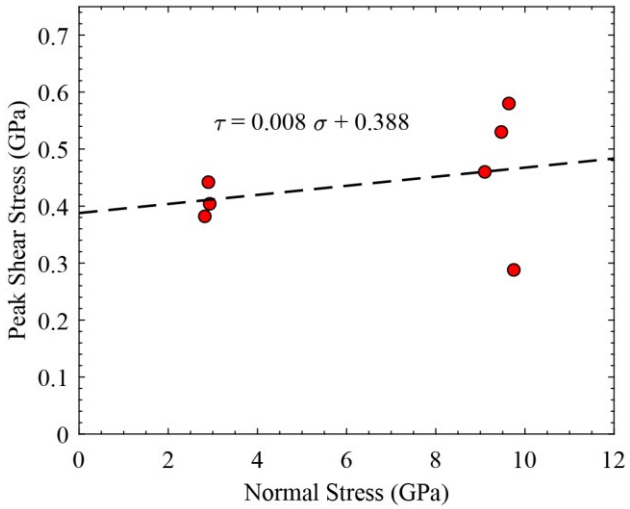

Fig. 8 Peak shear stress of sucrose vs normal stress at a nominally similar shear strain rate. The dashed line indicates a linear fit to the experimental data. The equation of the linear fit is displayed above the trendline. Note that substantial temperature increase is expected due to normal compression and therefore, the peak shear stress is expected to depend on temperature as well. Hence, the plot shows the coupled effect of normal stress and temperature rather than normal stress alone.

Shear strain-rate curves are plotted for low and high-pressure shots on sucrose in Fig. 9 (a) and (b), respectively. Mean shear strain-rate values for the low-pressure shots lie in the $\sim 1.5 \times 10^6 - 2 \times 10^6\ s^{-1}$ range while the mean shear strain-rates for high-pressure shots are slightly higher ($\sim 2.9 \times 10^6 - 3.1 \times 10^6\ s^{-1}$). The shear strain-rate values calculated here should be taken with caution as they assume that deformation in the specimen is homogeneous and the shear stress has equilibrated. Due to the extremely small thickness of the specimen, shear stress equilibrium can be attained fairly quickly. However, strain localization is suspected inside the specimen after the fall in shear strength. For such inhomogeneous deformations, the shear strain-rate plots shown here do not represent the actual strain-rate inside the specimen. So, the shear strain-rate and the consequent integrated shear strain values are only nominal proxies of actual values. Shear stress versus nominal shear strain behavior is plotted in Fig. 10. It can be observed that the shear stress begins to decrease around a nominal shear strain of ~ 0.2 for the low-pressure shots while the critical shear strain for high pressure shots is ~ 0.5, signalling the role of pressure in suppressing the onset of instability.

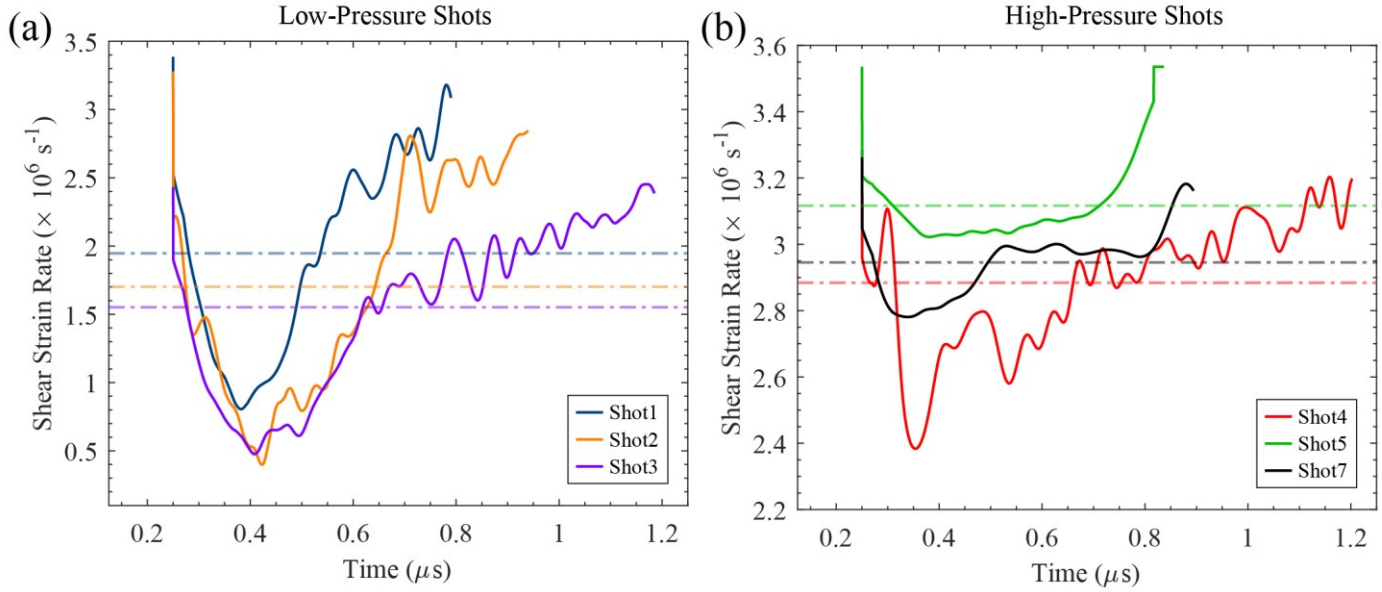

Fig. 9 Shear strain-rates for (a) low-pressure shots and (b) high-pressure shots. The mean shear strain-rate values for each shot are indicated by the light-colored dashed lines.

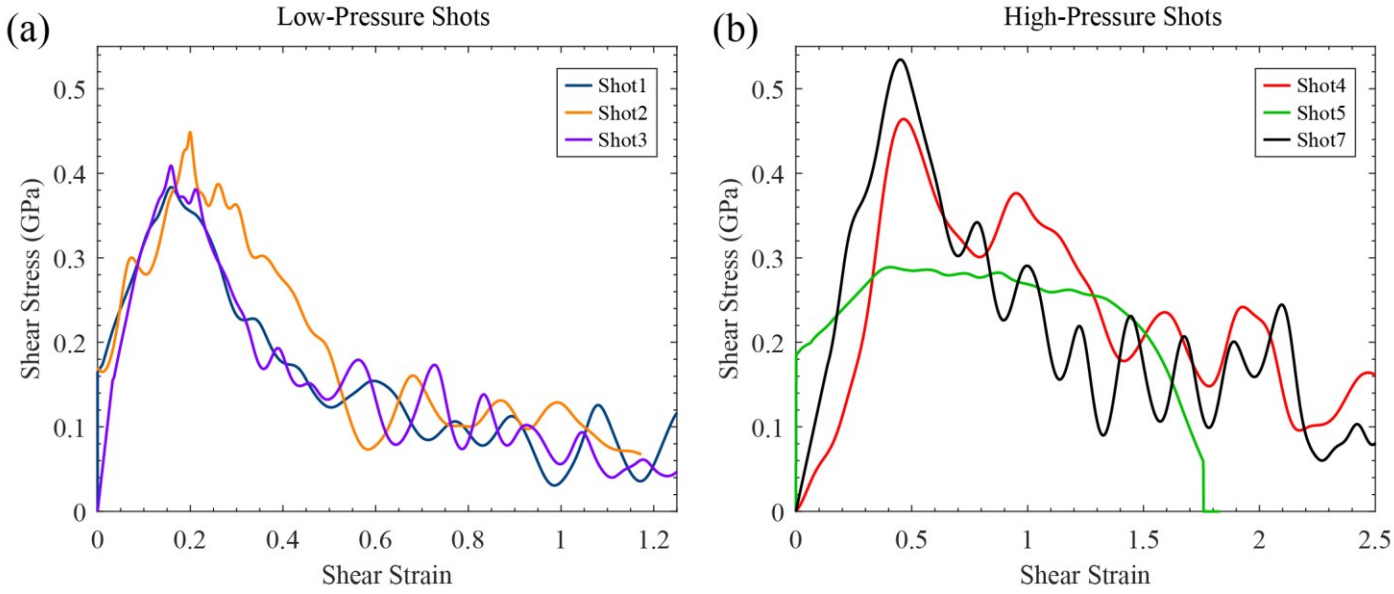

Fig. 10 Shear stress vs nominal shear strain for (a) low-pressure shots and (b) high-pressure shots.

This section presents an investigation of the shear strength of an energetic crystal simulant, i.e., sucrose, through PSPI experiments. A brief introduction to the PSPI experiments has been provided and methods for preparation of thin polycrystalline sucrose layers for PSPI experiments have been discussed in detail. PSPI experiments have been conducted at two different normal stresses of approximately 3 and 9.5 GPa and shear strain rates of the order of 10^6 s^{-1}. Under such loading conditions, sucrose loses its shear strength dramatically after reaching a peak value. Such softening of the shear response of sucrose may be attributed to a thermo-viscoplastic localized instability, which is discussed in a subsequent section. In the next section, we formulate a constitutive model for sucrose which not only captures the experimental observations from this section but can also be extended to other experimental loading scenarios.

3 Constitutive Model

This section focuses on developing a thermodynamically consistent framework for finite deformation modeling of sucrose. In Section 3.1, a thermodynamic foundation is laid for constitutive modeling of a solid. This is followed by a description of an isotropic thermoelastic, thermo-viscoplastic material model in Section 3.2. An isotropic model for sucrose is presented for two main reasons, apart from its simplicity: (a) a lack of characterization data for the anisotropic elastic constants of sucrose and (b) the use of polycrystalline samples in the PSPI experiments. The logarithmic strain is employed in the constitutive model for the thermoelastic response because the consequent Cauchy stress additively decomposes into volumetric and deviatoric parts even at finite strains, which is not possible when using the Green-Lagrange strain tensor (Barton et al., 2009; Becker, 2004). Such a decomposition makes it easier to handle the volumetric and deviatoric responses separately and to incorporate a complete equation of state into the framework. Since energetic crystals and their simulants are routinely subject to shock conditions, it is imperative to develop a material model that is able to faithfully represent the mechanical and thermal behavior under these conditions. As a result, a complete Mie-Gruneisen equation of state, with a temperature-dependent specific heat capacity, is derived and implemented in Section 3.3, laying the foundation for modeling the temperature-coupled elastic behavior under large pressures. In Section 3.1.6, it is shown that the temperature evolution equation involves two important terms, i.e., a rate of thermo-elastic heating and a rate of plastic dissipation, apart from thermal conduction, and in Section 3.4, an analytic expression for thermo-elastic heating is derived. Based on the complete equation of state, analytic expressions for different types of loading, namely, isentropic, isothermal and shock loading, are derived without strength considerations in Sections 3.5, 3.6 and 3.7, respectively and compared in Section 3.8. The complete Mie-Gruneisen equation of state uses an isothermal 3rd-order logarithmic equation of state as its reference curve. Appendix A presents a derivation for the 3rd-order equation of state using the logarithmic strain, consistent with our constitutive modeling approach (Note that the logarithmic equation of state was first derived by Poirier and Tarantola (1998)). Using logarithmic strains also has advantages at high pressures since a constitutive model based on logarithmic strains requires a smaller number of material constants to fit the experimental data (Anand, 1986, 1979; Clayton, 2014; Poirier and Tarantola, 1998). Note that the constitutive model for sucrose utilizes several material constants, not all of which are experimentally validated through PSPI experiments. Therefore, it is important to justify their choice based on experimental and theoretical observations of other researchers. The choice of material constants is discussed in detail in Appendix B.

In addition to the above, it must be noted that molecular crystals such as RDX, HMX and sucrose undergo complicated transformations, such as phase change and chemical decomposition under extreme environments. Adequate representation of such complex behaviors requires the consideration of additional physics and appropriate multi-phase models, which are not the focus of present work.

3.1 Thermodynamics of a Solid

3.1.1 Kinematics

Consider a body occupying a region of space $\mathcal{B}_0$ in the reference/undeformed configuration. The body is then subjected to a motion $\boldsymbol{x} = \boldsymbol{\chi}(\boldsymbol{X}, t)$ so that it occupies a region of space $\mathcal{B}_t$ at time t in the spatial/deformed configuration. The deformation gradient is then given by $\boldsymbol{F} = \boldsymbol{\nabla\chi}$ with $J = det(\boldsymbol{F}) > 0$, where $\boldsymbol{\nabla}$ denotes the gradient with respect to the material coordinate $\mathbf{X}$ in the undeformed body. We assume that the deformation gradient $\boldsymbol{F}$ is multiplicatively decomposed into elastic and plastic parts, $\boldsymbol{F}^e$ and $\boldsymbol{F}^p$, respectively (commonly referred to as the Kröner decomposition): $\boldsymbol{F} = \boldsymbol{F}^e\boldsymbol{F}^p$. It is assumed that $J^e \equiv det(\boldsymbol{F}^e) > 0$ and that the plastic deformation is incompressible, i.e., $J^p \equiv det(\boldsymbol{F}^p) = 1$, so that only the elastic deformation leads to a change in volume, i.e., $J^e = J$. The right polar decomposition of $\boldsymbol{F}^e$ is given as $\boldsymbol{F}^e = \boldsymbol{R}^e\boldsymbol{U}^e$, where $\boldsymbol{R}^e$ is the elastic rotation tensor and $\boldsymbol{U}^e$ is a symmetric positive-definite tensor, called the elastic right stretch tensor. The spatial velocity gradient $\boldsymbol{L}$ defined as: $\boldsymbol{L} \equiv \boldsymbol{grad}\, \boldsymbol{v} = \dot{\boldsymbol{F}}\boldsymbol{F}^{-1}$, where $\boldsymbol{grad}$ represents the gradient with respect to the spatial coordinate $\boldsymbol{x}$ in the deformed body. Using the Kroner decomposition of deformation, the velocity gradient can be decomposed as: $\boldsymbol{L} = \dot{\boldsymbol{F}}^e\boldsymbol{F}^{e-1} + \boldsymbol{F}^e\dot{\boldsymbol{F}}^p\boldsymbol{F}^{p-1}\boldsymbol{F}^{e-1} = \boldsymbol{L}^e + \boldsymbol{F}^e\boldsymbol{L}^p\boldsymbol{F}^{e-1}$, with $\boldsymbol{L}^e = \dot{\boldsymbol{F}}^e\boldsymbol{F}^{e-1}$ and $\boldsymbol{L}^p = \dot{\boldsymbol{F}}^p\boldsymbol{F}^{p-1}$. The elastic and plastic rate of stretching and spin tensors are defined as:

$$\begin{aligned} \boldsymbol{D}^e &\equiv sym(\boldsymbol{L}^e), \\ \boldsymbol{W}^e &\equiv skw(\boldsymbol{L}^e), \\ \boldsymbol{D}^p &\equiv sym(\boldsymbol{L}^p), \\ \boldsymbol{W}^p &\equiv skw(\boldsymbol{L}^p). \end{aligned} \tag{3.1}$$

It is assumed that plastic flow is irrotational, i.e., $\boldsymbol{W}^p = \boldsymbol{0}$, so that $\boldsymbol{L}^p = \boldsymbol{D}^p$.

3.1.2 First Law of Thermodynamics

The first law of thermodynamics states that the change in internal energy of an isolated system is equal to the work done on the system plus the heat added to the system. In the reference configuration, the local form of the first law is written as (Gurtin et al., 2010):

$$\dot{e_R} = \boldsymbol{T_0}\colon \dot{\boldsymbol{F}} - Div\,(\boldsymbol{q}_R) + r_R, \tag{3.2}$$

where e_R is the internal energy per unit reference volume, $\boldsymbol{q}_R$ is the referential heat flux vector and r_R is the heat supply per unit reference volume. Throughout, we use the subscript 'R' to denote referential quantities. The tensor $\boldsymbol{T_0}$ is the unsymmetric 1st Piola-Kirchhoff stress tensor, and $\boldsymbol{T}_0\colon \dot{\boldsymbol{F}}$ is the stress power per unit reference volume. The stress power can also be expressed in terms of the symmetric Cauchy stress tensor, $\boldsymbol{T} = J^{-1}\boldsymbol{T}_0\boldsymbol{F}^T$, as: $\boldsymbol{T}_0\colon \dot{\boldsymbol{F}} = J\boldsymbol{T}\colon \boldsymbol{L}$. Hence, the first law can be re-written as:

$$\dot{e_R} = J\boldsymbol{T}\colon \boldsymbol{L} - Div\,(\boldsymbol{q}_R) + r_R. \tag{3.3}$$

3.1.3 Second Law of Thermodynamics

The second law of thermodynamics states that the net entropy production of an isolated system is non-negative. The local form of the second law in the reference configuration is written as (Gurtin et al., 2010):

$$\delta_{\mathrm{R}} = \dot{\eta}_R + Div\left(\frac{\boldsymbol{q}_R}{\theta}\right) - \frac{r_R}{\theta} \geq 0, \tag{3.4}$$

where η_R is the entropy per unit reference volume, δ_R is the entropy production rate per unit reference volume, and θ is the absolute temperature.

3.1.4 Free-energy Imbalance

The Helmholtz free energy is related to the energy and entropy through $\psi_R = e_R - \eta_R\theta$, where ψ_R is the Helmholtz free energy per unit reference volume. Hence, the rate of change of free energy can be written as $\dot{\psi_R} = \dot{e_R} - \dot{\eta_R}\theta - \eta_R\dot{\theta}$. Combining with equation (3.3) and $\dot{\eta_R}$ from equation (3.4), we obtain the local free-energy imbalance inequality:

$$\dot{\psi_R} + \eta_R\dot{\theta} - J\boldsymbol{T}\colon \boldsymbol{L} + \frac{1}{\theta}\boldsymbol{q}_R \cdot \boldsymbol{\nabla}\theta = -\theta\delta_R \leq 0. \tag{3.5}$$

The quantity $\theta\delta_R$ represents dissipation rate per unit reference volume, and the free-energy imbalance requires that the dissipation rate is non-negative.

Next, consider the stress power term $J\boldsymbol{T}\colon \boldsymbol{L}$, which can be decomposed into elastic and plastic terms:

$$J\boldsymbol{T}\colon \boldsymbol{L} = J\boldsymbol{T}\colon \boldsymbol{L}^e + J\boldsymbol{T}\colon \boldsymbol{F}^e\boldsymbol{L}^p\boldsymbol{F}^{e-1} = J\boldsymbol{T}\colon \boldsymbol{D}^e + J\boldsymbol{F}^{e^T}\boldsymbol{T}\boldsymbol{F}^{e-T}\colon \boldsymbol{L}^p \tag{3.6}$$

Noting that $\boldsymbol{D}^e$ can be expressed as $\boldsymbol{D}^e = \frac{1}{2}\boldsymbol{F}^{e-T}\dot{\boldsymbol{C}}^e\boldsymbol{F}^{e-1}$, where $\boldsymbol{C}^e = \boldsymbol{F}^{e^T}\boldsymbol{F}^e$ is the right Cauchy-Green tensor, the stress power may be written as $J\boldsymbol{T}\colon \boldsymbol{L} = \left(J\boldsymbol{F}^{e^{-1}}\boldsymbol{T}\boldsymbol{F}^{e-T}\right)\colon \frac{\dot{\boldsymbol{C}}^e}{2} + \left(J\boldsymbol{F}^{e^T}\boldsymbol{T}\boldsymbol{F}^{e-T}\right)\colon \boldsymbol{L}^p$. Two additional stress measures are defined as:

$$\boldsymbol{T}^e = J\boldsymbol{F}^{e^{-1}}\boldsymbol{T}\boldsymbol{F}^{e-T}, \tag{3.7}$$

$$\boldsymbol{M}^e = J\boldsymbol{F}^{e^T}\boldsymbol{T}\boldsymbol{F}^{e-T} = \boldsymbol{C}^e\boldsymbol{T}^e, \tag{3.8}$$

where $\boldsymbol{T}^e$ is the symmetric elastic 2nd Piola-Kirchhoff stress, and $\boldsymbol{M}^e$ is the Mandel stress. Hence, the stress power can be re-written as:

$$J\boldsymbol{T}\colon \boldsymbol{L} = \boldsymbol{T}^e\colon \frac{\dot{\boldsymbol{C}}^e}{2} + \boldsymbol{M}^e\colon \boldsymbol{L}^p. \tag{3.9}$$

Re-writing the first law from equation (3.3) in terms of the stress measures introduced above, we have:

$$\dot{e_R} = \boldsymbol{T}^e\colon \frac{\dot{\boldsymbol{C}}^e}{2} + \boldsymbol{M}^e\colon \boldsymbol{L}^p - Div\,(\boldsymbol{q}_R) + r_R. \tag{3.10}$$

3.1.5 Thermoelastic Constitutive Equations and Thermodynamic Restrictions

The constitutive laws for ψ_R, η_R and $\boldsymbol{T}^e$ are assumed to be functions of the same set of variables $(\boldsymbol{C}^e, \theta, \boldsymbol{\nabla}\theta, \boldsymbol{\xi})$ where $\boldsymbol{\xi}$ represents the list of internal state variables:

$$\begin{aligned}\psi_R &= \hat{\psi}_R(\boldsymbol{C}^e, \theta, \boldsymbol{\nabla}\theta, \boldsymbol{\xi}),\\ \eta_R &= \hat{\eta}_R(\boldsymbol{C}^e, \theta, \boldsymbol{\nabla}\theta, \boldsymbol{\xi}),\\ \boldsymbol{T}^e &= \widehat{\boldsymbol{T}^e}(\boldsymbol{C}^e, \theta, \boldsymbol{\nabla}\theta, \boldsymbol{\xi}).\end{aligned} \tag{3.11}$$

The constitutive equation for the internal energy follows as $e_R = \hat{e}_R(\boldsymbol{C^e}, \theta, \boldsymbol{\nabla}\theta, \boldsymbol{\xi}) = \hat{\psi}_R(\boldsymbol{C^e}, \theta, \boldsymbol{\nabla}\theta, \boldsymbol{\xi}) + \hat{\eta}_R(\boldsymbol{C^e}, \theta, \boldsymbol{\nabla}\theta, \boldsymbol{\xi})\theta$. Taking the time derivative of the free energy, one obtains

$$\dot{\psi}_R = \frac{\partial \hat{\psi}_R}{\partial \boldsymbol{C}^e} : \dot{\boldsymbol{C}}^e + \frac{\partial \hat{\psi}_R}{\partial \theta}\dot{\theta} + \frac{\partial \hat{\psi}_R}{\partial \boldsymbol{\nabla}\theta} \cdot \dot{\overline{\boldsymbol{\nabla}\theta}} + \frac{\partial \hat{\psi}_R}{\partial \boldsymbol{\xi}} * \dot{\boldsymbol{\xi}}, \tag{3.12}$$

where '$*$' denotes the appropriate scalar product considering the order of $\boldsymbol{\xi}$. Using equation (3.5), the rate of change of the free energy can also be written as:

$$\dot{\psi}_R = \boldsymbol{T}^e : \frac{\dot{\boldsymbol{C}}^e}{2} + \boldsymbol{M}^e : \boldsymbol{L}^p - \eta_R\dot{\theta} - \frac{1}{\theta}\boldsymbol{q}_R \cdot \boldsymbol{\nabla}\theta - \theta\delta_R. \tag{3.13}$$

From equations (3.12) and (3.13),

$$\left(\frac{\partial \hat{\psi}_R}{\partial \boldsymbol{C}^e} - \frac{1}{2}\boldsymbol{T}^e\right) : \dot{\boldsymbol{C}}^e + \left(\frac{\partial \hat{\psi}_R}{\partial \theta} + \eta_R\right)\dot{\theta} + \frac{\partial \hat{\psi}_R}{\partial \boldsymbol{\nabla}\theta} \cdot \dot{\overline{\boldsymbol{\nabla}\theta}} + \left(\frac{\partial \hat{\psi}_R}{\partial \boldsymbol{\xi}} * \dot{\boldsymbol{\xi}} + \frac{1}{\theta}\boldsymbol{q}_R \cdot \boldsymbol{\nabla}\theta - \boldsymbol{M}^e : \boldsymbol{L}^p + \theta\delta_{\mathrm{R}}\right) = 0. \tag{3.14}$$

Following the Coleman-Noll procedure, one can deduce the following state relations for stress and entropy:

$$\boldsymbol{T}^e = 2\frac{\partial \hat{\psi}_R}{\partial \boldsymbol{C}^e}, \tag{3.15}$$

$$\eta_R = -\frac{\partial \hat{\psi}_R}{\partial \theta}, \tag{3.16}$$

$$\frac{\partial \hat{\psi}_R}{\partial \boldsymbol{\nabla}\theta} = \boldsymbol{0}. \tag{3.17}$$

From equation (3.17), it can be inferred that the free energy and hence the stress, entropy and internal energy are independent of the temperature gradient. In view of the above relations, the second law reduces to the following reduced dissipation inequality:

$$\frac{\partial \hat{\psi}_R}{\partial \boldsymbol{\xi}} * \dot{\boldsymbol{\xi}} + \frac{1}{\theta}\boldsymbol{q}_R \cdot \boldsymbol{\nabla}\theta - \boldsymbol{M^e} : \boldsymbol{L^p} = -\theta\delta_{\mathrm{R}} \leq 0. \tag{3.18}$$

3.1.6 Temperature Evolution Equation

In this section, a partial differential equation that dictates the evolution of temperature during a thermally-coupled mechanical deformation is derived. Consider the time derivative of the internal energy and use the thermodynamic relations derived in equations (3.15) and (3.16):

$$\dot{e}_R = \dot{\psi}_R + \theta\dot{\eta}_R + \dot{\theta}\eta_R = \frac{\boldsymbol{T}^e}{2} : \dot{\boldsymbol{C}}^e - \frac{\theta}{2}\frac{\partial \boldsymbol{T}^e}{\partial \theta} : \dot{\boldsymbol{C}}^e + \left(\frac{\partial \hat{\psi}_R}{\partial \boldsymbol{\xi}} - \theta\frac{\partial^2 \hat{\psi}_R}{\partial \boldsymbol{\xi}\partial\theta}\right) * \dot{\boldsymbol{\xi}} - \theta\frac{\partial^2 \hat{\psi}_R}{\partial \theta^2}\dot{\theta}. \tag{3.19}$$

Substituting $\dot{e}_R$ from the first law (equation (3.10)) and rearranging terms, one obtains

$$-Div\,(\boldsymbol{q}_R) + r_R + \underbrace{\left(\frac{\theta}{2}\frac{\partial \boldsymbol{T}^e}{\partial \theta} : \dot{\boldsymbol{C}}^e\right)}_{\dot{q}_R^e} + \underbrace{\left[\boldsymbol{M}^e : \boldsymbol{L}^p - \left(\frac{\partial \hat{\psi}_R}{\partial \boldsymbol{\xi}} - \theta\frac{\partial^2 \hat{\psi}_R}{\partial \boldsymbol{\xi}\partial\theta}\right) * \dot{\boldsymbol{\xi}}\right]}_{\dot{q}_R^p} = \underbrace{-\theta\frac{\partial^2 \hat{\psi}_R}{\partial \theta^2}\dot{\theta}}_{c_R\dot{\theta}}, \tag{3.20}$$

where $\dot{q}_R^e$ is referential rate of heating due to thermo-elasticity, $\dot{q}_R^p$ represents the referential rate of inelastic heating and c_R is the referential heat capacity, defined at constant strain and constant internal variables. More specifically, c_R is the specific heat capacity c multiplied by the referential mass density ρ_0, i.e., $c_R = \rho_0 c$. Equation (3.20) is the evolution equation for temperature. The first term in the expression for $\dot{q}_R^p$, i.e., $\boldsymbol{M}^e : \boldsymbol{L}^p$, represents the rate of plastic work, while the remainder of $\dot{q}_R^p$ represents the rate of change of internal energy of cold work $\left(\left(\frac{\partial \hat{\psi}_R}{\partial \xi} - \theta\frac{\partial^2 \hat{\psi}_R}{\partial \xi\partial\theta}\right) * \dot{\boldsymbol{\xi}}\right)$ (Rosakis et al., 2000).

Following Rosakis et al. (2000) and Gurtin et al. (2010), the Taylor-Quinney parameter β is defined as follows which quantifies the fraction of plastic power converted to heat:

$$\beta = \frac{\dot{q}_R^p}{\boldsymbol{M}^e : \boldsymbol{L}^p}. \tag{3.21}$$

In general, β is dependent on the evolution of internal variables that describe the density of defects such as dislocations. Experiments on metals by Hodowany et al. (2000) showed that β increases with increasing plastic strain and becomes constant after a saturation is achieved in the dislocation density. However, due to the difficulty of experimentally characterizing β, a constant value is typically assumed in the literature, which is the approach adopted here.

The thermoelastic term in equation (3.20) can be written in a more convenient form using the referential Gruneisen tensor $\boldsymbol{\Gamma}_{\mathrm{R}}$ as follows (Gurtin et al., 2010):

$$\boldsymbol{\Gamma}_{\mathrm{R}} = -\frac{1}{c_R}\left(\frac{\partial \boldsymbol{T}^e}{\partial \theta}\right). \tag{3.22}$$

Substituting equations (3.21) and (3.22) into equation (3.20), one obtains

$$-Div\,(\boldsymbol{q}_R) + r_R - \frac{c_R \theta}{2}\boldsymbol{\Gamma}_{\mathrm{R}} : \dot{\boldsymbol{C}}^e + \beta \boldsymbol{M}^e : \boldsymbol{L}^p = c_R \dot{\theta}. \tag{3.23}$$

3.1.7 Dissipative Constitutive Equations

Assuming plastic irrotationality, we have $\boldsymbol{L}^p = \boldsymbol{D}^p$. Using a co-directional flow rule, the plastic stretch-rate $\boldsymbol{D}^p$ can be written as:

$$\boldsymbol{D}^p = \frac{3}{2}\,\dot{\bar{\epsilon}}^p \frac{\boldsymbol{M}_0^e}{\bar{\sigma}}, \tag{3.24}$$

where $\boldsymbol{M}_0^e$ is the deviatoric portion of Mandel stress, $\dot{\bar{\epsilon}}^p \left(= \sqrt{\frac{2}{3}}|\boldsymbol{D}^p|\right)$ is the effective plastic strain rate and $\bar{\sigma}\left(= \sqrt{\frac{3}{2}}\,|\boldsymbol{M}_0^e|\right)$ is the effective stress. Hence, the rate of plastic work can be simplified as: $\boldsymbol{M}^e : \boldsymbol{L}^p = \boldsymbol{M}^e : \boldsymbol{D}^p = \bar{\sigma}\dot{\bar{\epsilon}}^p$.

Under the assumption of isotropy, the spatial heat flux vector $\boldsymbol{q} = J^{-1}\boldsymbol{F}\boldsymbol{q}_R$ and the spatial temperature gradient $grad\theta = \boldsymbol{F}^{-T}\boldsymbol{\nabla}\theta$ are related through Fourier's Law of Heat Conduction, i.e., $\boldsymbol{q} = -k\,grad\theta$, where k is the thermal conductivity. In order to express the temperature evolution equation (3.23) spatially, the thermoelastic heat generation in the deformed configuration can be expressed through the spatial Gruneisen tensor, as defined below using equation (3.7):

$$\boldsymbol{\Gamma} = \boldsymbol{F}^e \boldsymbol{\Gamma}_{\mathrm{R}} \boldsymbol{F}^{eT} = \boldsymbol{F}^e \left(-\frac{v_0}{c}\frac{\partial \boldsymbol{T}^e}{\partial \theta}\right)\boldsymbol{F}^{eT} = -\frac{J v_0}{c}\frac{\partial\left(J^{-1}\boldsymbol{F}^e \boldsymbol{T}^e \boldsymbol{F}^{eT}\right)}{\partial \theta} = -\frac{v}{c}\left(\frac{\partial \boldsymbol{T}}{\partial \theta}\right). \tag{3.25}$$

where $v_0 = 1/\rho_0$ is the referential specific volume, $v = J v_0$ is the spatial specific volume and $c = v_0 c_R$ is the specific heat capacity at constant strain and constant internal variables with units of J/kg K. Finally, the temperature evolution equation can be written in the spatial form as:

$$div\,(k\,grad\theta) + r \underbrace{-\rho c \theta \boldsymbol{\Gamma} : \boldsymbol{D}^e}_{\dot{q}^e} + \underbrace{\frac{\beta}{J}\bar{\sigma}\dot{\bar{\epsilon}}^p}_{\dot{q}^p} = \rho c \dot{\theta}. \tag{3.26}$$

where $r = J^{-1} r_R$ is the heat supply per unit deformed volume, $\rho = J^{-1}\rho_0$ is the spatial mass density, $\dot{q}^e = J^{-1}\dot{q}_R^e$ is the spatial rate of thermoelastic heating and $\dot{q}^p = J^{-1}\dot{q}_R^p$ is the spatial rate of inelastic heating. The operator div represents the divergence in the deformed configuration. In general, the thermal conductivity is dependent on temperature. However, we neglect the dependence of thermal conductivity on temperature.

3.2 Specialized Constitutive Equations

3.2.1 Free Energy

The constitutive equation for the free energy is taken to depend on the logarithmic elastic strain in the intermediate configuration, which is defined as follows in terms of the right stretch tensor, $\boldsymbol{U}^e$:

$$\boldsymbol{E}^e \equiv ln(\boldsymbol{U}^e). \tag{3.27}$$

The logarithmic strain is used because it facilitates an additive decoupling of the volumetric and deviatoric strains, which is not possible with the Green-Lagrange strain. Furthermore, with the use of an appropriate invariant basis, the consequent

stress terms can also be decomposed into pressure and deviatoric response terms, as demonstrated by Criscione et al. (2000). Such a decomposition is helpful in the direct incorporation of a complete equation of state, which is typically measured through a separate set of experiments. Moreover, elastic constitutive equations using the logarithmic strains typically require fewer higher order parameters to fit experimental data under moderate and high pressures (Clayton, 2014; Poirier and Tarantola, 1998).

The elastic response of sucrose is defined though the free energy per unit reference volume ψ_R. In general, ψ_R is a function of the elastic right Cauchy-Green tensor $\boldsymbol{C}^e$ and temperature θ, but idealizing sucrose as an isotropic material, the free energy can be represented in terms of the three elastic principal stretches ($\psi_R = \tilde{\psi}_R(\lambda_1^e, \lambda_2^e, \lambda_3^e, \theta)$) or the three principal invariants of $\boldsymbol{C}^e$, ($\psi_R = \tilde{\psi}_R(I_1, I_2, I_3, \theta)$) where $I_1 = tr\boldsymbol{C}^e$, $I_2 = \frac{1}{2}\left[(tr\boldsymbol{C}^e)^2 + tr\boldsymbol{C}^{e\,2}\right]$ and $I_3 = \det \boldsymbol{C}^e = J^{e\,2}$. Due to the insufficient experimental information on defects in molecular solids such as sucrose, for simplicity, the dependence of the free energy on internal variables is not considered. With a free energy based on the principal invariants (I_1, I_2, I_3), it is not possible to isolate the effect of each invariant in the consequent constitutive equation for the stress due to the non-orthogonality of different stress response terms, i.e., $\frac{\partial I_i}{\partial \boldsymbol{C}^e} : \frac{\partial I_j}{\partial \boldsymbol{C}^e} \neq 0$ for $i, j = 1,2,3$ and $i \neq j$. Therefore, the free energy density is written in terms of a set of logarithmic strain invariants (K_1, K_2, K_3), as proposed by Criscione et al. (2000). With each of these invariants, one can associate specific aspects of deformation and isolate the effect of each. The first invariant, $K_1 (= tr(\boldsymbol{E}^e) = \ln(J^e))$, represents the volume change, where the superscript 'e' indicates elastic. The second invariant, K_2 $(= |\boldsymbol{E}_0^e|)$, represents the magnitude of the distortional response of the material under constant volume, where subscript '0' indicates the deviatoric part of a tensor. Since $\boldsymbol{E}^e = \frac{K_1}{3}\boldsymbol{I} + \boldsymbol{E}_0^e$, a tensorial direction can be associated with this deviatoric strain invariant: $\boldsymbol{N} = \frac{\partial K_2}{\partial \boldsymbol{E}^e} = \frac{\boldsymbol{E}_0^e}{|\boldsymbol{E}_0^e|}$, where $\boldsymbol{N}$ is a unit tensor. Hence, the strain can be written as $\boldsymbol{E}^e = \frac{K_1}{3}\boldsymbol{I} + K_2\boldsymbol{N}$. The third invariant K_3 $\left(= 3\sqrt{6}\det(\boldsymbol{N})\right)$ represents the mode of distortion. Note that $K_1 > 0$ for dilatation and $K_1 < 0$ under compression. The magnitude of distortion is always positive, $K_2 \geq 0$, whereas K_3 is confined to the range $-1 \leq K_3 \leq 1$. We have that $K_3 = 1$ in simple tension, $K_3 = -1$ in simple compression and $K_3 = 0$ in simple shear.

Let $\tilde{\psi}_R(K_1, K_2, K_3, \theta)$ be the free energy density. It can be shown that, for an isotropic material, the Mandel stress and the logarithmic strain in the intermediate configuration are work conjugates. Hence,

$$\boldsymbol{M}^e = \frac{\partial \tilde{\psi}_R}{\partial \boldsymbol{E}^e} = \left(\frac{\partial \tilde{\psi}_R}{\partial K_1}\frac{\partial K_1}{\partial \boldsymbol{E}^e} + \frac{\partial \tilde{\psi}_R}{\partial K_2}\frac{\partial K_2}{\partial \boldsymbol{E}^e} + \frac{\partial \tilde{\psi}_R}{\partial K_3}\frac{\partial K_3}{\partial \boldsymbol{E}^e}\right) = \left(\frac{\partial \tilde{\psi}_R}{\partial K_1}\boldsymbol{I} + \frac{\partial \tilde{\psi}_R}{\partial K_2}\boldsymbol{N} + \frac{\partial \tilde{\psi}_R}{\partial K_3}\boldsymbol{Y}\right), \tag{3.28}$$

where $\boldsymbol{Y} = 3\sqrt{6}\boldsymbol{N^2} - \sqrt{6}\boldsymbol{I} - 3K_3\boldsymbol{N}$. Since, for an isotropic material, the tensors, $\boldsymbol{C}^e$ and $\boldsymbol{T}^e$ are coaxial, i.e., have the same principal directions, the Cauchy stress can be found using the definition of Mandel stress in equation (3.8):

$$\boldsymbol{T} = \frac{1}{J}\boldsymbol{R}^e\boldsymbol{M}^e\boldsymbol{R}^{e\,T} = \frac{1}{J}\left(\frac{\partial \tilde{\psi}_R}{\partial K_1}\boldsymbol{I} + \frac{\partial \tilde{\psi}_R}{\partial K_2}\boldsymbol{N}' + \frac{\partial \tilde{\psi}_R}{\partial K_3}\boldsymbol{Y}'\right), \tag{3.29}$$

where $\boldsymbol{N}' = \boldsymbol{R}^e\boldsymbol{N}\boldsymbol{R}^{e\,T}$ and $\boldsymbol{Y}' = \boldsymbol{R}^e\boldsymbol{Y}\boldsymbol{R}^{e\,T}$. Note that $\boldsymbol{N}' : \boldsymbol{I} = \boldsymbol{0}, \boldsymbol{Y}' : \boldsymbol{I} = \boldsymbol{0}$ and $\boldsymbol{N}' : \boldsymbol{Y}' = \boldsymbol{0}$, i.e., the Cauchy stress is composed of three mutually orthogonal terms, and each term is dependent on a derivative of a different strain invariant. This is enabled by using the logarithmic strain measure and an appropriate set of invariants for the logarithmic strain. So, it is possible to isolate the three response terms by contracting with $\boldsymbol{I}, \boldsymbol{N}'$ and $\boldsymbol{Y}'$. Specifically, the first term in (3.29) corresponds to the pressure term:

$$\frac{\boldsymbol{T} : \boldsymbol{I}}{3} = -P = \frac{1}{J}\frac{\partial \tilde{\psi}_R}{\partial K_1}, \tag{3.30}$$

while the other two terms sum to give the deviatoric stress. Therefore, the pressure term can be isolated from the deviatoric response, while retaining its dependence on all three invariants and temperature, i.e., $P(K_1, K_2, K_3, \theta)$.

Furthermore, the free energy density, $\tilde{\psi}_R(K_1, K_2, K_3, \theta)$ can, in general, be decomposed additively into three parts: (a) a purely volumetric term, $f_1(K_1, \theta)$, (b) a purely distortional term, $f_2(K_2, K_3, \theta)$ and (c) a coupled volumetric/distortional term, $f_3(K_1, \theta)f_4(K_2, K_3, \theta)$, where the temperature dependence is retained in each portion of the free energy density:

$$\tilde{\psi}_R(K_1, K_2, K_3, \theta) = f_1(K_1, \theta) + f_2(K_2, K_3, \theta) + f_3(K_1, \theta)f_4(K_2, K_3, \theta). \tag{3.31}$$

Such a general form for free energy density has been used by Landauer et al. (2019) to capture the isothermal nonlinear response of elastomeric foams. For the purpose of modeling sucrose, we consider a specific form of equation (3.31) for free energy that neglects the dependence on K_3:

$$\tilde{\psi}_R(K_1, K_2, K_3, \theta) = f_1(K_1, \theta) + G(K_1, \theta)K_2^2, \tag{3.32}$$

where $G(K_1, \theta)$ is the temperature and volumetric strain-dependent shear modulus. The first term in the free-energy expression leads to the pressure through $P(K_1, \theta) = -\frac{1}{J}\frac{\partial f_1}{\partial K_1} - \frac{1}{J}\frac{\partial G}{\partial K_1}K_2^2$. The pressure is found through a complete equation of state as described in Section 3.3. For the range of pressures considered in this investigation, the contribution of the shear-induced pressure $\left(-\frac{1}{J}\frac{\partial G}{\partial K_1}K_2^2\right)$ is much smaller than the first term $\left(-\frac{1}{J}\frac{\partial f_1}{\partial K_1}\right)$ due to small elastic distortional strains (which are limited by the shear strength of the material) and can therefore be neglected for simplicity. The Mandel stress and the Cauchy stress for such a free energy density function can then be calculated as:

$$\boldsymbol{M}^e(K_1, K_2, \theta) = -P(K_1, \theta)J\boldsymbol{I} + 2G(K_1, \theta)K_2\boldsymbol{N}, \tag{3.33}$$

$$\boldsymbol{T}(K_1, K_2, \theta) = -P(K_1, \theta)\boldsymbol{I} + \frac{2}{J}G(K_1, \theta)K_2\boldsymbol{N}'. \tag{3.34}$$

Some of the commonly used functional forms of the shear modulus are further discussed in Section 4.3.3. However, the shear modulus for sucrose has not been experimentally measured as a function of volume and/or temperature. So, in this study, a constant value of the shear modulus is assumed, i.e., $G(K_1, \theta) = G_0$.

3.2.2 Flow Rule

Since $\boldsymbol{L}^p = \boldsymbol{D}^p$ and $\boldsymbol{L}^p = \dot{\boldsymbol{F}}^p\boldsymbol{F}^{p^{-1}}$, the evolution of the plastic distortion $\boldsymbol{F}^p$ is given through the relation: $\dot{\boldsymbol{F}}^p = \boldsymbol{D}^p\boldsymbol{F}^p$. The plastic stretch rate $\boldsymbol{D}^p$ is given through a codirectional flow rule, $\boldsymbol{D}^p = \frac{3}{2}\dot{\bar{\epsilon}}^p\frac{\boldsymbol{M}_0^e}{\bar{\sigma}}$ (equation (3.24)), and the effective plastic strain-rate and the effective stress are related through a strain-rate and temperature-dependent constitutive law. The Johnson-Cook model (Johnson and Cook, 1985) is used here:

$$\bar{\sigma} = [A + B(\bar{\epsilon}^p)^n]\left[1 + C\ln\left(\frac{\dot{\bar{\epsilon}}^p}{\dot{\bar{\epsilon}}_0}\right)\right](1 - \hat{\theta}^m), \tag{3.35}$$

where $\bar{\epsilon}^p(t) = \int_0^t \dot{\bar{\epsilon}}^p(\zeta)d\zeta$ is the accumulated effective plastic strain, $(A, B, n, C, \dot{\bar{\epsilon}}_0, m)$ are material parameters, $\hat{\theta}\left(=\frac{\theta-\theta_{ref}}{\theta_m(P)-\theta_{ref}}\right)$ is a function of temperature θ and pressure P, θ_{ref} is the reference temperature (usually taken to be room temperature) and θ_m is the melt temperature. The parameter A is the yield strength of the material at the reference strain-rate $\dot{\bar{\epsilon}}_0$ and the reference temperature θ_{ref}. The parameters B and n depict the effect of strain-hardening where B is the work hardening modulus and n is the work-hardening exponent. The parameter C is the strain-rate-sentivity coefficient while m is the thermal softening exponent. Since high pressures are applied in our experiments, and temperatures are expected to go beyond melting, the dependence of the melting temperature on pressure is taken into account. Moreover, the melting point of large organic molecules, such as sucrose and HMX is expected to be highly pressure-dependent (Kroonblawd and Austin, 2021; Menikoff and Sewell, 2002). Numerical simulations of the deformation of energetic crystals widely use the Lindemann Law of melting or its linearized version, called the Kraut-Kennedy relation. However, molecular dynamics simulations on HMX (Kroonblawd and Austin, 2021) indicate that the Lindemann Law grossly underestimates the melting point as a function of temperature. An alternative empirical form obtained by Simon and Glatzel (1929) is therefore used:

$$\theta_m = \theta_{m0}\left(1 + \frac{P - P_{ref}}{P_i}\right)^{1/d}, \tag{3.36}$$

where (P_{ref}, P_i, d) are fitting parameters, and θ_{m0} is the melt temperature at the reference pressure P_{ref}. The consequences of the choice for the form of the melt curve are discussed in section 4.3.2.

To obtain a general, complete continuum model, two more issues should be addressed: (a) the phase transition from solid to liquid and (b) a constitutive model for the liquid. One way to model the solid-liquid phase transition is by introducing an order parameter, i.e., a phase-field parameter, as done by Fried and Gurtin (1993). The stress response of the liquid phase can be decomposed into pressure and deviatoric stress components. While the pressure of the liquid can be described through an appropriate equation of state, the deviatoric stress depends on the strain-rate through a pre-factor, called the shear viscosity of the liquid, which is generally a function of pressure and temperature. Both phase transitions and a material model for the liquid phase are not accounted for in the current work but are, however, important for the prediction of chemical reactions in the melt. Since the yield strength of the material model drops rapidly at melt, the

strain-rates tend to increase exponentially and become unreasonably large. In the present framework, the shear strain-rates after melt are set to reach an upper limit beyond which they are assumed to stay constant, as done by Grunschel (2009). This point is discussed in further detail in Section 4. The focus of the present work remains on the solid phase and its constitutive modelling. Next, the development of a complete equation of state for the solid is discussed.

3.3 Complete Equation of State

The Mie-Gruneisen equation of state is a commonly used form of the equation of state for a solid subjected to shock loading. It is often encountered in hydrocodes for solids under pressures of up to a few Megabar. In this section, a derivation of a complete equation of state is presented, i.e., with a temperature dependent specific heat capacity. Note that the equation of state is derived in the deformed configuration as opposed to the intermediate configuration used in the above discussion. We work with the following quantities: (a) the specific free energy $\psi = \psi_R/\rho_0$, (b) the specific entropy $\eta = \eta_R/\rho_0$, (c) the pressure $P = -1/3\ tr(\boldsymbol{T})$, and (d) the spatial specific volume $v = Jv_0 = v_0 \exp(K_1)$, where $v_0 = 1/\rho_0$. Under pure volumetric deformation, the thermoelastic constitutive equations are:

$$\begin{aligned} &\psi = \psi(v,\theta), \\ &\eta = \eta(v,\theta), \\ &P = P(v,\theta), \\ &e = e(v,\theta) = \psi(v,\theta) + \eta(v,\theta)\theta\ . \end{aligned} \tag{3.37}$$

The state relations $\eta_R = -\partial\psi_R/\partial\theta$ and $P = -(1/J)\partial\psi_R/\partial K_1$, which were defined in the intermediate configuration in equations (3.16) and (3.30), respectively, now become

$$\eta = -\frac{\partial\psi}{\partial\theta} \ \ and \ \ P = -\frac{\partial\psi}{\partial v} \tag{3.38}$$

in the deformed configuration, which imply the following Maxwell relation:

$$\frac{\partial\eta}{\partial v} = \frac{\partial P}{\partial\theta}. \tag{3.39}$$

The specific heat at constant volume is defined as:

$$c = \frac{\partial e}{\partial\theta}\,. \tag{3.40}$$

Using the definition of the specific internal energy $e(v,\theta)$ from equation (3.37) and that of the specific entropy from equation (3.38), the above definition of the specific heat at constant volume can be expressed in the following form:

$$c = \theta\frac{\partial\eta}{\partial\theta}. \tag{3.41}$$

The scalar Gruneisen parameter is defined as:

$$\Gamma(v,\theta) = \frac{v}{c}\frac{\partial P}{\partial\theta}. \tag{3.42}$$

Using equation (3.39), an alternate expression for the Gruneisen parameter is as follows:

$$\Gamma(v,\theta) = \frac{v}{c}\frac{\partial\eta}{\partial v}. \tag{3.43}$$

Using equation (3.25), we note that the scalar Gruneisen parameter is simply $\Gamma = \frac{1}{3}tr(\boldsymbol{\Gamma})$.

To determine the state relations in terms of known/measurable thermodynamic quantities, $c(v,\theta)$ and $\Gamma(v,\theta)$, we determine the rate of change of specific entropy and pressure. Applying chain rule and combining the definitions of $c(v,\theta)$ and $\Gamma(v,\theta)$ through equations (3.41), (3.42) and (3.43), we obtain:

$$\begin{aligned} \dot{\eta} &= \left(\frac{\partial\eta}{\partial v}\right)_\theta \dot{v} + \left(\frac{\partial\eta}{\partial\theta}\right)_v \dot{\theta} = \frac{\Gamma c}{v}\,\dot{v} + \frac{c}{\theta}\dot{\theta}, \\ \dot{P} &= \left(\frac{\partial P}{\partial v}\right)_\theta \dot{v} + \left(\frac{\partial P}{\partial\theta}\right)_v \dot{\theta} = \left(\frac{\partial P}{\partial v}\right)_\theta \dot{v} + \frac{\Gamma c}{v}\dot{\theta}. \end{aligned} \tag{3.44}$$

Since state relations do not depend on the thermodynamic path, the rate forms are integrated from an initial state $(v_0,\theta_0,\eta_0,P_0)$ to the final state (v,θ,η,P), along the path shown in Fig. 11, to yield the following relations:

$$\eta(v,\theta) = \eta_0 + \int_{v_0}^{v} \frac{\Gamma(v',\theta_0)c(v',\theta_0)}{v'}dv' + \int_{\theta_0}^{\theta} \frac{c(v,\theta')}{\theta'}d\theta',$$
$$P(v,\theta) = P(v,\theta_0) + \frac{1}{v}\int_{\theta_0}^{\theta} \Gamma(v',\theta_0)c(v',\theta)d\theta', \tag{3.45}$$

where $P(v,\theta_0)$ is the equation of state along an isotherm at a temperature of θ_0, and $P_0 = P(v_0,\theta_0)$. Therefore, to fully specify the state relations, one needs (1) an isotherm at θ_0, i.e., $P(v,\theta_0)$, (2) the Gruneisen parameter, $\Gamma(v,\theta)$, and (3) the specific heat capacity, $c(v,\theta)$.

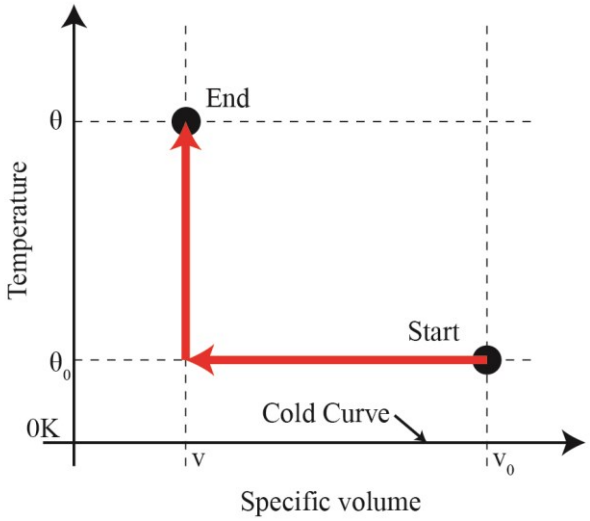

Fig. 11 A thermodynamic path connecting the initial and final states.

To determine the Helmholtz free energy, we apply chain rule:

$$\dot{\psi} = -P(v,\theta)\dot{v} - \eta(v,\theta)\dot{\theta}, \tag{3.46}$$

and integrate to obtain

$$\psi(v,\theta) = \psi_0 - \eta_0(\theta-\theta_0) - \int_{v_0}^{v}\left[P(v',\theta_0) + (\theta-\theta_0)\frac{\Gamma(\mathrm{v}',\theta_0)c(v',\theta_0)}{v'}\right]dv' - \int_{\theta_0}^{\theta}\frac{(\theta-\theta')}{\theta'}c(v,\theta')d\theta', \tag{3.47}$$

where $\psi_0 = \psi(v_0,\theta_0)$. The internal energy can, therefore, be calculated as:

$$e(v,\theta) = \psi(v,\theta) + \eta(v,\theta)\theta = e_0 - \int_{v_0}^{v}\left[P(v',\theta_0) - \theta_0\frac{\Gamma(\mathrm{v}',\theta_0)c(v',\theta_0)}{v'}\right]dv' + \int_{\theta_0}^{\theta}c(v,\theta')d\theta', \tag{3.48}$$

where $e_0 = \psi_0 + \eta_0\theta_0$.

3.3.1 Specialization for a Temperature Independent Gruneisen Parameter

First, note that the Gruneisen parameter Γ and the specific heat c are not independent but related through the following thermodynamic compatibility equation (Menikoff, 2016; Sheffield and Duvall, 1983):

$$\frac{\partial}{\partial v}\left(\frac{\partial^2\psi}{\partial\theta^2}\right) = \frac{\partial}{\partial\theta}\left(\frac{\partial^2\psi}{\partial\theta\partial v}\right). \tag{3.49}$$

Combining equations (3.38) and (3.41), it can be shown that $c = -\theta\left(\frac{\partial^2\psi}{\partial\theta^2}\right)$. Similarly, combining equations, (3.38) and (3.43), one obtains $\Gamma c = -v\frac{\partial^2\psi}{\partial\theta\partial v}$. Therefore, the compatibility relation in equation (3.49) takes the following form:

$$v\frac{\partial c}{\partial v} = \theta\frac{\partial(\Gamma c)}{\partial\theta}. \tag{3.50}$$

Next, we assume that the Gruneisen parameter is a function of specific volume only, $\Gamma = \Gamma(v)$. As mentioned by Grady, (2017), "*Both theoretical arguments and experience suggest that* Γ *is not sensitive to reasonable excursions of internal energy, E for many materials, and is usually assumed to be a volume-dependent only function,* $\Gamma(v)$*.*" For such a class of materials, the compatibility relation in (3.50) can be written as a hyperbolic partial differential equation for c (Menikoff, 2016):

$$v\frac{\partial c}{\partial v} = \theta\Gamma(v)\frac{\partial c}{\partial \theta}. \tag{3.51}$$

The characteristic curves for the PDE are solutions to the ODE:

$$\frac{d\theta}{dv} = -\theta\frac{\Gamma(v)}{v}. \tag{3.52}$$

For a characteristic passing through the initial state (v_0, θ_0), we have:

$$\theta = \theta_0\,\phi(v) \;\text{ with }\; \phi(v) = \exp\left(-\int_{v_0}^{v}\frac{\Gamma(v')}{v'}dv'\right). \tag{3.53}$$

The specific heat capacity is constant along the characteristic curve, i.e., $c(v,\theta) = c(v_0,\theta_0) = c\big(v_0, \theta/\phi(v)\big) = \tilde{c}\big(\theta/\phi(v)\big) = \tilde{c}(\tilde{\theta})$, where the tilde signifies the scaled temperature, $\tilde{\theta} = \theta/\phi(v)$. The function $\tilde{c}$ represents the specific heat capacity as a function of θ along the isochore v_0. Hence, for the class of materials with $\Gamma = \Gamma(v)$, the specific heat is a function of only the scaled temperature. With $\Gamma = \Gamma(v)$ and $c = \tilde{c}(\tilde{\theta})$, the equation of state (3.45) becomes:

$$P(v,\theta) = P(v,\theta_0) + \frac{\Gamma(v)\phi(v)}{v}\int_{\tilde{\theta}_0}^{\tilde{\theta}}\tilde{c}\big(\tilde{\theta}'\big)\,d\tilde{\theta}', \tag{3.54}$$

where $\tilde{\theta}_0 = \theta_0/\phi(v)$. Note that the internal energy in equation (3.48) becomes

$$\begin{aligned} e(v,\theta) &= e(v,\theta_0) + \phi(v)\int_{\tilde{\theta}_0}^{\tilde{\theta}}\tilde{c}\big(\tilde{\theta}'\big)d\tilde{\theta}', \\ \text{with }\; e(v,\theta_0) &= e_0 - \int_{v_0}^{v}\left[P(v',\theta_0) - \theta_0\frac{\Gamma(\mathrm{v}')\tilde{c}\big(\tilde{\theta}_0\big)}{v'}\right]dv', \end{aligned} \tag{3.55}$$

so that

$$P(v,\theta) = P(v,\theta_0) + \frac{\Gamma(v)}{v}\left[e(v,\theta) - e(v,\theta_0)\right], \tag{3.56}$$

which is a common form of the Mie-Gruneisen equation of state. The forms of P and e in equations (3.54) and (3.55) respectively and the resulting Mie-Gruneisen equation of state in equation (3.56) are a direct result of the assumption that the Gruneisen parameter is a function of specific volume only. Also, note that the state relations for P, e, ψ and η are often written with $\theta_0 = 0K$ as the reference temperature as simplified forms for each of these quantities emerge with the cold curve as the reference isotherm. However, we choose to write the state relations with ambient conditions as the reference state due to the relative ease of obtaining material properties at the ambient temperature.

3.4 Thermoelastic Heating

Heating due to large elastic deformation is important in applications where a material is subject to impact and shocks. Large pressures of the order of several GPa can be generated under such loading conditions in a very short amount of time, typically tens of nanoseconds. Therefore, adiabatic conditions combined with large volumetric compression can result in a significant temperature increase. Such an increase is especially important in the case of energetic materials whose mechanical and chemical behavior is highly temperature sensitive. Moreover, the melting points of energetic materials and their simulants are relatively low, compared to metals, which means that not a lot of thermal heating is required to melt. Therefore, it is important to accurately predict the temperature of such materials under dynamic loads. In the PSPI experiments, normal compression can significantly raise the temperature and affect the strength of the material under subsequent shear loading. So, it is important to quantify the thermo-elastic heating.

In section 3.1.7, it was shown that the rate of heat generation due to elastic processes is given as: $\dot{q}^e = -\rho c\theta\boldsymbol{\Gamma}\colon\boldsymbol{D}^e$ (equation (3.26)). Since, we neglect the temperature dependence of the shear modulus, i.e., $\frac{\partial G}{\partial\theta} = 0$, the Gruneisen tensor is spherical, i.e., $\boldsymbol{\Gamma} = \Gamma(v)\boldsymbol{I}$, so that

$$\dot{q}^e = -\rho c\theta\Gamma(v)\, tr(\boldsymbol{D}^e) = -\rho c\theta\Gamma(v)\,\frac{\dot{J^e}}{J^e} = -\rho c\theta\Gamma(v)\dot{K_1}. \tag{3.57}$$

For dynamic compression of materials, one typically encounters isentropic or shock loading. So, it is worthwhile investigating these thermodynamic processes in detail, along with the case of isothermal loading serving as a reference. Plotting these curves for sucrose is expected to provide insights into material behavior under different types of loading. In the following sections, analytical expressions for different state variables are derived for a solid undergoing isothermal, isentropic or shock loading (Hugoniot), using the complete equation of state developed above. Special attention is paid to the temperature increase expected for the three cases. In this investigation, temperature is not measured independently. However, if an accurate method for temperature measurement were to be developed in the future, the equations developed below would allow one to directly extract material parameters for the complete Mie-Gruneisen equation of state.

3.5 Isentrope

Normal loading under pressure-shear plate impact can be considered as being close to following an isentrope, i.e., the PSPI experiments load the specimen quasi-isentropically. Since the temperature change during normal loading that precedes the shear loading in a PSPI experiment influences the shear strength of the material, it is necessary to calculate the temperature change during isentropic loading. Using the expression for $\dot{\eta} = 0$ in equation (3.44), the Gruneisen parameter can be expressed as:

$$\Gamma = -\frac{v}{\theta}\left(\frac{\partial\theta}{\partial v}\right)_{\eta}. \tag{3.58}$$

Integrating the above relation gives the temperature variation along an isentrope as a function of specific volume:

$$\theta^{(\eta)}(v) = \theta_0 \exp\left(-\int_{v_0}^{v}\frac{\Gamma(v')}{v'}dv'\right) = \theta_0\phi(v). \tag{3.59}$$

Since equation (3.59) represents a characteristic curve for the hyperbolic PDE in equation (3.51), it follows that the specific heat c is constant along any isentrope. This is a consequence of the assumption that Gruneisen parameter is a function of specific volume only.

Pressure along an isentrope can be found by substituting the temperature along the isentrope from equation (3.59) into equation (3.54), which results in the following form:

$$P^{(\eta)}(v) = P(v,\theta_0) + \frac{\Gamma(v)\phi(v)}{v}\int_{\tilde{\theta}_0}^{\tilde{\theta}^{(\eta)}}\tilde{c}\left(\tilde{\theta}'\right)d\tilde{\theta}', \tag{3.60}$$

where $\tilde{\theta}^{(\eta)} = \frac{\theta^{(\eta)}}{\phi(v)} = \theta_0$.

3.6 Isotherm

Pressure along an isotherm can be obtained from equation (3.54) by substituting the isotherm temperature $\theta = \theta_i$:

$$P(v,\theta_i) = P(v,\theta_0) + \frac{\Gamma(v)\phi(v)}{v}\int_{\tilde{\theta}_0}^{\tilde{\theta}_i}\tilde{c}\left(\tilde{\theta}'\right)d\tilde{\theta}'. \tag{3.61}$$

where $\tilde{\theta}_i = \theta_i/\phi(v)$. In this work, the 3rd order logarithmic equation of state (Poirier and Tarantola, 1998), expressed below, is chosen as the reference isotherm:

$$P = K_{\theta 0}\left(\frac{v_0}{v}\right)\ln\left(\frac{v_0}{v}\right)\left[1 + \frac{K'_{\theta 0} - 2}{2}\ln\left(\frac{v_0}{v}\right)\right], \tag{3.62}$$

where $K_{\theta 0}$ and $K'_{\theta 0}$ are elastic bulk modulus and the first derivative of elastic bulk modulus with respect to pressure, respectively, at ambient temperature and specific volume. A derivation of equation (3.62) is presented in Appendix A. Fig. 12 shows isotherms for sucrose at different temperatures, using the material parameters for sucrose in Table 2.

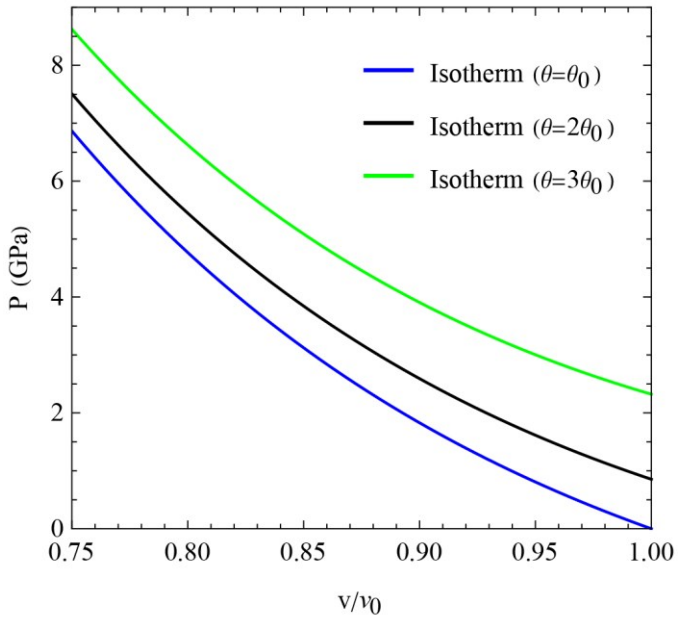

Fig. 12 Isotherms for sucrose at different temperatures. $\theta_0 = 298\,K$. As temperature increases, the isotherms translate upward

3.7 Hugoniot

A problem of interest is the ability to predict detonation in energetic material aggregates when subjected to a shock wave loading. Consider the case of a shock wave traveling through a solid that subjects the material to a high pressure. Under such high pressures, the shear strength of the solid is negligible with respect to the pressure applied. So, the normal stress jump across the shock wave can be approximated by the pressure jump. Then, the specific internal energy of the solid for shock compression from an initial state of $(e_0, P_0, \theta_0, v_0)$ is given through the following Rankine-Hugoniot relation:

$$e^{(H)}(v) = e_0 + \frac{1}{2}\left(P^{(H)}(v) + P_0\right)(v_0 - v). \tag{3.63}$$

Pressure along a Hugoniot requires another piece of information. Often, that is provided in terms of a shock speed-particle speed relation. Another way to find the pressure on a Hugoniot is by using a reference curve and then substituting it into the complete equation of state, which is represented in the present case using the Mie-Gruneisen form of the equation of state (3.56):

$$P^{(H)}(v) - P(v, \theta_0) = \frac{\Gamma(v)}{v}\left[e^{(H)}(v) - e(v, \theta_0)\right]. \tag{3.64}$$

Substituting the expressions for internal energy from equations (3.63) and (3.55) into equation (3.64), pressure along a Hugoniot can be written as:

$$P^{(H)}(v) = \frac{\frac{\Gamma(v)}{2v}P_0(v_0 - v) + P(v, \theta_0) + \frac{\Gamma(v)}{v}\left\{\int_{v_0}^{v}\left[P(v', \theta_0) - \theta_0\frac{\Gamma(\mathrm{v}')\tilde{c}\left(\widetilde{\theta_0}\right)}{v'}\right]dv'\right\}}{1 - \frac{\Gamma(v)}{2v}(v_0 - v)}. \tag{3.65}$$

Now consider the definition of internal energy from equation (3.37), i.e., $e(v, \theta) = \psi(v, \theta) + \eta(v, \theta)\theta$. The rate of change of internal energy can be expressed as:

$$\dot{e} = \dot{\psi} + \dot{\eta}\theta + \theta\dot{\eta} = \left[\left(\frac{\partial\psi}{\partial v}\right)_\theta \dot{v} + \left(\frac{\partial\psi}{\partial\theta}\right)_v \dot{\theta}\right] + \dot{\eta}\theta + \theta\dot{\eta}. \tag{3.66}$$

Since $\left(\frac{\partial\psi}{\partial v}\right)_\theta = -P$ and $\left(\frac{\partial\psi}{\partial\theta}\right)_v = -\eta$ (from equation (3.38)), equation (3.66) reduces to the rate form of the first law of Thermodynamics for a reversible process involving volumetric deformations only, i.e.,

$$\dot{e} = -P\dot{v} + \theta\dot{\eta}. \tag{3.67}$$

Substituting the rate of change of entropy from equation (3.44), the rate of change of internal energy can be written as follows:

$$\dot{e} = \left(-P + \frac{\Gamma c\theta}{v}\right)\dot{v} + c\dot{\theta}. \tag{3.68}$$

Equating the rate of change of internal energy obtained from equations (3.63) and (3.68), a first-order ODE in $\theta^{(H)}$ is obtained:

$$c\frac{d\theta^{(H)}}{dv} + \frac{\Gamma c}{v}\,\theta^{(H)} = \underbrace{\frac{1}{2}(v_0 - v)\frac{dP^{(H)}(v)}{dv} + \frac{1}{2}\left(P^{(H)}(v) - P_0\right)}_{h(v)}. \tag{3.69}$$

The right-hand side of equation (3.69) is a function of specific volume and can be abbreviated as $h(v)$, and $P^{(H)}$ can be substituted from equation (3.65). Substituting the derivative of the scaled temperature, $\tilde{\theta} = \theta/\phi(v)$, with respect to v, i.e., $\phi(v)\frac{d\tilde{\theta}}{dv} = \frac{d\theta}{dv} + \frac{\Gamma(v)}{v}\theta$, into equation (3.69), a simpler expression for the ODE governing the temperature along a Hugoniot is obtained:

$$\tilde{c}\left(\tilde{\theta}^{(H)}\right)\frac{d\tilde{\theta}^{(H)}}{dv} = \frac{h(v)}{\phi(v)}. \tag{3.70}$$

In its most generic form, the temperature relation above is a non-linear ODE and needs to be solved numerically. The special case of a constant specific heat can be solved by straightforward integration.

3.8 Comparison of the Three Thermodynamic Processes

At this point, it is instructive to compare the pressure-volume-temperature (P, v, θ) response under the different types of loading considered above. Fig. 13 shows a three-dimensional surface of a specialized complete Mie-Gruneisen equation of state for sucrose in the (P, v, θ) space. It is assumed that $\frac{\Gamma(v)}{v} = \frac{\Gamma_0}{v_0}$ where $\Gamma_0 = \Gamma(v_0)$. The material properties of sucrose used for plotting the curves are given in Table 2. The table includes an expression for the temperature-dependent specific heat and an approximation of its integral, which are discussed further in Appendix B. An isotherm, an isentrope and a Hugoniot are plotted simultaneously in Fig. 13. It is evident that there is a substantial difference between the three curves along the temperature axis.

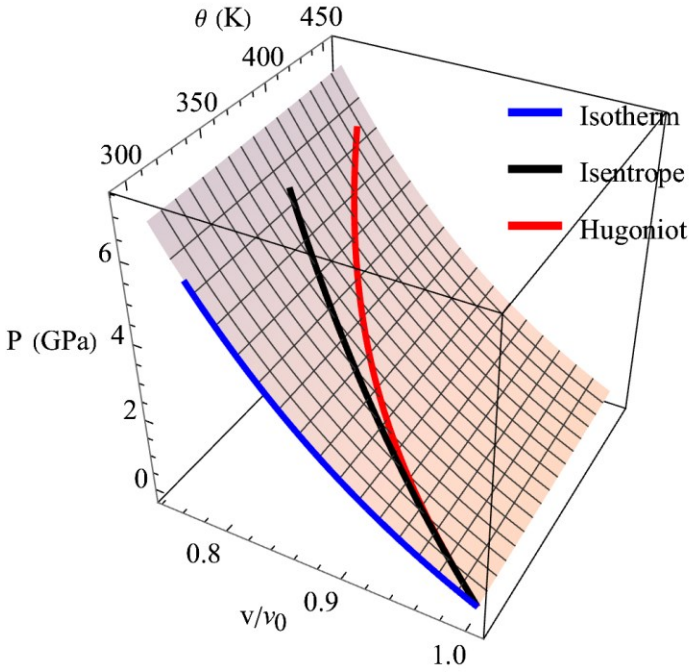

Fig. 13 Pressure-Volume-Temperature curve for a complete Mie-Gruneisen equation of state for sucrose (Orange grid). Blue: Isotherm, Black: Isentrope and Red: Hugoniot, all passing through the initial state, $P_0 = 0, v_0, \theta_0 = 298K$.

Table 2 Thermoelastic material parameters for sucrose used in plotting calculated profiles of the Isentrope, Isotherm and Hugoniot.

ρ_0	Initial density	1580.5 kg/m^3
Elastic Parameters		
G_0	Shear Modulus at ambient	8.58 GPa
$K_{\theta 0}$	Isothermal bulk modulus at ambient	14.3 GPa
$K'_{\theta 0}$	Derivative of Bulk modulus with respect to pressure	3.75
Γ_0	Gruneisen parameter at ambient	1.09
Thermal parameters		
c_0	Specific heat capacity at constant v, $c_v(\theta) = \dfrac{\theta^3}{c_0 + c_1\theta + c_2\theta^2 + c_3\theta^3}$	7.095 x 10^3 kgK^4/J
c_1		2.230 x 10^1 kgK^3/J
c_2		4.180 x 10^{-3} kgK^2/J
c_3		3.050 x 10^{-4} kgK/J
a_1	$\int_0^\theta c_v(\theta')d\theta' \approx (a_1\theta + a_2\theta^2 + a_3\theta^3)\dfrac{J}{kg}$	-105.517 J/kgK
a_2		2.473 J/kgK^2
a_3		-6.067×10^{-4} J/kgK^3

For a more illustrative comparison, the thermodynamic curves are compared in two-dimensional plots. Fig. 14 (a) shows that for the pressure P vs compression ratio, v/v_0, the Hugoniot lies at the top and the isotherm lies at the bottom of the three curves. However, for the volume compression ratios considered here, the difference between the curves is relatively modest. The main difference between the isotherm, the isentrope and the Hugoniot lies in the temperature increase of the material. While the temperature rise along an isentrope is almost linear with volume compression ratio (Fig. 14 (b)), the temperature along the Hugoniot quickly diverges from the isentrope and leads to a much higher temperature rise. These differences in the material response to different types of thermodynamic loading has significant consequences for energetic materials. For example, a ramp wave with an isentropic pressure loading is much less likely to cause ignition as compared to a shock wave of the same pressure magnitude.

From the preceding discussion, it is worth highlighting the importance of using a complete equation of state with a temperature dependent specific heat. As noted by Menikoff and Sewell (2002) and Sewell and Menikoff (2004), incorporating the temperature dependence of the specific heat in an equation of state is extremely important to accurately predict hot-spot temperatures and hence the consequent chemical reaction kinetics. Let us compare the thermodynamic response of sucrose for two cases: (a) a temperature dependent specific heat, and (b) a constant specific heat capacity, evaluated at $\theta = \theta_0$. Fig. 15 (a) shows the difference arising in the temperature response due to the form of specific heat chosen. As expected, the temperature along the isentrope should be unaffected by the choice of specific heat capacity because it remains constant along an isentrope. However, there is a substantial difference in the temperature rise along a Hugoniot. Using the temperature-dependent specific heat $c(\theta)$ results in a lower temperature increase with compression as compared to using a constant specific heat $c(\theta_0)$ with the difference between the two cases increasing as the amount of compression increases. Such a comparison emphasizes the role played by the choice of specific heat capacity for shock wave loading of energetic/simulant crystals. Thus, proper representation of the temperature dependence of specific heat has consequences for accurately simulating the mechanical, thermal and chemical response of energetic materials. In particular, the choice of specific heat can have a potentially significant impact on the accuracy of predicting deformation localization and formation of hot-spots due to adiabatic shear bands and the likelihood of such hot-spots turning critical, leading to ignition. Fig. 15 (b) shows that the choice of a temperature dependent specific heat has a small effect on the pressure-volume response of sucrose.

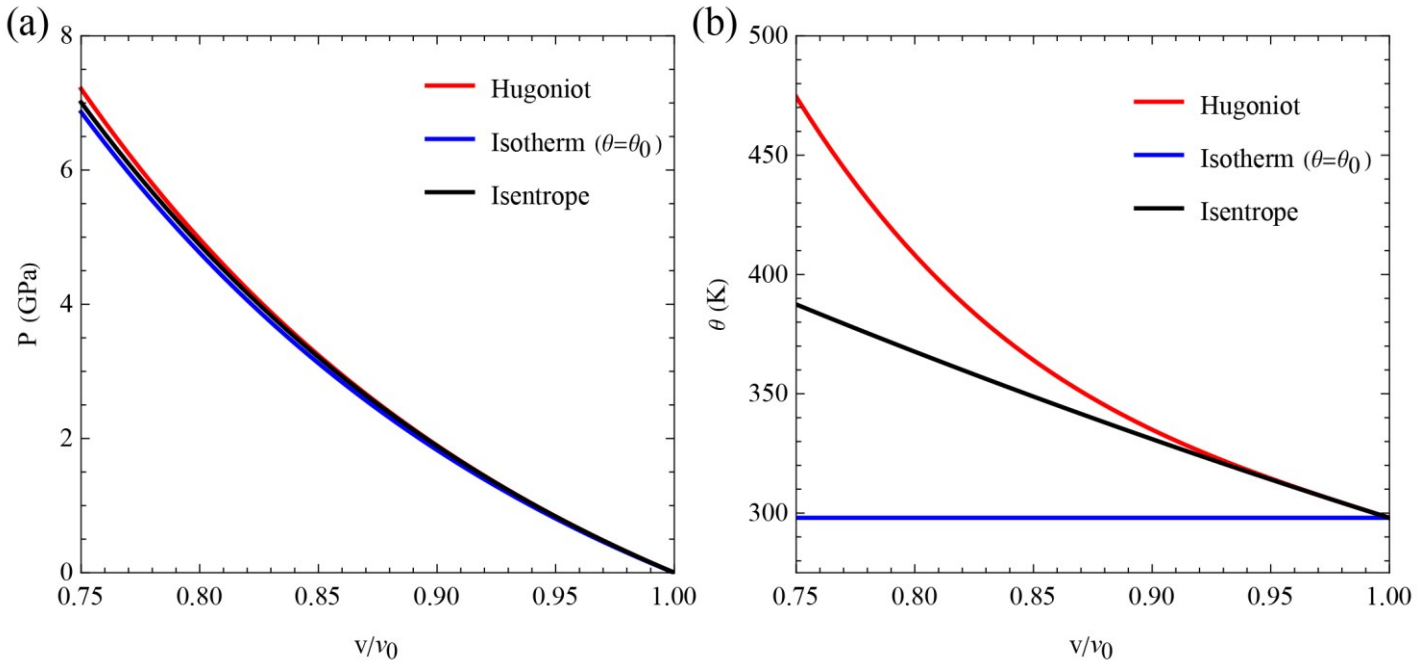

Fig. 14 (a) Pressure P vs compression ratio v/v_0, and (b) temperature θ vs compression ratio v/v_0, plots for sucrose for a Hugoniot, an isotherm (at $\theta = \theta_0$) and an isentrope, all passing through the same initial point, i.e., $P_0 = 0, \frac{v}{v_0} = 1, \theta_0 = 298\ K$.

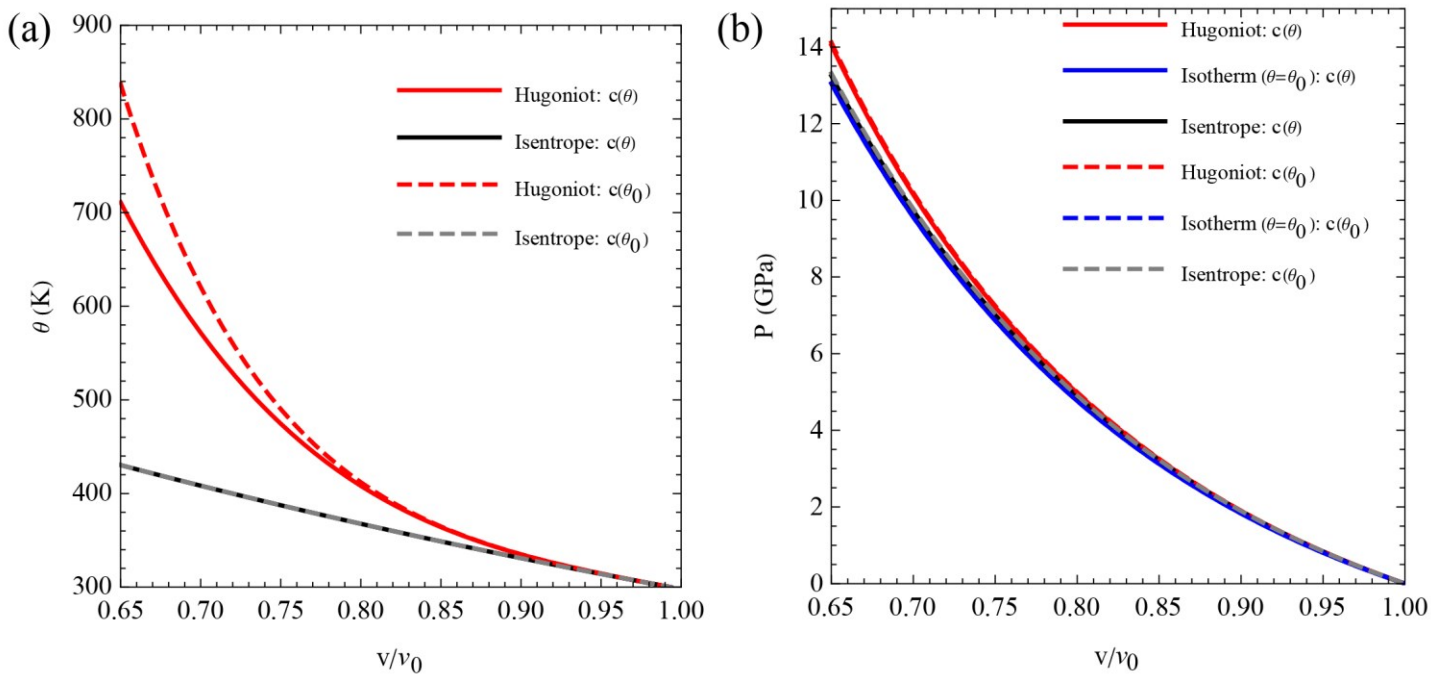

Fig. 15 Effect of the choice of specific heat on thermodynamic curves for sucrose, i.e., the Hugoniot, isotherm and isentrope. Curves are plotted for two cases: (1) a temperature-dependent specific heat capacity (solid lines) and (2) a temperature-independent specific heat capacity evaluated at $\theta = \theta_0$ (dashed lines).

3.9 Summary of the Constitutive Model

In this section, a thermodynamic framework is presented for thermo-mechanical constitutive modeling of sucrose. An energy balance equation accounting for the thermoelastic and the dissipative work is derived (3.23). The free energy is written in terms of invariants of a logarithmic strain measure (3.32), such that it allows an additive

decomposition of the Cauchy stress into pressure and deviatoric stresses (3.34). The constitutive relation for pressure, with dependence on both volume and temperature, is derived in terms of a complete Mie-Gruneisen equation of state (3.54) while the thermo-viscoplastic deformation is modeled through a pressure-dependent Johnson-Cook Model (3.35). Using the complete equation of state, the deformation behavior of sucrose is compared under isentropic, isothermal and shock loadings. The material constants for thermo-elasticity are presented in Table 2 while those for thermo-viscoplasticity are presented in Table 3. In the next section, numerical simulations are carried out using this thermally-coupled mechanical constitutive model and compared with PSPI experimental observations.

4 Numerical Simulations

The constitutive model for sucrose described in Section 3 has been implemented in the commercial finite element software Abaqus/Explicit, using a user material subroutine VUMAT. This section details the results of numerical simulations of PSPI loading and draws comparisons with experimental observations. The VUMAT algorithm is laid out in detail in Appendix C.

The flyer, target plates and the sandwiched specimen are modeled using four-noded bilinear plane strain quadrilateral elements with reduced integration, hourglass control and thermal coupling (CPE4RT). Since shear localization is expected, the mesh size of the specimen is kept smaller than the expected shear band width. Without prior knowledge of the expected temperature rise and shear strain-rates within the band, the shear band width is estimated as:

$$\delta_{band} \approx 2\sqrt{Dt}, \tag{4.1}$$

where $D = k/\rho_0 c(\theta)$ is the thermal diffusivity and t is the expected duration of loading. Using the material constants listed in Table 2 and Table 3 and the temperature-dependence of the specific heat discussed in Appendix B, the thermal diffusivity of sucrose can be calculated to vary between $94 \times 10^{-9}\ m^2/s$ and $258 \times 10^{-9}\ m^2/s$ (for specific heats at ambient and the Dulong-Petit limit), and for a loading duration of about $1\ \mu s$, the shear band width is expected to lie between $0.61\ \mu m$ and $1\ \mu m$. Therefore, a mesh size of $0.25\ \mu m$, which is sufficiently smaller than the minimum expected band width, is chosen to err on the side of caution (see Fig. 16). For the stability of the numerical scheme, the time-step is dictated by the longitudinal wave speed in sucrose and the time-scale of thermal diffusion.

$$\Delta t < \min\left(\frac{\Delta x}{c_L}, \frac{(\Delta x)^2}{2D}\right), \tag{4.2}$$

where $c_L = \sqrt{(K_{\theta 0} + (4/3)G_0)/\rho_0}$ is the longitudinal wave speed at ambient and Δx is the mesh size. For a mesh size of $0.25\ \mu m$, a time-step of $10^{-11} s$ satisfies the stability criteria in equation (4.2) with a sufficient margin for error. Simulations are carried out using a dynamic, temperature-displacement, explicit analysis step. Full thermo-mechanical coupling is modeled, including heat conduction even though its effects are negligible, as demonstrated below.

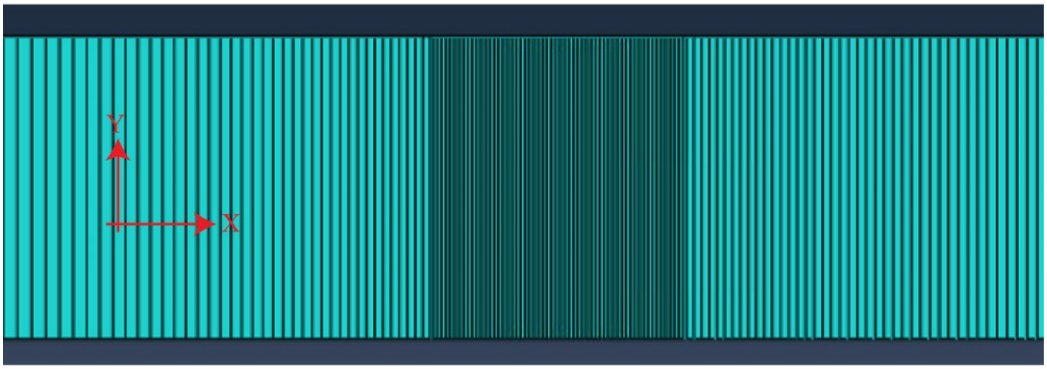

Fig. 16 Finite-element mesh for simulation of Shot3. The sucrose specimen (middle of the figure) has a finer mesh size of 0.25 μm than the target plates on either side which have a mesh size increasing linearly from 0.5 μm (at the target/specimen interface) to 50 μm (at the other ends).

4.1 Comparisons of stress profiles

Experimental and simulated velocity profiles at the sample/rear target plate interface are converted to nominal normal and shear stresses using equation (2.1) and compared. The material constants used in simulations are shown in Table 2

and Table 3. The choice of material constants is discussed and justified in Appendix B. While some of the material constants have been obtained from literature, others have been fit to the PSPI experimental data. In particular, the material parameters for the Johnson-Cook model are based on a modest search of parameter values. All parameters shown in Table 2 (i.e., the thermoelastic parameters) are adopted from the literature (as discussed further in Appendix B). Parameters for the Johnson-Cook model shown in Table 3 are obtained by fitting the simulation results with the experimental results. It has been observed that the agreement between simulations and experiments is most sensitive to the strain-rate sensitivity coefficient C, the work-hardening exponent n, and the thermal softening exponent *m* in the Johnson-Cook model. The remaining parameters in Table 3 are taken from literature (see Appendix B).

Fig. 17 shows experimental and simulated normal stress profiles for low and high-pressure shots. Since the compaction of the initial surface roughness of the sucrose specimen is not modeled in the simulations, the initial step observed in the normal stress profiles in the experiments is not seen in the simulations. The rise of normal stress to the plateau agrees very well with the experiments. For the high-pressure shots, a slight deviation from the simulated profiles is observed for normal velocities above 0.12 mm/μs, due to loading of the anvil WC plates beyond their Hugoniot Elastic Limit. Simulated shear stress profiles are compared with experimental observations in Fig. 18. It is shown that the choice of a single set of material constants can fit the shear stresses under different experimental conditions reasonably well. Simulated profiles can capture the drop in the shearing resistance of sucrose, which results when thermal softening overtakes hardening due to increasing strains and strain-rates. The rising portion of simulated nominal shear stress is steeper than that observed in the experiments which indicates that the actual shear modulus value upon the arrival of shear wave is smaller than the quasi-static shear modulus value used here. As discussed in section 3.2, the shear modulus varies with temperature and pressure and such a variation, if experimentally validated, can be readily incorporated into the simulation capability. However, due to the lack of experimental data on the variation of shear modulus with temperature and pressure, a constant value is employed. Good agreement between the experiments and the simulations is seen for the peak values of nominal shear stresses, especially for the cases of low pressures. Due to small variations in the experimentally observed shear behavior under similar sets of conditions, simulated shear stress profiles fit some shots better than the others. The drop in shear strength is also captured well in the numerical simulations. Simulated profiles for the low-pressure experiments show a slightly delayed drop.

Table 3 Visco-plastic and thermal material constants for sucrose used in simulating stress profiles for PSPI experiments.[1]

Johnson-Cook parameters		
A	Static yield strength	500 MPa
B	Strain-hardening coefficient	500 MPa
n	Strain-hardening exponent	0.1
C	Strain-rate hardening coefficient	0.01
$\dot{\epsilon}_0$	Reference plastic strain-rate	1 s^{-1}
m	Thermal softening exponent	0.45
θ_{ref}	Reference temperature	298 K
θ_{m0}	Melt temperature at ambient pressure	459 K
$\dot{\epsilon}^p_{lim}$	Limiting strain-rate	10^7 s^{-1}
Thermal parameters		
k	Thermal conductivity	0.486 W/mK
β	Inelastic heat fraction	0.9
P_{ref}	Reference pressure in Simon-Glatzel melt relation	0
P_i	Parameter in Simon-Glatzel melt relation	0.3 GPa
d	Parameter in Simon-Glatzel melt relation	3.25

[1]Anvil materials are modeled as thermoelastic with the following material constants: (a) D2 Steel ($E = 210\ GPa, \nu = 0.29, \rho_0 = 7787 \frac{kg}{m^3}, k = 20 \frac{W}{mK}, c = 461 J/kgK$), and (b) WC ($E = 650\ GPa, \nu = 0.2, \rho_0 = 15400 \frac{kg}{m^3}, k = 100 \frac{W}{mK}, c = 209.3 J/kgK$), where E is the Young's modulus and ν is the Poisson's ratio.

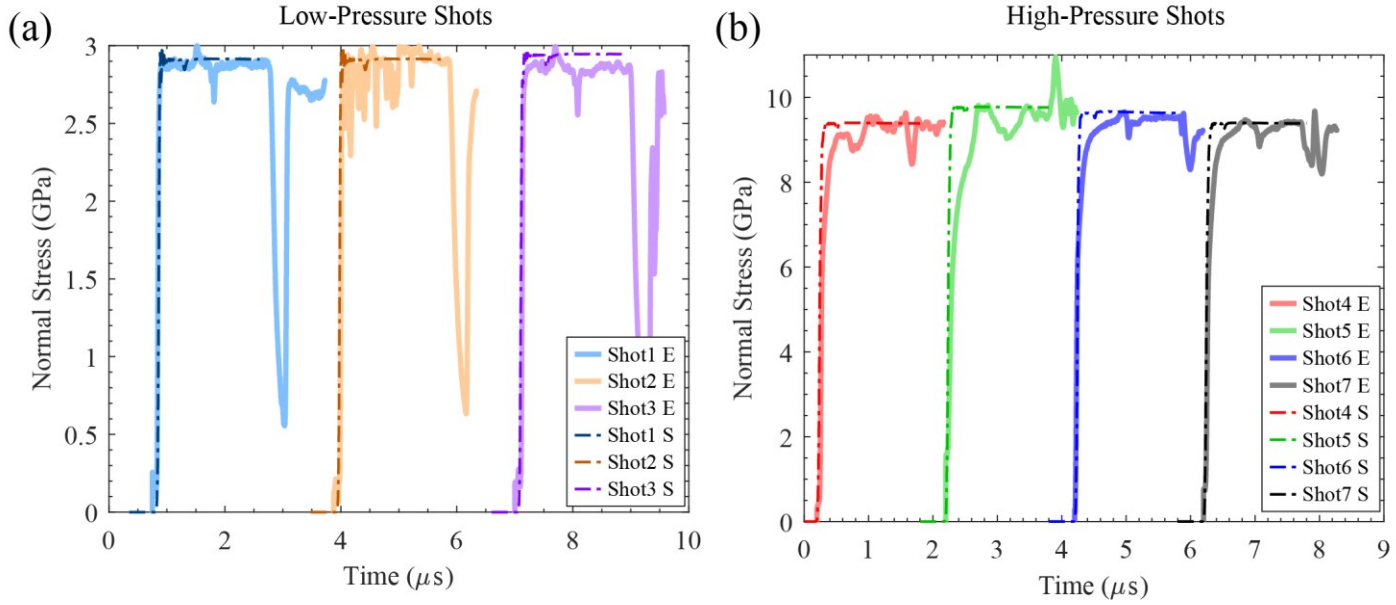

Fig. 17 Nominal normal stress profiles for (a) low-pressure and (b) high-pressure PSPI shots on sucrose. Experimental profiles (indicated by the suffix 'E' in the legend) are shown using solid lines, while the corresponding simulated profiles (indicated by the suffix 'S' in the legend) are represented using dashed lines.

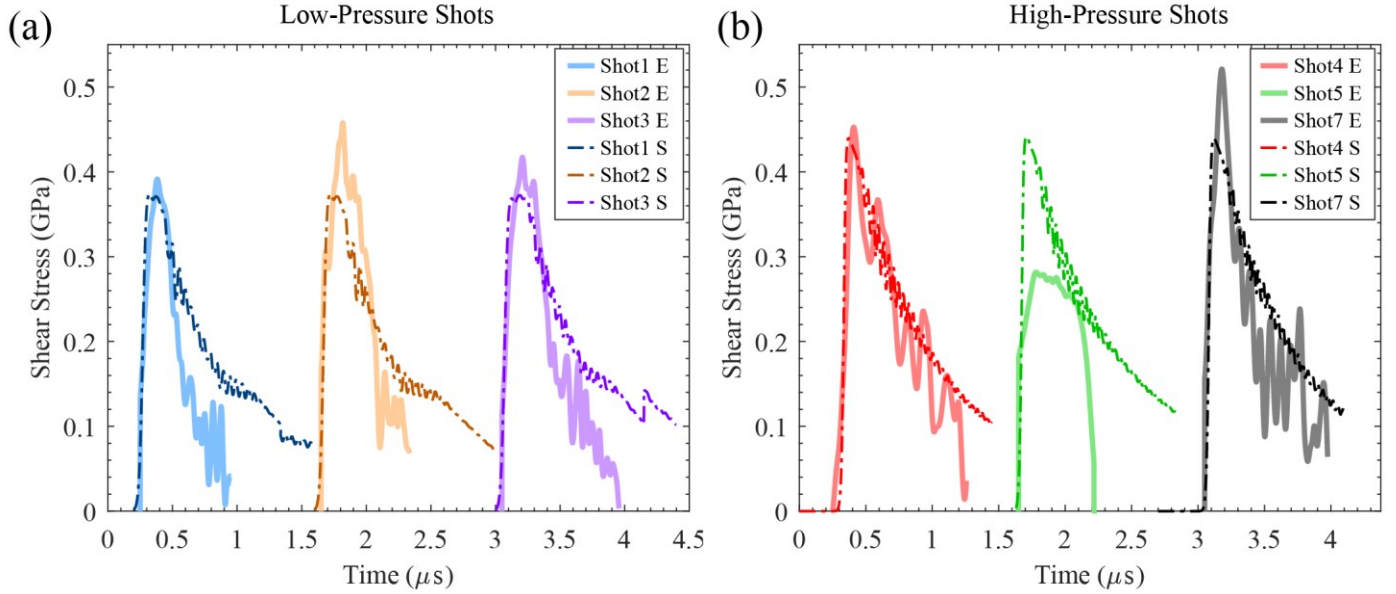

Fig. 18 Nominal shear stress profiles for (a) low-pressure and (b) high-pressure PSPI shots on sucrose. Experimental profiles (indicated by the suffix 'E' in the legend) are shown using solid lines, while the corresponding simulated profiles (indicated by the suffix 'S' in the legend) are represented using dashed lines.

4.2 Adiabatic Shear Localization

A drop in the shear strength of sucrose as seen in both experiments and simulations is indicative of the development of localized deformation in the form of adiabatic shear bands. Temperature profiles across the specimen for low and high-pressure cases each are plotted in Fig. 19. Shot3 and Shot4 are chosen as representative low and high-pressure shots, respectively. As each specimen is compressed by the normal wave, the temperature of the specimen rises uniformly due to elastic and plastic work; the contribution of each to the temperature rise is discussed further in section 4.3.1. There is a small drop in temperature at each specimen/anvil interface due to heat conduction into the bounding anvil plates. However, the temperature drop at the interfaces is sufficiently small that thermal conduction effects are practically negligible, and the temperature increase in the specimen can be assumed to be the result of a nearly adiabatic process.

After the arrival of the shear wave, adiabatic shear localization is observed in both the low and high-pressure cases. A shear band of ~3.7 μm width forms for the low-pressure case while two shear bands of widths ~3.8 μm and ~2.8 μm form for the high-pressure case, as shown in Fig. 19 (a) and (b) respectively.

For the low-pressure case, the shear wave arrives at the left specimen interface at 0.86 μs (assuming impact takes place at time t = 0 μs) and shear localization begins at ~1.13 μs. Shear localization is characterized by a sudden and steep increase in temperature and a drop in shear stress, as shown for a material point in the middle of the shear band in Fig. 20 (a). Normal and shear stress profiles for the material point are also plotted to provide a perspective on the timeline of events. It is observed that the temperature increases initially to 363 K following the arrival of the normal wave. When the normal stress has plateaued, the temperature remains constant. After the shear wave arrives, there is a uniform increase in temperature initially throughout the thickness of the specimen, followed by a rapid rise in the middle of the band once localization begins. Temperatures as high as 1155 K are predicted at t = 2 μs.

For the high-pressure case, as shown in Fig. 19 (b), two shear bands form, with the second one (on the right) initiating within a few nanoseconds of the first. The peak temperature in each band at t = 2 μs is about 1600 K and 1325 K respectively. The difference in the times of initiation of the two shear bands is of the order of the time it takes for the longitudinal wave to travel the specimen thickness. Thus, the second shear band (on the right) initiates before the effect of the formation of the first shear band (on the left) is felt at its location. Such an observation is similar to the formation of multiple necks in rapidly expanding cylindrical metal rings as observed by Grady and Benson (1983) and Altynova et al. (1996) and theoretically analyzed by Guduru and Freund (2002). The number of necks were found to increase at higher strain-rates which is similar to the observation of multiple shear bands for Shot 4. Stress and temperature profiles are plotted in Fig. 20 (b) for the material point in the middle of the left shear band. Normal compression increases the temperature substantially to a value of 492 K compared to 363 K for the low-pressure shot. A larger increase is expected with increasing pressure due to an increase in both thermo-elastic work and thermo-viscoplastic work. It is also observed that the time duration between the arrival of shear wave and the formation of a shear band is only 0.1 μs compared to 0.27 μs for the low-pressure case. Therefore, localization is expected to begin earlier in time in the higher pressure shots. Fig. 20 shows that the steep increase in temperature coincides with the drop in shear stress for both cases considered.

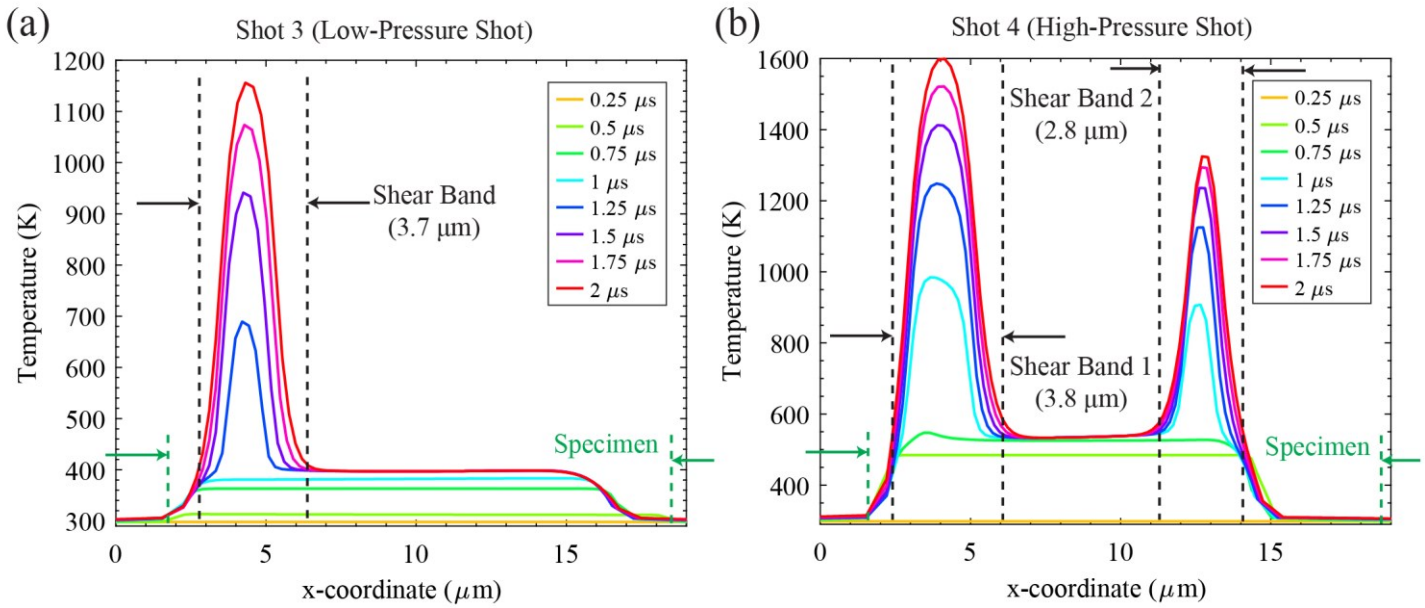

Fig. 19 Through thickness temperature variation for (a) Shot3 (low-pressure shot) and (b) Shot4 (high-pressure shot) plotted as a function of the deformed x-coordinate. The span of the specimen in the undeformed configuration is indicated by green arrows. The left most point, i.e., x=0 is kept fixed in time while plotting the temperature profiles. Small portions of the target plates on either side are also plotted to demonstrate that minimal heat conduction takes place at the specimen/anvil interfaces during the time duration considered. Temperatures are plotted at 8 different time instants from 0.25 μs to 2 μs. Time of impact is 0 μs. In (a), the normal wave arrives at the left interface of the specimen at 0.45 μs, while the shear wave arrives at 0.86 μs. A uniform increase in temperature is observed across the specimen initially. A little while after the arrival of the shear wave, between 1 and 1.25 μs, the temperature increase begins to localize in a shear band. The band width is measured to be roughly 3.7 μm. Temperatures increase to as high as 1155 K within the band at 2 μs. In (b), the normal wave arrives at the left interface of the specimen at 0.38 μs, while the shear wave arrives at 0.65 μs. The temperature rises uniformly in the specimen after the arrival of the normal wave and begins to localize at ~0.75 μs (the

left band). Within a few nanoseconds, temperature begins to localize in a second band on the right. Two shear bands form, with a width of ~3.8 μm and ~2.8 μm for the left and right bands respectively. The corresponding peak temperatures are 1600 K and 1325 K respectively at t = 2 μs.

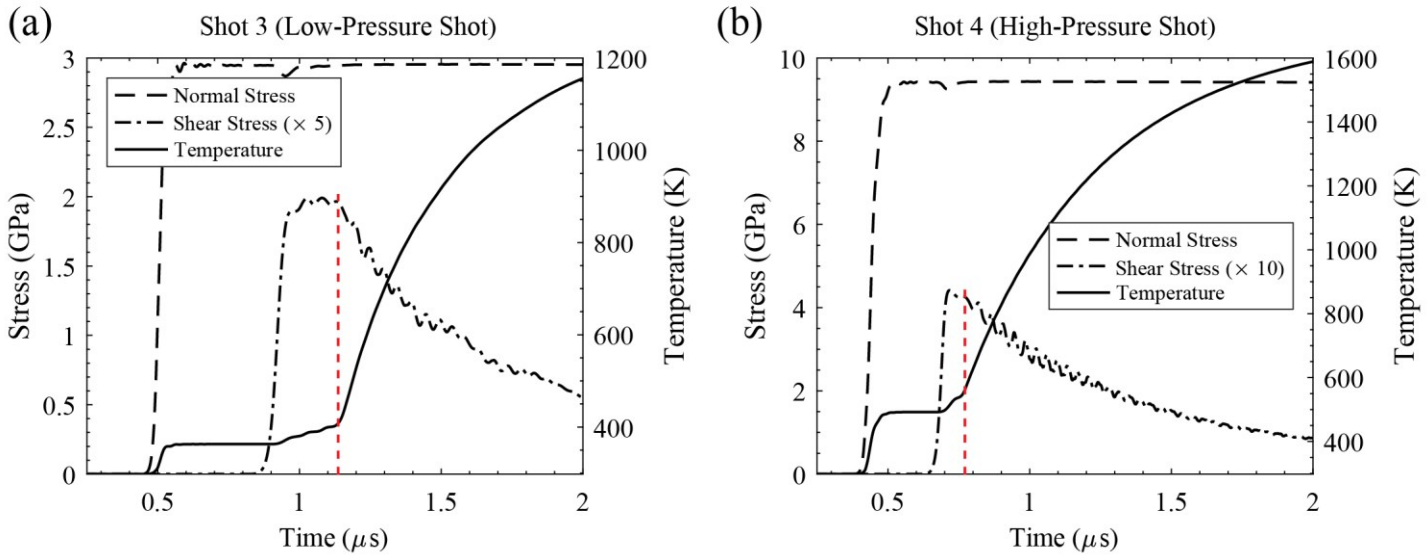

Fig. 20 Normal and shear stress profiles for a material point in the middle of the shear band for (a) Shot3 (low-pressure shot) and (b) Shot4 (high-pressure shot). For Shot4, stresses and temperature are plotted for the left shear band. Shear stress profiles are scaled for better visualization. Stress and temperature are shown on the left and right vertical axis respectively. All values are plotted for the integration point of the element in the middle of the shear band. In (a), temperature is observed to rise steeply at ~1.13 μs which coincides with a drop in shear stress, indicating the onset of localization (shown using a vertical dashed red line). In (b), the corresponding localization time is ~0.75 μs.

4.3 Discussion

Even though sucrose has a long history of being used as an energetic simulant, material models for sucrose have not been developed that account for the shearing behavior over a wide pressure range. In this section, a material model of sucrose with a complete equation of state and a thermo-viscoplasticity model for strength was shown to adequately capture the experimentally observed shearing response in PSPI. Simulations show that the fall in the shear strength of sucrose is a result of a thermo-viscoplastic instability in the form of adiabatic shear bands. It is also shown that normal compression can lead to a significant temperature increase, especially at higher pressures. The model can be applied to consider more complex phenomena like pore collapse or shear band formation under complex loading scenarios. The contribution of thermoelastic heating to the temperature increase is significant and can affect the shearing response upon arrival of the shear wave, as discussed below. Therefore, for accurate determination of temperatures and shearing behavior under complex loading, a complete equation of state with a temperature-dependent specific heat capacity is required. If a constant value of the specific heat capacity at the ambient conditions are used, the temperature increase would be overpredicted. It is shown that melting eventually occurs in the shear bands. The choice of the melt curve can significantly affect the shearing behavior as discussed below. Accurate modeling of material behavior beyond melt requires consideration of solid-liquid phase transition, latent heat of melting and a constitutive relation for the molten liquid, especially the shear viscosity of the liquid. Lack of experimental data for molten energetic crystals or their simulants makes it difficult to validate material models for the melt. Modeling the liquid phase, especially the pressure and temperature dependent shear viscosity, is important in simulations of phenomena such as pore-collapse. However, the attention of this study is limited to the solid phase before melt. It is assumed that beyond melt, the solid loses its strength completely while maintaining a constant limiting shear strain-rate (Grunschel, 2009). Such an assumption can be relaxed when better models of the phase transition to the liquid phase and shear resistance of the melt phase become available.

4.3.1 Thermoelastic work

A significant temperature increase is expected from elastic compression of sucrose, as predicted by the isentropic temperature increase in Fig. 14. It is important to accurately model this temperature increase for the PSPI experiments as it significantly impacts the subsequent material response upon the arrival of the shear wave. Some plastic work is also expected during normal compression which leads to an additional temperature rise. However, separating the thermo-elastic and thermo-viscoplastic temperature changes during normal loading analytically is not possible due to the non-

linear coupling of the two effects. It is, however, possible to separate the two contributions in numerical simulations. Considering the specific heat to be constant for a given time-step, the temperature increase due to thermo-elasticity during that time step can be calculated from equation (4.3) below. Such an approach is valid for the small time-steps used here, which ensure that the variation in the specific heat during a time-step is small. The temperature change due to thermoelastic work for a time-step can be calculated as:

$$\Delta\theta = \frac{\Delta q^e}{\rho c(\theta)}, \tag{4.3}$$

where the thermo-elastic heat increment, $\Delta q^e = \dot{q}^e \Delta t$, is calculated in the deformed configuration (see equation (C.10) in Appendix C). Simulated predictions are compared with the theoretical predictions for isentropic hydrostatic compression of a single elastic 3D element. Near perfect agreement is seen between the analytical and computational results (see Fig. 21), verifying the method for separating temperature increase due to elastic and viscoplastic deformations.

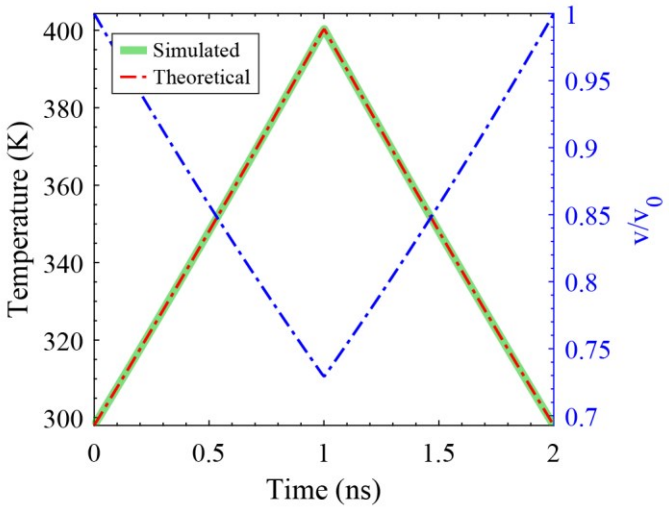

Fig. 21 Simulated (solid green line) and theoretical (red dashed line) temperature profiles of a single elastic 3D element subjected to a ramp volumetric strain. The imposed loading is a linear variation of the compression ratio from 1.0 to 0.73 over a duration of 1 ns followed by a reversal to the original state at the same rate.

The temperature increase at the middle of the shear band is plotted for low and high-pressure shots (Shot3 and Shot4) as a function of pressure in Fig. 22. Each plot shows the overall total temperature, the thermoelastic contribution (numerically calculated $\theta^{(e)}$), the theoretical isentropic temperature $\theta^{(\eta)}$ and the evolution of the melting point with pressure according to two models (Lindemann and Simon-Glatzel). Note that the vertical increase in the temperature at the right end of the plot corresponds to heating upon the formation of the shear band. Also note that $\theta^{(e)}$ and $\theta^{(\eta)}$agree with each other very well. The difference between the total temperature increase (red curve) and thermoelastic temperature increase (black curve) is the contribution from viscoplastic dissipation, which is comparable to the thermoelastic contribution, prior to the formation of the shear band, especially in the higher pressure case. For the low-pressure shot, the thermoelastic and viscoplastic contributions to the temperature increase are 42 K and 23 K respectively. The corresponding numbers for the high pressure case are 117 K and 77 K. Two main conclusions that can be drawn from Fig. 22 are: (a) the temperature increase during normal wave loading is substantial and (b) the thermoelastic and viscoplastic contributions to the temperature increase during normal wave loading are comparable to each other, especially at the higher pressure. Hence, it is important to include the thermoelastic term in a thermo-mechanically coupled model for energetic materials and their simulants.

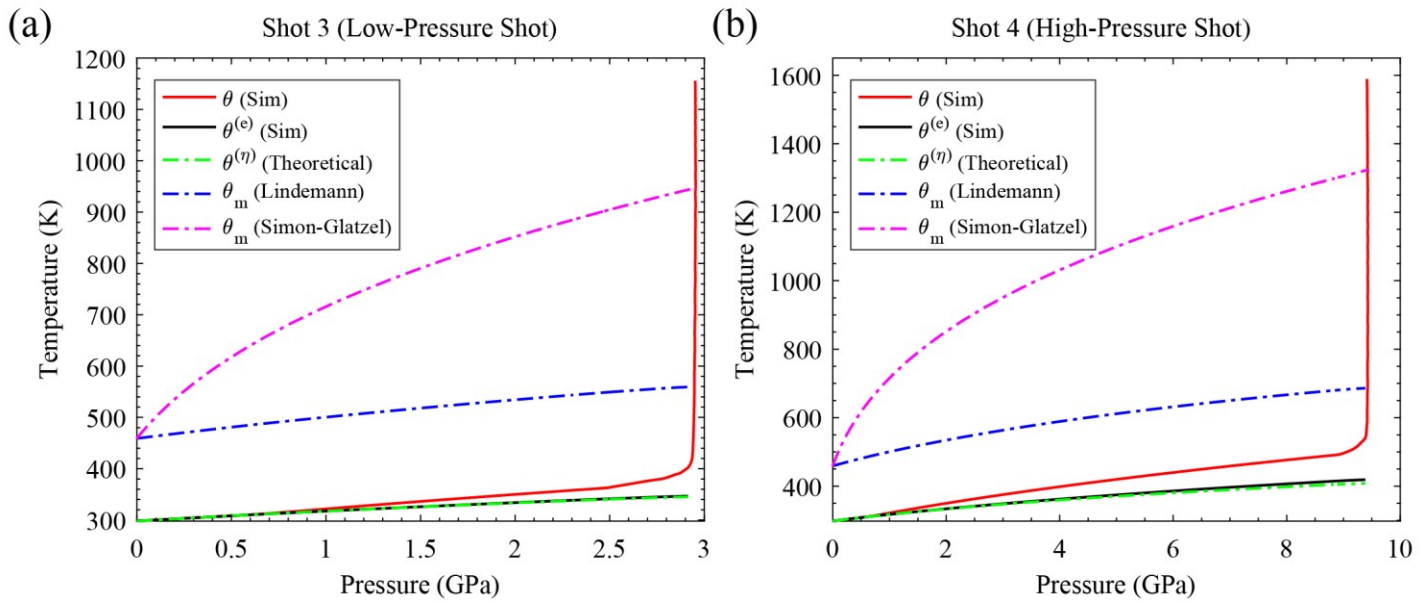

Fig. 22 Simulated temperature profiles as a function of pressure, plotted at the middle of the shear band for (a) Shot3 (low-pressure shot) and Shot4 (high-pressure shot). θ (solid red line) shows the simulated temperature profile using the Simon-Glatzel melting relation. A modest increase of 65 K is observed in temperature during normal wave loading in (a), while the corresponding temperature increase in (b) is 194 K, which is substantially larger. $\theta^{(e)}$ (solid black line) is the numerically calculated thermoelastic contribution to the temperature increase and $\theta^{(\eta)}$ (dashed green line) is the corresponding theoretically predicted isentropic temperature increase. θ_m (dashed blue line) is the melt curve for Lindemann Law and θ_m (dashed magenta line) is the melt curve for the Simon-Glatzel relation. In (a), the Lindemann Law predicts melting at 557 K while the Simon-Glatzel curve predicts melting at a much higher temperature of 947 K at a saturation pressure of 2.95 GPa. In (b), the Lindemann Law predicts melting at 686 K while the Simon-Glatzel curve predicts melting at a much higher temperature of 1323 K at a pressure of 9.45 GPa.

4.3.2 Melt Curve

The flow strength of sucrose is a strong function of the specimen temperature and its melt temperature, which is accounted for by the $(1-\hat{\theta}^m)$ factor in the Johnson-Cook model for the flow strength. However, the melting point of sucrose is itself a function of pressure (thus making the shear strength of sucrose dependent on pressure). Since the thermal factor in the Johnson-Cook model is responsible for thermal softening and hence a fall in the shear strength, it is important to consider the pressure-dependence of the melting point of sucrose, so that its shear behaviour can be simulated consistently for different pressures. Accurate representation of the melt curve is also important for the prediction of hot-spot formation. The shearing resistance of an energetic crystal drops to zero at melt, and the shear viscosity of the molten fluid takes over and results in significantly reduced dissipation compared to the viscoplastic dissipation of the solid phase. So, the melt curve dictates the amount of dissipation and hence the peak hot-spot temperatures during localization. Formation of hot-spots and their transition to ignition is highly temperature-sensitive under weak shocks, which emphasizes the importance of accurate prediction of the melting point as a function of pressure. However, measurement of the melting point for energetic crystals is difficult due to associated dissociation reactions. Therefore, experimentally measured melt curves are typically replaced by empirical laws. One such law is the Lindeman Law (Lindemann, 1910; Ross, 1969; Poirier and Tarantola, 1998):

$$\theta_m = \theta_{m0} \exp\left[2\Gamma_0\left(1-\frac{v}{v_0}\right)+\frac{2}{3}\ln\left(\frac{v}{v_0}\right)\right], \tag{4.4}$$

where θ_{m0} is the melt temperature at ambient temperature and pressure. Note that the Lindeman Law can be linearized in volume (Kraut-Kennedy relation) or in pressure (Menikoff and Sewell, 2002) but is not very accurate at high pressures as described in Menikoff and Sewell (2002) and Appendix B. Molecular dynamics simulations on HMX (Kroonblawd and Austin, 2021) show that the Lindemann Law grossly underestimates the melt temperature whereas the Simon-Glatzel relationship (equation (3.36)) fits the molecular dynamics data very well. In equation (3.36), (P_{ref}, P_i, d) are fitting parameters. Due to the lack of experimental data on the melt curve of sucrose as a function of pressure, parameters for the Simon-Glatzel fit used for HMX by Kroonblawd and Austin (2021) are employed here for sucrose. Fig. 23 shows a comparison between the shear stress profiles calculated using the Simon-Glatzel melt relation and the Lindemann melt curve for low and high-pressure cases. Other material parameters are kept the same for both cases. Using the Lindemann

Law results in a much lower shear strength than that observed experimentally. This is expected since a lower melt temperature, as predicted by the Lindemann Law, results in earlier melting and hence an earlier decrease in shear strength. Additionally, it results in a lower overall temperature due to decreased dissipation after melt, affecting the predictions of strength and temperature. On the other hand, the Simon-Glatzel melt relation captures the experimental data much better. A comparison between the two melting relations is also plotted in Fig. 22. It is observed that for the same pressure, the Lindemann Law predicts a much lower melt temperature than the Simon-Glatzel relation.

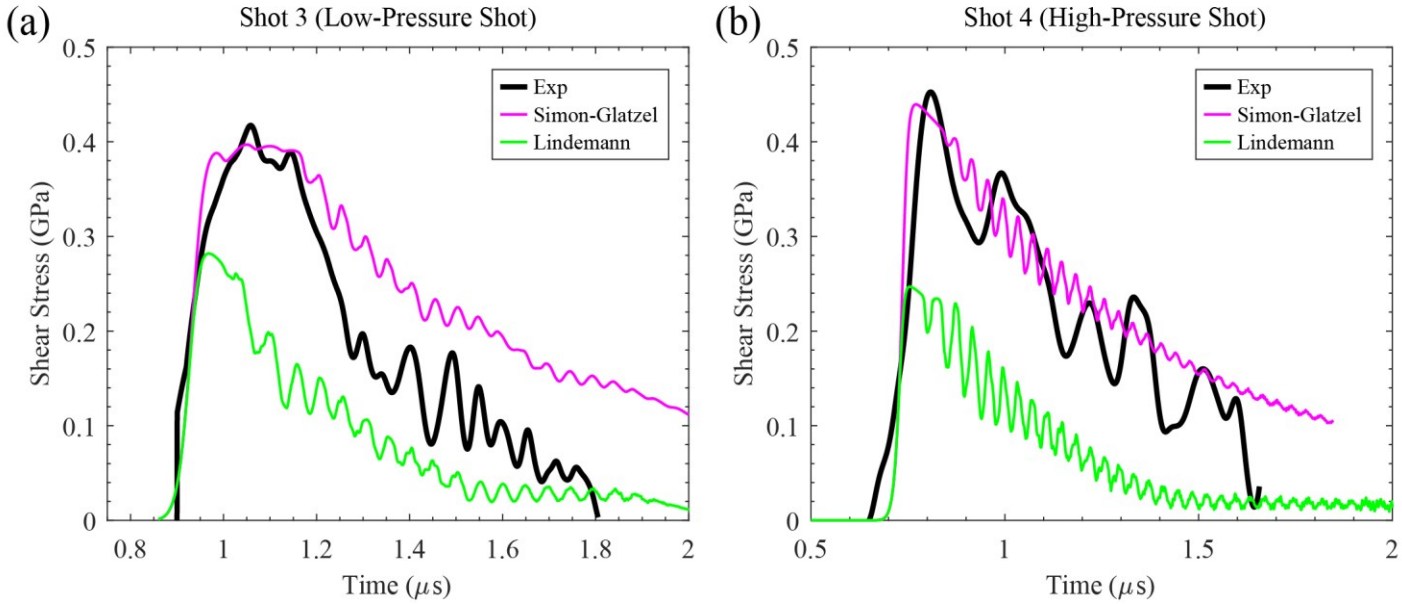

Fig. 23 Nominal shear stress vs time for (a) Shot3 (low-pressure shot) and (b) Shot4 (high-pressure shot). A comparison is drawn between the shear stress profiles obtained using the Simon-Glatzel melt relation and the Lindemann melt curve, keeping all other material parameters for sucrose the same.

4.3.3 Temperature and Volume-Dependent Shear Modulus

In the preceding sections, a constant value of the shear modulus was assumed. However, the shear modulus of sucrose is expected to be dependent on specific volume and temperature, especially at high pressures. A commonly used functional form of the shear modulus is a linear variation with both pressure and temperature, as described by Steinberg et al. (1980):

$$G(v,\theta) = G_0 + \frac{\partial G}{\partial P}\frac{P(v,\theta)}{\left(\frac{v_0}{v}\right)^{1/3}} + \frac{\partial G}{\partial \theta}(\theta - \theta_0), \tag{4.5}$$

where G_0 is the shear modulus at ambient pressure and temperature and $P(v,\theta)$ follows from the complete equation of state. The derivatives of the shear modulus with respect to pressure and temperature, i.e., $\frac{\partial G}{\partial P}$ and $\frac{\partial G}{\partial \theta}$, respectively, were assumed to be constant by Steinberg et al. (1980) for fitting experimental data of several metals. However, the shear modulus behaviour near melt is not well known, especially for energetic materials, and it is expected that the shear modulus drops to near zero after melt. A drastic drop in shear modulus at melt has been observed through shear wave measurements by Nadal and Le Poac (2003). The Steinberg model in equation (4.5) does not necessarily give a zero shear modulus at melt and does not consider the variation of the slope of the shear modulus-temperature curve, i.e., $\frac{\partial G}{\partial \theta}$, with pressure, near the melting point. These issues were addressed by Nadal and Le Poac (2003) who proposed a modified expression for the shear modulus that retains the linear variation of the shear modulus with pressure and temperature away from the melting point while addressing the sharp decrease in the shear modulus at melt through the incorporation of a temperature dependent pre-factor in equation (4.5).

Note that using a temperature dependent shear modulus will affect the expression for thermoelastic work derived in section 3.4. The spatial Gruneisen tensor, which is not spherical anymore, can be expressed as:

$$\boldsymbol{\Gamma} = -\frac{v}{c}\left(-\frac{\partial P}{\partial \theta}\boldsymbol{I} + \frac{2K_2}{J^e}\frac{\partial G}{\partial \theta}\boldsymbol{N}'\right). \tag{4.6}$$

Since $\boldsymbol{I}:\boldsymbol{D}^e = tr(\boldsymbol{D}^e) = \frac{\dot{J}^e}{J^e} = \dot{K}_1$ and $\boldsymbol{N}':\boldsymbol{D}^e = (\boldsymbol{E}_0^e:\boldsymbol{C}^{e^{-1}}\dot{\boldsymbol{C}}^e)/2K_2$, the simplified expression for thermoelastic work can be written as:

$$\dot{q}^{\boldsymbol{e}} = -\theta\frac{\partial P}{\partial \theta}\dot{K}_1 + \frac{\theta}{J^e}\frac{\partial G}{\partial \theta}\,\boldsymbol{E}_0^e:\boldsymbol{C}^{e^{-1}}\dot{\boldsymbol{C}}^e. \tag{4.7}$$

5 Summary and Concluding Remarks

In this study, an experimental investigation has been carried out on a commonly used energetic material simulant, sucrose, through PSPI experiments. To the best of our knowledge, this is the first investigation of its kind. Experiments have been performed at two different nominal normal stress values, 3 and 9.5 GPa, with nominal shear strain-rates of $1.5 - 2 \times 10^6\ s^{-1}$ and $3 \times 10^6\ s^{-1}$ for the low and high-pressure cases, respectively. The normal stress profiles show an initial elastic precursor, followed by a sharp rise to a plateau. No reverberations are observed in the normal velocity profiles due to the extreme thinness of the samples. The shear strength of sucrose shows a peak value followed by a dramatic drop after reaching a critical strain. The peak shear stress and the shear stress drop are consistently observed at both low and high pressures, although the critical strain at which the drop occurs varies with pressure. Such softening of the shear response of sucrose may be attributed to thermo-viscoplastic localized instabilities. It is worth noting that formation of adiabatic shear bands is a key mechanism of hot-spot formation in energetic crystals. The reported measurements on sucrose motivate the need to study the shear strength behavior of actual energetic crystals such as RDX and HMX under high-pressures and high strain-rates as the shear strength is expected to have direct implications for their ignition mechanisms. It should also be noted that the peak shear strength of sucrose displays minimal pressure-sensitivity, which is in contrast to the binders of polymer-bonded explosive systems (Malhotra, 2020; Malhotra et al., 2021). The shear strength of the binder is expected to surpass that of sucrose beyond a certain pressure which can lead to a reversal in the energy localization behavior and hence the subsequent hot-spot formation. Such a behavior has important consequences for ignition behavior of polymer-bonded explosives.

Next, a thermodynamically-consistent constitutive model for sucrose has been presented. Molecular crystals such as sucrose, HMX and RDX are complex materials to model under quasi-static and dynamic loads. The complexity arises due to several factors: (a) anisotropic elastic properties, (b) thermo-elastic coupling, (c) a complex thermo-viscoplastic response, (d) a low melting point, (e) strong dependence of material properties on temperature and pressure, such as the elastic moduli, specific heat, melt curve and viscosity of molten fluid to name a few, and (f) the added complexity of chemical reactions. Moreover, lack of experimental data on melt curves and temperature and pressure-dependencies of shear viscosity of the melt for energetic crystals makes determination of material parameters an arduous task. Here, the focus is restricted to modeling the solid phase before melting takes place. First, a thermodynamic foundation is presented for modeling the material behavior of a solid. The temperature evolution equation is derived using the laws of thermodynamics, with the thermoelastic work being represented in terms of the Gruneisen tensor. Next, the free energy is expressed in terms of invariants of a logarithmic strain measure. The use of logarithmic strains facilitates the additive decomposition of large strains into volumetric and deviatoric parts. As demonstrated above, using an adequate invariant basis (K_1, K_2, K_3), the Cauchy stress tensor can be additively decomposed into pressure and deviatoric stresses. Such a decomposition allows an independent focus on the equation of state of the material, which is typically measured through separate experiments. Consistent with the thermodynamic foundation laid before, a complete Mie-Gruneisen equation of state is derived by incorporating a temperature-dependent specific heat capacity. A complete equation of state allows for an accurate prediction of the thermoelastic temperature increase during extreme deformations such as in PSPI or shock loading, which bears important consequences for accurate prediction of deformation behavior and hot-spot formation in energetic crystals. Using this complete equation of state, analytical expressions for pressure and temperature are derived for the special cases of isothermal, isentropic and shock loading. The thermo-viscoplastic response is modeled using a Johnson-Cook model with a pressure-dependent melting curve.

Finite element simulations of PSPI experiments reveal that the shear softening is a result of the formation of a thermo-viscoplastic instability in the form of adiabatic shear bands. It is shown that the fall in shearing resistance is coincident with the sharp rise in local temperatures, which results in the formation of hot-spots. Therefore, adiabatic shear bands are identified as a potent hot-spot mechanism in energetic crystals subject to impact loading. It is also shown that the contribution of volumetric elastic compression to the temperature increase can be separated from that due to viscoplasticity in the numerical implementation. Large thermo-elastic temperature increases in simulations emphasize the importance of accurate modeling of the volumetric behavior of energetic materials through a complete equation of state.

The current study provides a good starting point in characterizing and modeling deformation behavior of an energetic material simulant. However, much remains to be done to fully understand the complex thermo-mechanical behavior of such molecular crystals both experimentally and theoretically. To begin with, localized temperature fields and strain-fields that eventually lead to hot-spots need to be measured with sufficient fidelity to provide reliable experimental data for modeling. As noted above, an important requirement is an accurate prediction of the melt curve as a function of pressure. Experimental evidence is needed to corroborate the models used. While such measurements are difficult to carry out with real energetic crystals due to the dissociation reactions associated with a temperature increase, simulants like sucrose provide a good opportunity in this regard. At the same time, it is important to incorporate the temperature and pressure dependence of the shear modulus, especially near melt. In the present work, the focus is kept on modeling the solid phase. However, since localized melting is expected in the adiabatic shear bands, it is important to incorporate a solid to liquid phase transition and the constitutive behavior of the liquid phase. So, the present framework needs to be extended to incorporate the above features, which remains a task for the future. Experimental characterization of shear viscosity as a function of temperature and pressure is expected to provide insights into the behavior of the molten phase and hence experimental corroboration of a constitutive model for the liquid phase. Such measurements also remain an avenue for future work. As the fraction of molten phase grows, dissipation is expected to drop. So, accurate prediction of temperature fields and associated material behaviors, such as ensuing chemical behaviors in the case of energetic crystals, requires accurate modeling of the phase transition as well. It should be noted that the experimental data on specific heat capacity of sucrose is available for a very small range of temperatures and extending such measurements to higher temperatures will increase confidence in the prediction of the temperature rise due to thermo-elasticity. As experimental techniques improve in the future, the above mentioned measurements may become feasible, and the current constitutive model can be extended to model such experiments.

Acknowledgements: The authors are thankful to AFOSR (Grant#FA9550-15-1-0415, Dynamic Materials and Interactions, Dr. Martin Schmidt) and NSF (Award #1825582) for supporting this work.

Appendix A. Derivation of a 3rd order equation of state

A 3rd-order polynomial free-energy function is used to derive an isothermal equation of state. Note that the final form of the equation of state depends on the volumetric strain measure used. The three most familiar measures of strain are the logarithmic strain, the Euler-Almansi strain and the Green-Lagrange strain. We begin with the logarithmic strain. Typically, a quadratic form of Helmholtz free energy is used. However, to model large non-linear deformations, a cubic term can be added, as follows:

$$\psi_R(K_1) = A_2 K_1^2 + A_3 K_1^3 + \cdots, \tag{A.1}$$

where ψ_R is the Helmholtz free energy per unit volume in the reference configuration, $K_1 (= \ln J = \ln(v/v_0))$ is the logarithmic volumetric strain, and A_2 and A_3 are constants. For the logarithmic strain measure, the pressure in the solid can be found from the trace of the Cauchy stress tensor $\boldsymbol{T}$ (as shown in equation (3.30)):

$$P = -\frac{tr(\boldsymbol{T})}{3} = -\frac{1}{J}\frac{\partial \psi_R}{\partial K_1} = -v_0 \frac{\partial \psi_R}{\partial v} = -K_1\, e^{-K_1}(2A_2 + 3A_3 K_1). \tag{A.2}$$

The constants A_2 and A_3 need to be expressed in terms of measurable material parameters such as the isothermal bulk modulus, $K_{\theta 0}$ and its first pressure derivative, $K'_{\theta 0}$, which are defined below:

$$K_{\theta 0} = -\left(v\frac{\partial P}{\partial v}\right)_{v_0,\theta_0}, \qquad K'_{\theta 0} = \left(\frac{\partial K_\theta}{\partial P}\right)_{v_0,\theta_0}. \tag{A.3}$$

The subscript '0' refers to the reference state of $(v_0, P_0 = 0, \theta_0 = 298\,K)$. It can be shown that $A_2 = K_{\theta 0}/2$ and $A_3 = K_{\theta 0}(2 - K'_{\theta 0})/6$. Substituting these relations into equation (A.2), the 3rd-order equation of state in terms of the logarithmic strain (Poirier and Tarantola, 1998) is written as:

$$P = K_{\theta 0}\left(\frac{v_0}{v}\right)\ln\left(\frac{v_0}{v}\right)\left[1 + \frac{K'_{\theta 0} - 2}{2}\ln\left(\frac{v_0}{v}\right)\right]. \tag{A.4}$$

Now, we derive the 3rd-order Birch-Murnaghan equation of state in terms of the Euler-Almansi strain, which is one of the most commonly encountered equations of state in shock physics and geophysics applications. For a purely volumetric deformation, the Euler-Almansi strain can be expressed as:

$$\boldsymbol{e} = \frac{\boldsymbol{I} - \boldsymbol{B}^{e^{-1}}}{2} = \frac{1 - J^{-2/3}}{2}\boldsymbol{I}, \tag{A.5}$$

where $\boldsymbol{B}^e = \boldsymbol{F}^e\boldsymbol{F}^{e^T}$ is the left Cauchy-Green tensor and $\boldsymbol{F}^e = J^{1/3}\boldsymbol{I}$ is the elastic deformation gradient for purely volumetric deformation. The volumetric Eulerian strain is defined as:

$$e = \frac{tr(\boldsymbol{e})}{3} = \frac{1}{2}\left(1 - J^{-2/3}\right). \tag{A.6}$$

Now, consider the Helmholtz free energy written in terms of the volumetric Eulerian strain, similar to equation (A.1), as:

$$\psi_R(e) = a_2e^2 + a_3e^3 + \cdots. \tag{A.7}$$

where a_2 and a_3 are constants. The pressure in the solid can be found using equation (3.38)

$$P = -\frac{\partial\psi}{\partial v} = -\frac{\partial\psi}{\partial e}\frac{\partial e}{\partial v} = -(2a_2e + 3a_3e^2)\left(\frac{1}{3J^{5/3}\,v_0}\right). \tag{A.8}$$

Using the definitions for $K_{\theta 0}$ and $K'_{\theta 0}$ from equation (A.3), it can be shown that $a_2 = 9v_0K_{\theta 0}/2$ and $a_3 = 9v_0K_{\theta 0}(4 - K'_{\theta 0})/2$. Substituting the values of a_2 and a_3 into equation (A.8), the 3rd-order Birch-Murnaghan equation of state can be written as:

$$P = \frac{3}{2}K_{\theta 0}\left[\left(\frac{v_0}{v}\right)^{\frac{7}{3}} - \left(\frac{v_0}{v}\right)^{\frac{5}{3}}\right]\left[1 + \frac{3}{4}(K'_{\theta 0} - 4)\left\{\left(\frac{v_0}{v}\right)^{\frac{2}{3}} - 1\right\}\right]. \tag{A.9}$$

On similar lines, consider the derivation of a 3rd-order equation of state in terms of the Green-Lagrange strain. For a purely volumetric deformation, the Green-Lagrange strain can be found to be:

$$\boldsymbol{E} = \frac{\boldsymbol{C}^e - \boldsymbol{I}}{2} = \frac{J^{2/3} - 1}{2}\boldsymbol{I}. \tag{A.10}$$

The volumetric Lagrangian strain E is defined as:

$$E = \frac{tr(\boldsymbol{E})}{3} = \frac{J^{2/3} - 1}{2}. \tag{A.11}$$

The referential Helmholtz free energy can be written in terms of the volumetric Lagrangian strain as:

$$\psi_R(E) = B_2E^2 + B_3E^3 + \cdots, \tag{A.12}$$

where B_2 and B_3 are constants. Combining equations (3.7) and (3.15), the Cauchy stress can be obtained from the derivative of free energy with respect to $\boldsymbol{C}^e$ as:

$$\boldsymbol{T} = \frac{2}{J^e}\boldsymbol{F}^e\frac{\partial\psi_R}{\partial\boldsymbol{C}^e}\,\boldsymbol{F}^{e^T}. \tag{A.13}$$

Since $\boldsymbol{F}^e = J^{1/3}\boldsymbol{I}$ and $\boldsymbol{C}^e = J^{2/3}\boldsymbol{I}$, the expression for pressure can be shown to be:

$$P = -\frac{tr(\boldsymbol{T})}{3} = -v_0\frac{\partial\psi_R}{\partial v} = -\frac{2}{J^{1/3}}(2B_2E + 3B_3E^2). \tag{A.14}$$

Following a procedure similar to the logarithmic and Eulerian strains, $B_2 = 3K_{\theta 0}/2$ and $B_3 = 3K_{\theta 0}K'_{\theta 0}/2$, which when substituted into equation (A.14) gives the 3rd-order equation of state derived using Lagrangian strain:

$$P = \frac{3}{2}K_{\theta 0}\left[\left(\frac{v_0}{v}\right)^{\frac{1}{3}} - \left(\frac{v_0}{v}\right)^{-\frac{1}{3}}\right]\left[1 + \frac{3}{4}K'_{\theta 0}\left\{1 - \left(\frac{v_0}{v}\right)^{-\frac{2}{3}}\right\}\right]. \tag{A.15}$$

A comparison of the 3rd-order equations of state using the 3 different strain measures is shown in Fig. A.1. It is evident that the Green-Lagrange strain leads to the most compliant behavior at the same volumetric compression while the Euler-Almansi strain leads to the stiffest behavior. The equations of state using the logarithmic strain and the Euler-Almansi strain are quite close to one another over the range of finite volumetric strains considered here. All three strain measures show agreement at small strains, which is to be expected.

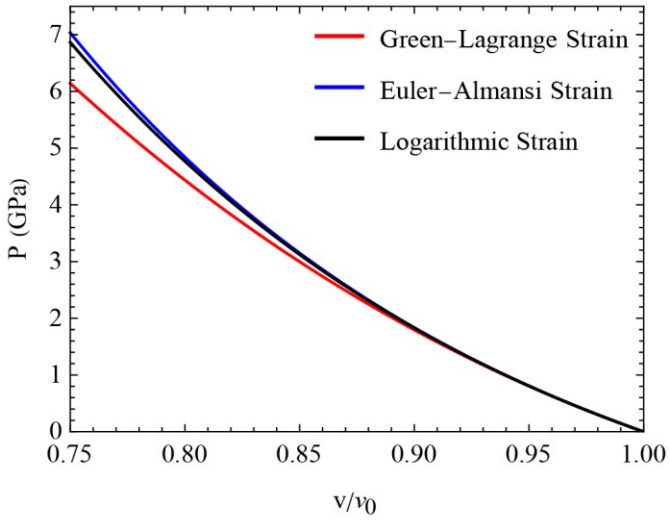

Fig. A.1 3rd order equations of state using 3 different strain measures.

Appendix B. Material Constants for Sucrose

Elastic Constants

Bulk Modulus

Bridgman made measurements of compression ratios of sucrose under pressures up to 3 GPa (see Table V in Bridgman (1949)). The values of the bulk modulus of sucrose as a function of pressure are tabulated below.

Table B.1 Bulk modulus of sucrose measured at different pressures. Bulk moduli and volumetric changes are calculated based on Table V in Bridgman (1949).

Pressure (kg/cm^2)	Pressure (GPa)	$1 - J$	Bulk Modulus (GPa)
5,000	**0.5**	**0.03151**	**15.868**
10,000	1	0.05518	18.122
15,000	1.5	0.07434	20.178
20,000	2	0.09074	22.041
25,000	2.5	0.10552	23.692
30,000	3	0.11866	25.282

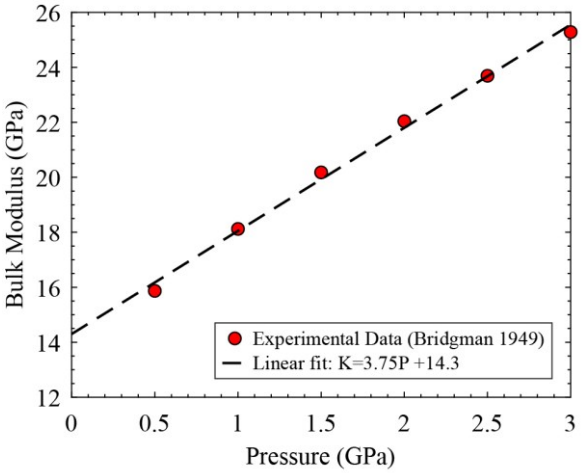

Fig. B.1 Linear fit to the experimental data for the isothermal bulk modulus of sucrose

Fig. B.1 indicates the pressure dependence of the bulk modulus for sucrose. $K_{\theta 0} = 14.3\ GPa$ and $K'_{\theta 0} = 3.75$ are obtained using a linear fit to the experimental data. $K_{\theta 0}$ is the isothermal bulk modulus at ambient temperature and pressure while $K'_{\theta 0}$ is the first derivative of the bulk modulus with respect to pressure at ambient temperature and pressure. These values are very close to the data obtained from Bridgman (1933).

Poisson's Ratio and Shear Modulus

(Trott et al., 2007) used a Poisson's ratio of 0.25 for sucrose. Using $K_{\theta 0} = 14.3\ GPa$ and $\nu = 0.25$, $G_0 = 21.45\ GPa$ is obtained.

Thermal Constants

Coefficient of Thermal Expansion

A mean volumetric coefficient of thermal expansion of $\alpha_v = 140.1 \times 10^{-6}\ ^{\circ}\mathrm{C}^{-1}$ was reported by (Bridgman, 1933) over a temperature range from $30\ ^0C$ to $75\ ^0C$.

Specific Heat

Specific heat capacity at constant pressure, c_p was reported by (Anderson et al., 1950) over a temperature range from $25\ ^0C$ to $90\ ^0C$. The experimental data is given in B.2. In order to derive the specific heat capacity at constant volume c_v the following thermodynamic relation can be used:

$$c_p - c_v = v\theta\alpha_v^2 K_\theta, \tag{B.1}$$

where $v = V/m$ is specific volume, and K_θ is the isothermal bulk modulus. Note that the specific heat at constant volume has been represented by c in the main text. However, in this appendix c_v is used for the specific heat at constant volume to differentiate it from the specific heat at constant pressure, c_p. It can be seen from Table B.2 that the difference in c_p and c_v values is relatively small.

Table B.2 Specific heat capacities of sucrose. c_p values are direct experimental measurements while c_v values are derived from thermodynamic constraints.

Temp (K)	$c_p\left(\frac{J}{kg\ K}\right)$ (Experimentally Measured)	$c_v\ (= c_p - v\theta\alpha_v^2 K_\theta)$
275.6	1137.98	1087.331
281.9	1167.32	1115.513
289.7	1200.32	1147.079
296.2	1255.32	1200.885

296.8	1234.54	1179.995
296.9	1238.21	1183.646
299.4	1250.43	1195.407
301.2	1250.43	1195.076
302.8	1263.88	1208.232
313	1313.99	1256.467
320.3	1351.89	1293.026
342.4	1476.56	1413.634
362.7	1581.68	1515.024

Fitting to the Debye Relation

Using a complete equation of state requires a temperature-dependent specific heat capacity. However, experimentally measured values are not available for the entire temperature range of interest. So, the specific heat capacity is fit to the well-known Debye model of specific heat capacity:

$$c_v = \frac{9R_0}{M}\left(\frac{\theta}{\theta_D}\right)^3 \int_0^{\theta_D/\theta} \frac{x^4 e^x}{(e^x-1)^2} dx = 3A\left(\frac{\theta}{\theta_D}\right)^3 \int_0^{\theta_D/\theta} \frac{x^4 e^x}{(e^x-1)^2} dx \tag{B.2}$$

where $R_0 = 8.314 \frac{J}{K\ mol}$ is the universal gas constant and M is the molar mass in kg/mol, θ_D is Debye temperature and $A = \frac{3R_0}{M}$. As $\theta \to 0, c_v \to 0$, and as $\theta \to \infty, c_v \to fR_0/M$ where the latter asymptotic limit is referred to as the Dulong-Petit limit. f represents the degrees of freedom contributing to the specific heat. For a monoatomic molecule, $f = 3$. However, for complex polyatomic molecules like HMX and sucrose, the number of degrees of freedom is very large. For any non-linear molecule, the total degrees of freedom is $3N$ (3 translational, 3 rotational and 3N-6 vibrational) where N is the number of atoms in the molecule. Hence, the Dulong-Petit limit of specific heat should be $c_v \to 3NR_0/M$ as $\theta \to \infty$. However, as is noted in (Menikoff and Sewell, 2002), some of the vibrational degrees of freedom corresponding to C-H bond stretching in HMX do not contribute to the specific heat capacity (as the vibrational frequencies of C-H bonds are very high and these modes are not very highly populated). Therefore, for HMX, the Dulong-Petit limit is expected to be $c_v \to (3 \times 28 - 8)R_0/M$ as $\theta \to \infty$, where number of atoms in HMX is 28 and number of C-H bonds is 8. However, no such information is available about the vibrational frequencies of C-H bonds in sucrose. So, to begin with, a conservative limit for the specific heat of sucrose is assumed, i.e., as $\theta \to \infty, c_v \to \frac{3\times 45R_0}{M} = 3279 \frac{J}{kg\ K}$ $(M = 342.3\ g/mol)$.

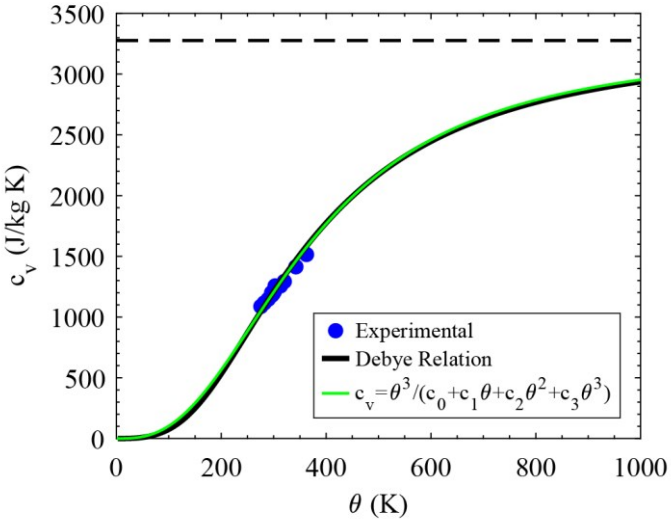

Fig. B.2 The Debye model fit to experimental data for the specific heat capacity at constant volume for sucrose.

In the form for Debye model (equation B.2), $c_v \to A \; as \; \theta \to \infty$, and hence A is the Dulong-Petit limit. There are two unknown constants for a fit to experimental data in the Debye form of specific heat, i.e., A and θ_D. The Debye expression is fit to the experimental specific heat data for sucrose assuming $A = 3279 \frac{J}{kg\,K}$ and $\theta_D = 1500\ K$ as shown in Fig. B.2. Since the experimental data for sucrose is available only for a small range of temperatures, a more accurate estimate of the Dulong-Petit Limit (A) would lead to a better extrapolation of the specific heat at elevated temperatures (θ >400K).

Fitting to an Empirical form: $\widetilde{c_v}(\tilde{\theta}) = \frac{\tilde{\theta}^3}{c_0+c_1\tilde{\theta}+c_2\tilde{\theta}^2+c_3\tilde{\theta}^3}$

In order to provide a simpler expression to calculate the specific heat and enable the integration of the Debye form, the specific heat is fit to the empirical form shown below, as done for HMX by (Sewell and Menikoff, 2004):

$$\widetilde{c_v}(\tilde{\theta}) = \frac{\tilde{\theta}^3}{c_0 + c_1\tilde{\theta} + c_2\tilde{\theta}^2 + c_3\tilde{\theta}^3} \tag{B.3}$$

where (c_0, c_1, c_2, c_3) are constants. Such a form is chosen as it obeys the asymptotic limits at the two temperature extremes, i.e., $\widetilde{c_v}(\tilde{\theta}) \to \tilde{\theta}^3 \; as \; \tilde{\theta} \to 0$ and $\widetilde{c_v}(\tilde{\theta}) \to \frac{3R_0}{M} = \frac{1}{c_3} as \; \tilde{\theta} \to \infty$ (Dulong-Petit Limit). A fit to the Debye relation for the specific heat capacity using the empirical form is shown in Fig. B.2. It can be seen from the plot that the empirical relation fits the Debye Model very well. The following set of parameters are used for this fit: $c_0 = 7.095 \times 10^3 \frac{kgK^4}{J}$, $c_1 = 2.230 \times 10^1 \frac{kgK^3}{J}$, $c_2 = 4.180 \times 10^{-3} \frac{kgK^2}{J}$ and $c_3 = 3.050 \times 10^{-4} \frac{kgK}{J}$. An explicit expression for the integral of the specific heat capacity with temperature is still difficult to evaluate using the empirical relation for specific heat (equation B.3). Therefore, the integral is calculated numerically, and a cubic polynomial is fit, as shown in Fig. B.3. A simple cubic polynomial is able to fit the data very well.

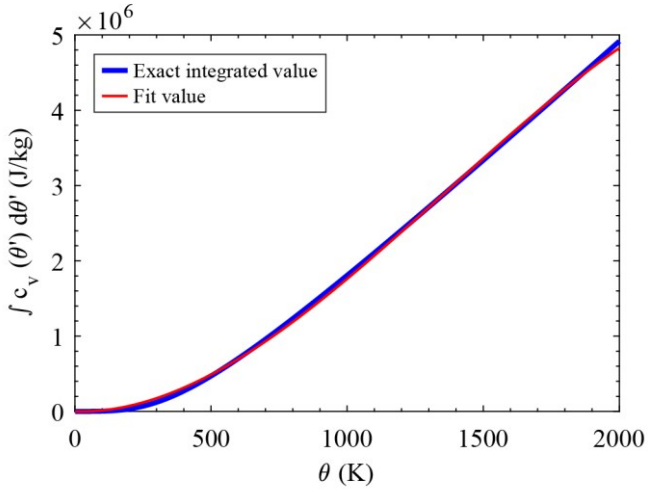

Fig. B.3 $\int_0^\theta c_v(\theta')d\theta'$ is evaluated numerically (thick blue curve) and fit to a cubic function (thin red curve)

Therefore, the approximation is given as: $\int_0^\theta c_v(\theta')d\theta' \approx (a_1\theta + a_2\theta^2 + a_3\theta^3)\frac{J}{kg}$ where $a_1 = -105.517$ J/kgK, $a_2 = 2.473$ J/kgK^2 and $a_3 = -6.067 \times 10^{-4}$ J/kgK^3 are found through least squares fit.

Thermal Conductivity

A thermal conductivity value of 0.486 W/m K was reported in (Trott et al., 2007).

Mechanical Properties

Yield Strength

Nanoindentation measurements of sucrose by (Ramos and Bahr, 2007) estimated a hardness of 1.5 GPa suggesting a bulk yield strength of 500 MPa, which motivates the use of $A = 500\ MPa$ in the Johnson-Cook model.

Gruneisen parameter

The following functional form of the Gruneisen parameter is assumed as noted by (Grady, 2017): $\Gamma(v) = \frac{\Gamma_0}{v_0} v$. The value of Γ_0 is derived from the following thermodynamic relation to be consistent with values for other thermodynamic quantities under ambient conditions:

$$\frac{\Gamma(v)}{v} = \frac{\alpha_v K_\theta}{c_v}. \tag{B.4}$$

At ambient, $\Gamma_0 = 1.09$ is obtained which is very close to that for HMX ($\Gamma_{0_{HMX}} = 1.1$). The integrating factor $\phi(v)$ can now be calculated explicitly:

$$\phi(v) = \exp\left(-\int_{v_0}^{v} \frac{\Gamma(v')}{v'} dv'\right) = \exp\left(-\int_{v_0}^{v} \frac{\Gamma_0}{v_0} dv'\right) = \exp\left(\Gamma_0\left(1 - \frac{v}{v_0}\right)\right). \tag{B.5}$$

Appendix C. VUMAT Algorithm

Given: $(\boldsymbol{F}_{n+1}, \theta_{n+1})$ and $(\boldsymbol{F}_n, \boldsymbol{F}_n^p, \boldsymbol{D}_n^p, \bar{\epsilon}_n^p)$ at time t_n.
Calculate: $(\boldsymbol{T}_{n+1}, \boldsymbol{F}_{n+1}^p, \boldsymbol{D}_{n+1}^p, \bar{\epsilon}_{n+1}^p, \Delta q^e, \Delta q^p)$ at time $t_{n+1} = t_n + \Delta t$.

Step 1: Update the plastic distortion using a forward Euler discretization of the evolution equation, $\dot{\boldsymbol{F}}^{\boldsymbol{p}} = \boldsymbol{D}^{\boldsymbol{p}}\boldsymbol{F}^{\boldsymbol{p}}$:

$$\boldsymbol{F}_{n+1}^p = \left(\boldsymbol{I} + \Delta t \boldsymbol{D}_n^p\right)\boldsymbol{F}_n^p. \tag{C.1}$$

Step 2: Update the elastic distortion and associated kinematic quantities:

$$\begin{aligned} \boldsymbol{F}_{n+1}^e &= \boldsymbol{F}_{n+1}\left(\boldsymbol{F}_{n+1}^p\right)^{-1}, \\ J_{n+1}^e &= \det(F_{n+1}^e), \\ v_{n+1} &= v_0 J_{n+1}^e, \\ \boldsymbol{U}_{n+1}^{\boldsymbol{e}} &= \sqrt{(\boldsymbol{F}_{n+1}^e)^T \boldsymbol{F}_{n+1}^e}, \\ \boldsymbol{R}_{n+1}^e &= \boldsymbol{F}_{n+1}^e (\boldsymbol{U}_{n+1}^e)^{-1}, \\ \boldsymbol{E}_{n+1}^e &= \ln(\boldsymbol{U}_{n+1}^e). \end{aligned} \tag{C.2}$$

Step 3: Update the pressure using the complete equation of state:

$$\begin{aligned} P_{n+1} = &-\frac{K_{\theta 0}}{J_{n+1}^e} ln(J_{n+1}^e)\left[1 - \frac{K'_{\theta 0} - 2}{2} ln(J_{n+1}^e)\right] \\ &+ \frac{\Gamma_0}{v_0}\phi(v_{n+1})\left[a_1\left(\tilde{\theta}_{n+1} - \tilde{\theta}_0\right) + a_2\left(\tilde{\theta}_{n+1}^2 - \tilde{\theta}_0^2\right) + a_3(\tilde{\theta}_{n+1}^3 - \tilde{\theta}_0^3)\right], \\ with \quad \phi(v_{n+1}) = &\exp\left[-\Gamma_0\left(\frac{v_{n+1}}{v_0} - 1\right)\right], and\ \tilde{\theta}_{n+1} = \frac{\theta_{n+1}}{\phi(v_{n+1})}. \end{aligned} \tag{C.3}$$

Step 4: Update the Mandel and Cauchy stresses:

$$\begin{aligned} \boldsymbol{M}_{n+1}^e &= 2G\boldsymbol{E}_{0,n+1}^e - P_{n+1}J_{n+1}^e\boldsymbol{I}, \\ \boldsymbol{T}_{n+1} &= \frac{1}{J_{n+1}^e}\boldsymbol{R}_{n+1}^e\boldsymbol{M}_{n+1}^e(\boldsymbol{R}_{n+1}^e)^T, \\ \overline{\sigma_{n+1}} &= \sqrt{\frac{3}{2}}\left|\boldsymbol{M}_{0,n+1}^{\boldsymbol{e}}\right|. \end{aligned} \tag{C.4}$$

Step 5: Update the rate of plastic stretching $\boldsymbol{D}^p$.

a. Update the accumulated plastic strain:

$$\begin{aligned} \dot{\overline{\epsilon_n^p}} &= \sqrt{\frac{2}{3}}\left|\boldsymbol{D}_n^p\right|, \\ \overline{\epsilon_{n+1}^p} &= \overline{\epsilon_n^p} + \dot{\overline{\epsilon_n^p}}\Delta t. \end{aligned} \tag{C.5}$$

b. Calculate the melting temperature using the Simon-Glatzel relation:

$$\theta_{m,n+1} = \theta_{m0}\left(1 + \frac{P_{n+1} - P_{ref}}{P_i}\right)^{\frac{1}{d}},$$
$$\hat{\theta}_{n+1} = \frac{\theta_{n+1} - \theta_{ref}}{\theta_{m,n+1} - \theta_{ref}}. \tag{C.6}$$

c. Calculate the effective plastic strain-rate using the Johnson-Cook Model:

$$\left(\dot{\overline{\epsilon^p_{n+1}}}\right)_{JC} = \dot{\epsilon_0}\exp\left(\frac{1}{C}\left(\frac{\overline{\sigma_{n+1}}}{\left(A + B\left(\overline{\epsilon^p_{n+1}}\right)^n\right)\left(1 - \hat{\theta}^m_{n+1}\right)} - 1\right)\right). \tag{C.7}$$

d. Update the effective plastic strain-rate, ensuring that it remains bounded for cases in which $\theta_{n+1} > \theta_{m,n+1}$:

$$\frac{1}{\dot{\overline{\epsilon^p_{n+1}}}} = \frac{1}{\left(\dot{\overline{\epsilon^p_{n+1}}}\right)_{JC}} + \frac{1}{\dot{\epsilon^p_{lim}}}. \tag{C.8}$$

e. Update $\boldsymbol{D}^p$:

$$\boldsymbol{D}^p_{n+1} = \frac{3}{2}\frac{\dot{\overline{\epsilon^p_{n+1}}}}{\bar{\sigma}_{n+1}}\boldsymbol{M}^e_{0,n+1}. \tag{C.9}$$

Step 6: Calculate Δq^e.

$$\Delta q^e = \Delta t\, \dot{q^e} = -\theta_{n+1}\, c_{v,n+1}\frac{\Gamma_0}{v_0}(\ln J^e_{n+1} - \ln J^e_n),$$
$$c_{v,n+1} = \frac{\tilde{\theta}^3_{n+1}}{c_0 + c_1\tilde{\theta}_{n+1} + c_2\tilde{\theta}^2_{n+1} + c_3\tilde{\theta}^3_{n+1}}, \tag{C.10}$$
$$J^e_n = \det\left(\boldsymbol{F}_n\boldsymbol{F}^{p^{-1}}_n\right).$$

Step 7: Calculate Δq^p.

$$\Delta q^p = \Delta t\, \dot{q^p} = \frac{\beta}{J^e_{n+1}}\bar{\sigma}_{n+1}\dot{\overline{\epsilon^p_{n+1}}}\Delta t. \tag{C.11}$$

6 References

Altynova, M., Hu, X., Daehn, G.S., 1996. Increased ductility in high velocity electromagnetic ring expansion. Metall. Mater. Trans. A Phys. Metall. Mater. Sci. 27, 1837–1844. https://doi.org/10.1007/BF02651933

Anand, L., 1986. Moderate deformations in extension-torsion of incompressible isotropic elastic materials. J. Mech. Phys. Solids 34, 293–304. https://doi.org/10.1016/0022-5096(86)90021-9

Anand, L., 1979. On H. Hencky's approximate strain-energy function for moderate deformations. J. Appl. Mech. Trans. ASME 46, 78–82. https://doi.org/10.1115/1.3424532

Anderson, G.L., Higbie, H., Stegeman, G., 1950. The Heat Capacity of Sucrose from 25 to 90°. J. Am. Chem. Soc. 72, 3798–3799. https://doi.org/10.1021/ja01164a503

Austin, R.A., Barton, N.R., Reaugh, J.E., Fried, L.E., 2015. Direct numerical simulation of shear localization and decomposition reactions in shock-loaded HMX crystal. J. Appl. Phys. 117, 185902. https://doi.org/10.1063/1.4918538

Barton, N.R., Winter, N.W., Reaugh, J.E., 2009. Defect evolution and pore collapse in crystalline energetic materials. Model. Simul. Mater. Sci. Eng. 17, 35003. https://doi.org/10.1088/0965-0393/17/3/035003

Becker, R., 2004. Effects of crystal plasticity on materials loaded at high pressures and strain rates. Int. J. Plast. 20, 1983–2006. https://doi.org/10.1016/j.ijplas.2003.09.002

Beevers, C.A., McDonald, T.R.R., Robertson, J.H., Stern, F., 1952. The crystal structure of sucrose. Acta Crystallogr. 5, 689–690. https://doi.org/10.1107/s0365110x52001908

Bowden, F.P., Yoffe, A.D., 1958. Fast Reactions in Solids. Butterworths: London.

Bowden, F.P., Yoffe, A.D., 1952. Initiation and growth of explosion in liquids and solids. Cambridge University Press.
Bridgman, P.W., 1949. Linear Compressions to 30,000 Kg/Cm^3, including Relatively Incompressible Substances. Proc. Am. Acad. Arts Sci. 77, 189. https://doi.org/10.2307/20023541
Bridgman, P.W., 1933. Compressibilities and Pressure Coefficients of Resistance of Elements, Compounds, and Alloys, Many of Them Anomalous. Proc. Am. Acad. Arts Sci. 68, 27. https://doi.org/10.2307/20022931
Cawkwell, M.J., Sewell, T.D., Zheng, L., Thompson, D.L., 2008. Shock-induced shear bands in an energetic molecular crystal: Application of shock-front absorbing boundary conditions to molecular dynamics simulations. Phys. Rev. B - Condens. Matter Mater. Phys. 78, 014107. https://doi.org/10.1103/PhysRevB.78.014107
Ciezak-Jenkins, J.A., Jenkins, T.A., 2018. Mechanochemical induced structural changes in sucrose using the rotational diamond anvil cell. J. Appl. Phys. 123, 085901. https://doi.org/10.1063/1.5020231
Clayton, J.D., 2014. Analysis of shock compression of strong single crystals with logarithmic thermoelastic-plastic theory. Int. J. Eng. Sci. 79, 1–20. https://doi.org/10.1016/j.ijengsci.2014.02.016
Clifton, R.J., Song, S., Jiao, T., 2020. Inverse problem for PSPI experiments, in: AIP Conference Proceedings. American Institute of Physics Inc., p. 070008. https://doi.org/10.1063/12.0000789
Coffey, C.S., Sharma, J., 2001. Lattice softening and failure in severely deformed molecular crystals. J. Appl. Phys. 89, 4797–4802. https://doi.org/10.1063/1.1358319
Criscione, J.C., Humphrey, J.D., Douglas, A.S., Hunter, W.C., 2000. Invariant basis for natural strain which yields orthogonal stress response terms in isotropic hyperelasticity. J. Mech. Phys. Solids 48, 2445–2465. https://doi.org/10.1016/S0022-5096(00)00023-5
Dick, J.J., Hooks, D.E., Menikoff, R., Martinez, A.R., 2004. Elastic-plastic wave profiles in cyclotetramethylene tetranitramine crystals. J. Appl. Phys. 96, 374–379. https://doi.org/10.1063/1.1757026
Duncan-Hewitt, W.C., Weatherly, G.C., 1990. Modeling the Uniaxial Compaction of Pharmaceutical Powders Using the Mechanical Properties of Single Crystals. II: Brittle Materials. J. Pharm. Sci. 79, 273–278. https://doi.org/10.1002/jps.2600790319
Duncan-Hewitt, W.C., Weatherly, G.C., 1989. Evaluating the hardness, Young's modulus and fracture toughness of some pharmaceutical crystals using microindentation techniques. J. Mater. Sci. Lett. 8, 1350–1352. https://doi.org/10.1007/BF00721518
Fried, E., Gurtin, M.E., 1993. Continuum theory of thermally induced phase transitions based on an order parameter. Phys. D Nonlinear Phenom. 68, 326–343. https://doi.org/10.1016/0167-2789(93)90128-N
Funk, D.J., Laabs, G.W., Peterson, P.D., Asay, B.W., 1996. Measurement of the stress/strain response of energetic materials as a function of strain rate and temperature: PBX 9501 and mock 9501, in: AIP Conference Proceedings. American Institute of PhysicsAIP, pp. 145–148.
Grady, D., 2017. Physics of Shock and Impact, Volume 2 Materials and shock response, Physics of Shock and Impact, Volume 2 Materials and shock response. IOP Publishing. https://doi.org/10.1088/978-0-7503-1257-8
Grady, D.E., Benson, D.A., 1983. Fragmentation of metal rings by electromagnetic loading - Fragmentation studies on rapidly expanding metal rings are performed with electromagnetic loading. Dynamic-fracture strain and fragment-size measurements are reported for aluminum and copper. Exp. Mech. 23, 393–400. https://doi.org/10.1007/BF02330054
Gray III, G., Idar, D., Blumenthal, W., Cady, C., Peterson, P., 1998. High-and low-strain rate compression properties of several energetic material composites as a function of strain rate and temperature.
Grunschel, S., 2009. Pressure -shear plate impact experiments on high-purity aluminum at temperatures approaching melt. Brown University.
Guduru, P., Freund, L., 2002. The dynamics of multiple neck formation and fragmentation in high rate extension of ductile materials. Int. J. Solids Struct. 39, 21–22. https://doi.org/https://doi.org/10.1016/S0020-7683(02)00367-0
Gurtin, M.E., Fried, E., Anand, L., 2010. The Mechanics and Thermodynamics of Continua, The Mechanics and Thermodynamics of Continua. Cambridge University Press. https://doi.org/10.1017/cbo9780511762956
Haussühl, S., 2001. Elastic and thermoelastic properties of selected organic crystals: Acenaphthene, trans-azobenzene, benzophenone, tolane, trans-stilbene, dibenzyl, diphenyl sulfone, 2,2′-biphenol, urea, melamine, hexogen, succinimide, pentaerythritol, urotropine, malonic acid, dimethyl malonic acid, maleic acid, hippuric acid, aluminium acetylacetonate, iron acetylacetonate, and tetraphenyl silicon. Zeitschrift fur Krist. 216, 339–353. https://doi.org/10.1524/zkri.216.6.339.20342
Haycraft, J.J., Stevens, L.L., Eckhardt, C.J., 2006. The elastic constants and related properties of the energetic material cyclotrimethylene trinitramine (RDX) determined by Brillouin scattering. J. Chem. Phys. 124, 024712. https://doi.org/10.1063/1.2141958
Heavens, S.N., Field, J.E., 1974. The ignition of a thin layer of explosive by impact. Proc. R. Soc. London. A. Math. Phys.

Sci. 338, 77–93. https://doi.org/10.1098/rspa.1974.0074
Hodowany, J., Ravichandran, G., Rosakis, A.J., Rosakis, P., 2000. Partition of plastic work into heat and stored energy in metals. Exp. Mech. 40, 113–123. https://doi.org/10.1007/BF02325036
Hooks, D.E., Ramos, K.J., Richard Martinez, A., 2006. Elastic-plastic shock wave profiles in oriented single crystals of cyclotrimethylene trinitramine (RDX) at 2.25 GPa. J. Appl. Phys. 100, 024908. https://doi.org/10.1063/1.2214639
Hu, Z., Luo, H., Bardenhagen, S.G., Siviour, C.R., Armstrong, R.W., Lu, H., 2015. Internal Deformation Measurement of Polymer Bonded Sugar in Compression by Digital Volume Correlation of In-situ Tomography. Exp. Mech. 55, 289–300. https://doi.org/10.1007/s11340-014-9856-4
Idar, D.J., Peterson, P.D., Scott, P.D., Funk, D.J., 1998. Low strain rate compression measurements of PBXN-9, PBX 9501, and mock 9501, in: AIP Conference Proceedings. AIP Publishing, pp. 587–590. https://doi.org/10.1063/1.55704
Jaramillo, E., Sewell, T.D., Strachan, A., 2007. Atomic-level view of inelastic deformation in a shock loaded molecular crystal. Phys. Rev. B - Condens. Matter Mater. Phys. 76, 064112. https://doi.org/10.1103/PhysRevB.76.064112
Johnson, G., Cook, W., 1985. Fracture characteristics of three metals subjected to various strains, strain rates, temperatures and pressures. Eng. Fract. Mech. 21, 31–48. https://doi.org/https://doi.org/10.1016/0013-7944(85)90052-9
Kendall, M.J., Siviour, C.R., 2015. Experimentally Simulating High Rate Composite Deformation in Tension and Compression: Polymer Bonded Explosive Simulant. J. Dyn. Behav. Mater. 1, 114–123. https://doi.org/10.1007/s40870-015-0018-2
Kim, K.S., Clifton, R.J., Kumar, P., 1977. A combined normal- and transverse-displacement interferometer with an application to impact of y-cut quartz. J. Appl. Phys. 48, 4132–4139. https://doi.org/10.1063/1.323448
Klopp, R.W., Clifton, R.J., 1990. Analysis of tilt in the high-strain-rate pressure-shear plate impact experiment. J. Appl. Phys. 67, 7171–7173. https://doi.org/10.1063/1.344549
Kroonblawd, M.P., Austin, R.A., 2021. Sensitivity of pore collapse heating to the melting temperature and shear viscosity of HMX. Mech. Mater. 152, 103644. https://doi.org/10.1016/j.mechmat.2020.103644
Kumar, P., Clifton, R.J., 1977. Optical alignment of impact faces for plate impact experiments. J. Appl. Phys. 48, 1366–1367. https://doi.org/10.1063/1.323734
Landauer, A.K., Li, X., Franck, C., Henann, D.L., 2019. Experimental characterization and hyperelastic constitutive modeling of open-cell elastomeric foams. J. Mech. Phys. Solids 133, 103701. https://doi.org/10.1016/j.jmps.2019.103701
Lindemann, F.A., 1910. The Calculation of Molecular Vibration Frequencies. Phys. Z. 609–612.
Liu, C., Rae, P.J., Cady, C.M., Lovato, M.L., 2011. Damage & fracture of high-explosive mock subject to cyclic loading, in: Conference Proceedings of the Society for Experimental Mechanics Series. Springer New York LLC, pp. 151–157. https://doi.org/10.1007/978-1-4614-0213-8_23
Malhotra, P., 2020. Dynamic Shearing Resistance of HTPB, Sucrose and their Polymer-Bonded Energetic Simulant. Brown University.
Malhotra, P., Jiao, T., Henann, D.L., Clifton, R.J., Guduru, P.R., 2021. Dynamic Shearing Resistance of Hydroxyl-Terminated Polybutadiene (HTPB). J. Appl. Phys.
Masterson, V.M., Cao, X., 2008. Evaluating particle hardness of pharmaceutical solids using AFM nanoindentation. Int. J. Pharm. 362, 163–171. https://doi.org/10.1016/j.ijpharm.2008.06.015
Menikoff, R., 2016. Complete Mie-Gruneisen Equation of State (update). Los Alamos, NM (United States). https://doi.org/10.2172/1241653
Menikoff, R., Sewell, T.D., 2002. Constituent properties of HMX needed for mesoscale simulations. Combust. Theory Model. 6, 103–125. https://doi.org/10.1088/1364-7830/6/1/306
Miller, G.R., Garroway, A.N., 2001. A Review of the Crystal Structures of Common Explosives Part I: RDX, HMX, TNT, PETN, and Tetryl.
Nadal, M.H., Le Poac, P., 2003. Continuous model for the shear modulus as a function of pressure and temperature up to the melting point: Analysis and ultrasonic validation. J. Appl. Phys. 93, 2472–2480. https://doi.org/10.1063/1.1539913
Patyk, E., Skumiel, J., Podsiadło, M., Katrusiak, A., 2012. High-Pressure (+)-Sucrose Polymorph. Angew. Chemie Int. Ed. 51, 2146–2150. https://doi.org/10.1002/anie.201107283
Poirier, J.P., Tarantola, A., 1998. A logarithmic equation of state. Phys. Earth Planet. Inter. 109, 1–8. https://doi.org/10.1016/S0031-9201(98)00112-5
Ramos, K.J., Bahr, D.F., 2007. Mechanical behavior assessment of sucrose using nanoindentation. J. Mater. Res. 22, 2037–2045. https://doi.org/10.1557/jmr.2007.0249

Rosakis, P., Rosakis, A.J., Ravichandran, G., Hodowany, J., 2000. Thermodynamic internal variable model for the partition of plastic work into heat and stored energy in metals. J. Mech. Phys. Solids 48, 581–607. https://doi.org/10.1016/S0022-5096(99)00048-4

Ross, M., 1969. Generalized Lindemann Melting Law, Physical Review.

Sandusky, H.W., Beard, B.C., Glancy, B.C., Elban, W.L., Armstrong, R.W., 1993. Comparison of deformation and shock reactivity for single crystals of RDX and ammonium perchlorate, in: Materials Research Society Symposium Proceedings. Publ by Materials Research Society, pp. 93–98. https://doi.org/10.1557/proc-296-93

Schwarz, R.B., Hooks, D.E., Dick, J.J., Archuleta, J.I., Martinez, A.R., 2005. Resonant ultrasound spectroscopy measurement of the elastic constants of cyclotrimethylene trinitramine. J. Appl. Phys. 98, 056106. https://doi.org/10.1063/1.2037865

Sewell, T.D., Menikoff, R., 2004. Complete Equation of State for β-HMX and Implications for Initiation, in: AIP Conference Proceedings. AIP Publishing, pp. 157–162. https://doi.org/10.1063/1.1780207

Sharma, J., Coffey, C.S., 1996. Nature of Ignition Sites and Hot Spots, Studied by Using an Atomic Force Microscope. AIP Conf. Proc. 370, 811. https://doi.org/10.1063/1.50834

Sharma, J., Coffey, C.S., Ramaswamy, A.L., Armstrong, R.W., 1996. Atomic force microscopy of hot spot reaction sites in impacted RDX and laser heated AP, in: Materials Research Society Symposium - Proceedings. Materials Research Society, pp. 257–264. https://doi.org/10.1557/proc-418-257

Shastry, A. V., Hartel, R.W., 1996. Crystallization and drying in thin sucrose films during panning. J. Food Sci. 61, 978–981. https://doi.org/10.1111/j.1365-2621.1996.tb10915.x

Sheffield, S.A., Duvall, G.E., 1983. Response of liquid carbon disulfide to shock compression: Equation of state at normal and high densities. J. Chem. Phys. 79, 1981–1990. https://doi.org/10.1063/1.445981

Sheffield, S.A., Gustavsen, R.L., Alcon, R.R., 1998. Porous HMX initiation studies—sugar as an inert simulant, in: AIP Conference Proceedings. AIP Publishing, pp. 575–578. https://doi.org/10.1063/1.55703

Simon, F., Glatzel, G., 1929. Bemerkungen zur Schmelzdruckkurve. Zeitschrift für Anorg. und Allg. Chemie 178, 309–316. https://doi.org/10.1002/zaac.19291780123

Siviour, C.., Laity, P.., Proud, W.., Field, J.., Porter, D., Church, P.., Gould, P., Huntingdon-Thresher, W., 2008. High strain rate properties of a polymer-bonded sugar: their dependence on applied and internal constraints. Proc. R. Soc. A Math. Phys. Eng. Sci. 464, 1229–1255. https://doi.org/10.1098/rspa.2007.0214

Steinberg, D.J., Cochran, S.G., Guinan, M.W., 1980. A constitutive model for metals applicable at high-strain rate. J. Appl. Phys. 51, 1498–1504. https://doi.org/10.1063/1.327799

Stevens, L.L., Eckhardt, C.J., 2005. The elastic constants and related properties of B -HMX determined by Brillouin scattering. J. Chem. Phys. 122. https://doi.org/10.1063/1.1883627

Trott, W.M., Baer, M.R., Castañeda, J.N., Chhabildas, L.C., Asay, J.R., 2007. Investigation of the mesoscopic scale response of low-density pressings of granular sugar under impact. J. Appl. Phys. 101. https://doi.org/10.1063/1.2427093

Wang, X., Wu, Y., Huang, F., Jiao, T., Clifton, R.J., 2016. Mesoscale thermal-mechanical analysis of impacted granular and polymer-bonded explosives. Mech. Mater. 99, 68–78. https://doi.org/10.1016/j.mechmat.2016.05.004

Williamson, D.M., Palmer, S.J.P., Proud, W.G., 2006. Fracture studies of PBX simulant materials, in: AIP Conference Proceedings. AIP, pp. 829–832. https://doi.org/10.1063/1.2263450

Zaug, J., 1998. Elastic Constants of β-HMX and Tantalum, Equations of State of Supercritical Fluids and Fluid Mixtures and Thermal Transport Determinations, in: Eleventh International Symposium on Detonation. Office of Naval Research Arlington, VA, p. 498.